A Precision Search for Exotic Scalar and Tensor Couplings in the Beta Decay of Polarized ^{37}K

by

Melissa Anholm

A Thesis submitted to the Faculty of Graduate Studies of
The University of Manitoba
in partial fulfillment of the requirements of the degree of

DOCTOR OF PHILOSOPHY

Department of Physics and Astronomy
University of Manitoba
Winnipeg

Abstract

There are four fundamental forces within the natural world: electromagnetism, gravity, the strong nuclear force, and the weak nuclear force. One of the primary windows to the inner workings of the weak nuclear force has long been found in observations of beta decay processes. Of particular interest is the form taken by the couplings involved in beta decay; prior experiments have shown that the process is dominated by a combination of vector and axial couplings, analogous to Maxwell's theory of electromagnetism — however the possibility of a non-dominant contribution from exotic scalar or tensor couplings remains. Such a discovery would shake the foundations upon which our understanding of the weak force is built.

A precision kinematic measurement is conducted to search for- or constrain exotic couplings within the nuclear weak force by measuring an observable known as the Fierz interference, b_{Fierz}, within the $^{37}\text{K} \rightarrow {}^{37}\text{Ar} + \beta^+ + \nu_e$ transition. The effect, if present, would manifest as a perturbation to the expected shape of the energy spectrum for betas emerging from a decay — or equivalently, as an apparent change to the energy dependence of the beta asymmetry (A_β, measured with respect to nuclear polarization), which is the approach employed here. As the observable is comprised of a linear combination of scalar and tensor couplings, any non-zero value of b_{Fierz} would be indicative of exotic physics.

The measurement is carried out within the TRINAT laboratory located at TRIUMF, which provides the radioactive ^{37}K necessary for the experiment. The TRINAT apparatus provides an isotope-specific means to cool, confine, and intermittently spin-polarize ^{37}K atoms within a magneto-optical trap. Upon decay, outgoing particles are emitted from a small central cloud into an open geometry featuring a variety of detectors. A thorough understanding of the nuclear polarization allows the superratio technique to be employed, greatly decreasing the size of many systematic errors. Geant4 simulations are used to model scattering effects and background events that could mimic the signal being searched for. The resulting measurement gives $b_{\mathrm{Fierz}} = +0.033 \pm 0.084(\mathrm{stat}) \pm 0.039(\mathrm{sys})$, consistent with the absence of exotic scalar and tensor couplings.

Contents

List of Figures

List of Tables

List of Abbreviations

AC-MOT	alternating current magneto-optical trap
BSM	beyond the standard model
CFD	constant fraction discriminator
CKM	Cabibbo–Kobayashi–Maskawa
CVC	conserved vector current
DC-MOT	direct current magneto-optical trap
DSSD	double-sided silicon strip detector
eMCP	electron microchannel plate
G4	Geant4
iMCP	ion microchannel plate
JTW	Jackson–Treiman–Wyld [1][2]
LE	leading edge
MC	monte carlo
MCP	microchannel plate
MOT	magneto-optical trap
NMR	nuclear magnetic resonance
OP	optical pumping
PDF	probability density function
PMT	photomultiplier tube
QED	quantum electrodynamics
RF	response function
rMCP	recoil microchannel plate
ROC	recoil-order corrections
SM	standard model of particle physics
SMC	simple monte carlo

SOE	shake-off electron
TDC	time-to-digital converter
TE	trailing edge
TOF	time of flight
TRINAT	TRIUMF Neutral Atom Trap
UHV	ultra-high vacuum

Chapter 1

Background

Within nature, there exist four fundamental forces governing the interactions of particles with one another: electromagnetism, the nuclear weak force, the nuclear strong force, and gravity. This work seeks to probe the nature of the weak nuclear force on its most fundamental level through observations of beta decay, a process which results directly from the action of the weak nuclear force. Through kinematic observations of the decay products, much can be learned about the form of the weak nuclear force's coupling, through which beta decay proceeds. Prior experiments have shown that this coupling is dominated by a combination of operators that behave as vectors and axial-vectors under Lorentz transformation, however the possibility of a non-dominant contribution from other types of operators, such as scalars and tensors, cannot be ruled out entirely. This is the domain of precision measurements.

1.1 Introduction

Within our present understanding of physics, there are four fundamental forces governing the interactions of particles with one another: electromagnetism, the nuclear weak force, the nuclear strong force, and gravity. These forces are considered to be distinct from one another by virtue of their differing behaviours, however attempting to unify them within a single theoretical framework has been a major focus of later 20th- and early 21st century physics to date. The effort has been met with only partial success, and the resulting theoretical framework is collectively known as the standard model of particle physics (SM).

The standard model provides a quantum mechanical description for the behaviour of three of the four fundamental forces: electromagnetism, the nuclear weak force, and the nuclear strong force. The SM notably does not describe gravitational processes — despite extensive efforts, the gravitational force has thus far defied all attempts to describe it in a fully quantum mechanical way, though this remains an active field of research.

Each force has its own specific mediating particle(s) which couple only to a particular type of (generalized) charge, and therefore interact only with particles that possess that charge. For example, the gravitational charge is *mass*, and (at least within a simplified particle physics model) gravity acts only on objects that possess mass. With only a single type of charge and no negative masses, the gravitational force can only ever be attractive. By constrast, the electromagnetic force couples to both positive and negative electric charges, and can produce both attractive and repulsive forces. Both the electromagnetic and gravitational forces are mediated by massless force-carrying particles (the photon and still-theoretical graviton, respectively), a property which implies that the amount of flux per unit solid angle is constant over all distance scales, and Gauss's Law holds true.

In the case of the nuclear weak force, which will be the primary concern within this thesis, the notion of generalized charge is no longer entirely straightforward to apply. We must rely instead on a list of allowed Feynman diagram vertices to describe the types of interaction that are possible (see Fig. 1.1). We note that the weak force involves three mediating particles — W^+, W^-, and Z^0 bosons — and these mediators can interact with both (anti-)quarks and (anti-)leptons. The W^+ and W^- particles also carry electric charge, which must be separately conserved in any interaction, but the Z^0 is electrically neutral. All three are massive, which implies that the strength of the weak force falls off more rapidly as distance increases, and Gauss's Law does not apply.

With a comparatively large number of possible vertex types, it can be challenging to develop an intuition about the behaviour of the weak force. Perhaps the most well known physical behaviour that arises from the nuclear weak force is beta decay. Indeed, beta decay offers one of the most readily accessible experimental windows to the workings of the nuclear weak force.

Although it is now generally well understood, beta decay still presents a unique opportunity for precision measurements to search for exotic physics beyond the Stan-

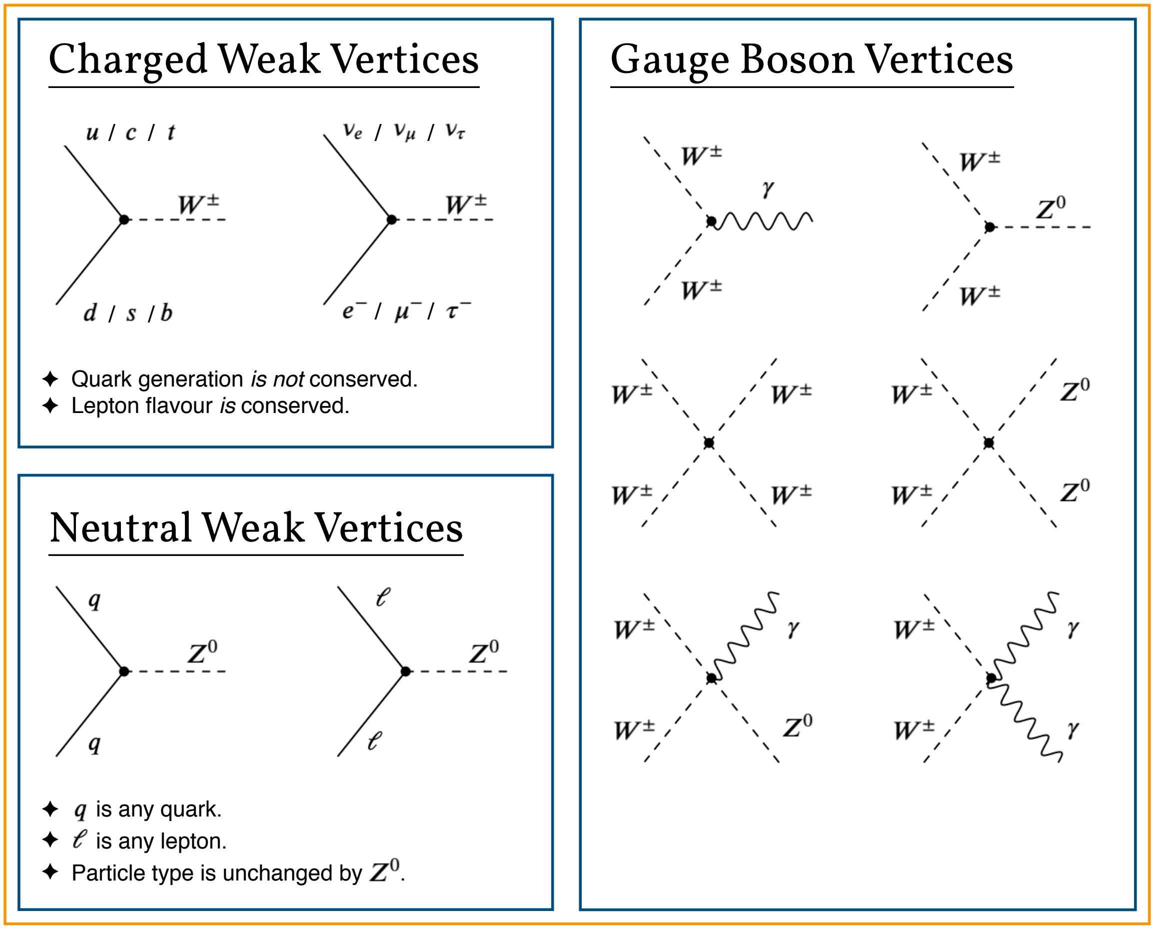

Figure 1.1: An exhaustive list of weak vertices. All possible Feynman diagram vertices involving W^+, W^-, or Z^0 bosons are shown, and the usual rules apply. These vertices show the types of interactions that can occur between the bosons mediating the weak force, and other types of particles. Only the fundamental vertices are shown, meaning that these diagrams are in some sense incomplete. At the energy scales available in everyday life, the W and Z bosons act only as an intermediary between two such vertices.

dard Model within the weak coupling. By observing the kinematics and angular correlations involved in the decay process, one gains access to a wealth of information about the laws underpinning the decay process, and the weak force as a whole.

1.2 A Historical Look at Beta Decay and the Weak Interaction

We consider the historical development of our scientific understanding of beta decay and the nuclear weak force. This is a historically rich topic, and a full discussion is beyond the scope of this document, however we shall attempt to touch on some highlights.

Radioactivity was first observed in 1896 by Henri Becquerel in uranium, and this landmark discovery set off a flurry of activity in the field [3]. Ernest Rutherford noted in 1899 that the particles emitted by a sample of uranium could be classified into two groups based on how readily they were absorbed in materials – alpha particles are easily absorbed, while beta particles are more penetrating [4]. A third and even more penetrating type of radioactive emission was observed in 1900 by Paul Villard, who made no attempt to give it a name – but within a few years, Rutherford's naming convention had been applied and this third type of particle became known as a gamma ray [5][6].

When, in 1900, Becquerel measured the charge-to-mass ratio of emitted beta (β^-) radiation and found that it was the same as that of the electron, he proposed that these must be the same particle [7], and in 1903 Rutherford and Soddy demonstrated that the processes of alpha and beta decay both transmute the original chemical element into another[8].

Despite these early successes, in 1911 Lise Meitner and Otto Hahn noticed that beta particles are emitted with a variety of different kinetic energies, and in 1914 James Chadwick demonstrated that energies of emitted beta particles formed a continuous distribution. The physics community was baffled for years by the fact that it seemed impossible to predict the energy of a beta particle emitted by a particular process; if the emitted beta simply took on the difference in energy between the initial and final states, then surely that energy should be a fixed, unchanging value for a paricular transition.

Finally, in 1930, a frustrated Wolfgang Pauli famously proposed that if an additional small, neutral, difficult to detect particle were emitted simultaneously with the beta and allowed to carry away a varying amount of energy, then this accounting trick could account for the continuous beta energy spectrum. He named this particle a “neutron” – though today we refer to that same particle as a(n) “(anti-)neutrino,” and use the name “neutron” for an entirely different particle[9].

Pauli’s 1930 insight paved the way for Enrico Fermi to propose a quantitative description of the nuclear weak force and the beta decay processes resulting from it. He modeled the weak force as a contact interaction with zero range — a very good approximation. After being rejected by *Nature* in 1933, Fermi’s seminal theory of beta decay was published in both Italian and German journals the following year [10] [11] [12]. Because of its powerful predictive ability together with its generalized quantum mechanical approach, Fermi’s model forms the basis upon which modern beta decay calculations have been built. With one of its major results, now commonly known as Fermi’s Golden Rule, still routinely used, the introduction of Fermi’s model arguably marks the beginning of our modern understanding of beta decay.

The mid 1930s was a busy time for our understanding of beta decay. In addition to the publication of Fermi’s model in 1934, this year also marks the first discovery of β^+ radiation, for which Irène and Frédéric Joliot-Curie later received a Nobel prize, and the proposal by Gian-Carlo Wick of the electron capture mechanism for beta decay. The electron capture theory was fleshed out further in 1935-1936 by Yukawa and Sakata, and first observed in 1937 by Luis Alvarez. Meanwhile, in 1936 George Gamow and Edward Teller improved upon Fermi’s model by including a mechanism to potentially change the nuclear spin[13], and to this day, beta decay transitions are still routinely classified as following Fermi or Gamow-Teller (or mixed) selection rules.

Over the next few years, developments within the field of nuclear physics were largely directed elsewhere, but beta decay returned to scientific prominence with T. D. Lee and C. N. Yang’s 1956 suggestion that, contrary to the community’s prior expectation, parity may not be conserved within beta decay processes[14]. The proposition was rapidly put to the test by C.S. Wu’s landmark 1957 measurement of ^{60}Co, confirming that beta decay violates parity conservation and simultaneously paving the way for the Nobel prize to be awarded to Lee and Yang that same year [15].

Subsequent experiments demonstrated that not only was parity non-conserved in a beta decay transition, it is (as near as we can collectively tell) *maximally* violated. Though early experiments suggested that the couplings were likely comprised of scalar and tensor interactions, Feynman and Gell-Mann first postulated the correct $(V - A)$ form of the interaction in 1958 by invoking an analogy with the photon, and this was eventually borne out by experimental evidence[16]. (See Sec. 1.3 for further discussion on the form of weak interaction couplings.)

In the following years, the theory behind the nuclear weak force was developed further, and eventually merged with the theory of electromagnetism as the electroweak force. The framework for quantum electrodynamics (QED) had already been largely developed between 1946 and 1950 by Shinichiro Tomonaga, Julian Schwinger, Richard Feynman, and others. The theory was fully covariant, meaning that it behaves properly under a Lorentz transformation. The work of Schwinger, and independently, Tomonaga, developed much of the methodology behind renormalization, which is now considered to be a mathematical necessity in any modern quantum field theory[17][18][19][20][21][22].

Following the success of QED, there was a push from the physics community to create a similar theory to model the nuclear weak force. Lee and Yang, and Feynman and Gell-Mann, produced two notable early examples of a weak force Lagrangian written, like the theory of electromagnetism, in terms of Lorentz-transforming currents[14][16]. Yang and Mills took a more mathematical approach, and their 1954 non-abelian gauge theory [23] lies at the foundation of electroweak unification.

In 1961, Sheldon Glashow extended some of Schwinger's work to model the nuclear weak force, adding an explicit mass term (i.e., to make the force mediating particles massive). The model included the W^+ and W^- bosons needed to explain beta decay, and for the first time, a neutral Z^0 boson. With the explicit mass term, the theory was not renormalizable, and since there had been no experimental hint of the Z^0, Glashow himself discounted the model, and it initially received little attention. In 1964, Abdus Salam and John Clive Ward proposed a similar theory, this time including the photon as well as $W^{\pm}$ and Z^0 bosons – however they, too, relied on explicit symmetry breaking to provide a mass for the $W^{\pm}$ and Z^0 bosons[24][25][26].

With the development of the Higgs mechanism in 1964, which provided an indirect mechanism for gauge bosons to gain a non-zero mass spontaneously without the need to explicitly add a mass term[27][28][29][30][31], it was perhaps only a matter of time before Salam and, separately, Steven Weinberg applied that mechanism to the weak force in 1967, producing a theory of electroweak interaction that was potentially renormalizable[32][33]. It was not until 1971 that Gerardus 't Hooft and Martinus Veltman proved that this class of theories actually *is* renormalizable, thereby making the Weinberg-Salam model of the electroweak force a much more viable theory[34].

The Weinberg-Salam model of electroweak interactions was borne out by the experimental observation of the weak neutral current (i.e., the interaction mediated by the Z^0 boson) in 1973 at CERN's Gargamelle bubble chamber experiment[35]. The $W^{\pm}$ and Z^0 bosons themselves were first unambiguously observed at CERN's Super Proton Synchrotron in 1983[36][37][38][39] – with the $W^{\pm}$ and Z^0 being quite massive in comparison to other fundamental particles, earlier experimental designs had not been powerful enough to reach the necessary energy scale.

Following the development of electroweak unification, theorists turned their attention to the nuclear strong force, which had been challenging to model in a mathematically rigorous way due to its property of growing *stronger*, rather than weaker, at long distances. The breakthrough came in 1973, when David Gross and Frank Wilczek, and separately, David Politzer developed a model of asymptotic freedom applied to the nuclear strong force[40][41][42].

The completed theories of electroweak and strong interactions, together, formed the core of what has come to be known as the standard model of particle physics (SM). It is unclear exactly when this terminology developed, or who originated it, but it had certianly come into use by the mid-1970s, and the usage still persists[43][44]. Notably, the only one of the fundamental forces not included under the umbrella of the standard model is the force of gravity, which is not compatible, as it is currently understood, with the quantum mechanical underpinnings of the standard model. In the decades since, this incompatibility has been a major focus of inquiry for theoretical physicists, but the problem remains unresolved.

1.3 Beta Decay within the Standard Model and Beyond

In the most general sense, the process of beta decay is one in which a nucleon (proton or neutron) is transformed into a different nucleon (i.e., a neutron or proton, respectively) and a beta particle (a positron or electron, respectively) and neutrino are emitted.

At the nucleon level, there are three basic classes of beta decay processes:

$$n \rightarrow p + e^- + \bar{\nu}_e \qquad \beta^- \text{ Decay} \tag{1.1}$$

$$p \rightarrow n + e^+ + \nu_e \qquad \beta^+ \text{ Decay} \tag{1.2}$$

$$p + e^- \rightarrow n + \nu_e, \qquad \text{Electron Capture} \tag{1.3}$$

where p represents a proton and n a neutron, e^-/e^+ represents an electron/positron (often referred to as a β^-/β^+), and $\nu_e/\bar{\nu}_e$ represents an electron neutrino/electron anti-neutrino. In practice, these are often all simply referred to as "neutrinos".

Of course, the processes of β^+ decay and electron capture are energetically disallowed for a proton not bound within a nucleus, but a free neutron will eventually undergo β^- decay. Within the nucleus, rules of which processes are and are not energetically allowed are dependent on the specific nucleus in question. Figure 1.2 shows the Feynman diagrams associated with each of these processes.

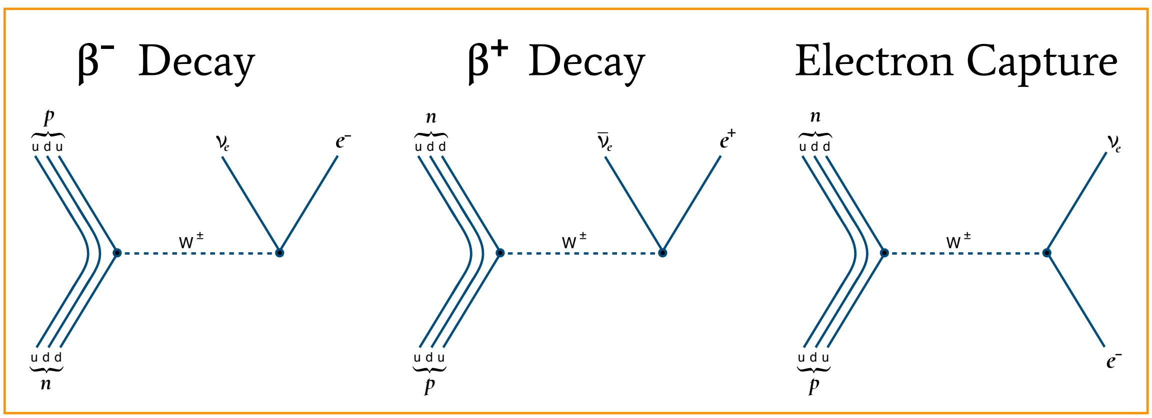

Figure 1.2: Beta decay Feynman diagrams are drawn here to describe the three most common types of beta decay. The interactions are mediated by massive $W^{\pm}$ bosons, resulting in an extremely limited range for the weak force.

Energetic considerations aside, it is worthwhile to consider whether there might be any rules relating to the *spin* of the nucleons before and after a decay, or the spins and angular correlations of the leptons that emerge. Does the nucleon's spin flip during the decay process, or remain unchanged? Are the decay products emitted preferentially in any particular direction? Which direction are the beta and neutrino spins pointed in after they are emitted? Angular momentum must, of course, be conserved – but the question is *how* it is to be conserved. This question is not only at the heart of many modern precision measurements in beta decay physics, it has also been a driving force behind the development of much of our understanding of the nuclear weak force.

We must develop the tools with which these questions can be discussed. We will begin by using Fermi's classic description of a beta decay as a transition that occurs with zero range:

$$\mathcal{M}_{fi} \;=\; G_F \int \bar{\psi}_f \, \hat{\mathcal{O}} \, \psi_i \, \mathrm{d}V, \tag{1.4}$$

where $\mathcal{M}_{fi}$ is the transition matrix element between the final (ψ_f) and initial (ψ_i) states, and G_F gives a measure of the strength of the coupling between states. The integral is evaluated over phase space volume, and the operator $\hat{\mathcal{O}}$, which has yet to be determined, allows for a mathematical description of how the initial and final states must be related in order for a transition to occur.

Of course, this description represents a model of nuclear transitions which is highly simplified; by neglecting the W bosons that mediate the process and that we now know to be present, the result is a description of an interaction with zero range – i.e., the leptons must be emitted from the exact place where the nucleon was transmuted. Because the mediating W bosons are so heavy ($m_W = 80.379(12)\,\mathrm{GeV}/c^2$ [45]), the range of the interaction is extremely limited, so the above turns out to be a very good description.

This immediately gives rise to a rate law commonly known as Fermi's Golden Rule,

$$\Gamma \;=\; \frac{1}{\tau} \;=\; \frac{2\pi}{\hbar} \left|\mathcal{M}_{fi}\right|^2 \, \rho(E_f), \tag{1.5}$$

which describes the relationship between the total transition rate Γ (or equivalently the lifetime τ), the transition matrix element $\mathcal{M}_{fi}$, and the available density of states at the final energy, $\rho(E_f)$. We can also use this to write down the differential decay rate,

$$\frac{\mathrm{d}^5\Gamma}{\mathrm{d}E_\beta \mathrm{d}\hat{\mathbf{\Omega}}_\beta \mathrm{d}\hat{\mathbf{\Omega}}_\nu} \;=\; \frac{1}{(2\pi)^5} \, p_\beta E_\beta (E_0 - E_\beta)^2 F_\pm(E_\beta, Z') \left|\mathcal{M}_{fi}\right|^2, \tag{1.6}$$

where E_β and p_β are the outgoing β's (total) energy and momentum, E_0 is the maximum possible β energy associated with the transition, and $F_\pm(Z', E_\beta)$ is called a

Fermi function (with Z' the proton number of the daughter), and is used to account for the electric force between the nucleus and the (charged) outgoing electron (top) or positron (bottom) [11][12][46].

With this description, the problem of characterizing the transition is reduced to determining the form of $\hat{\mathcal{O}}$. Table 1.1 provides a comprehensive list of all operators for which Lorentz invariance holds. The complete transition operator $\hat{\mathcal{O}}$ must be comprised of a linear combination of these terms.

Lorentz Invariant Operators

Name	Form	Parity
Scalar	1	$+$
Pseudoscalar	γ_5	$-$
Vector	γ_μ	$-$
Axial-vector	$\gamma_\mu\gamma_5$	$+$
Tensor	$\gamma_\mu\gamma_\nu - \gamma_\nu\gamma_\mu$	N/A

Table 1.1: A complete list of operators that obey Lorentz invariance, defined in terms of Dirac γ-matrices. It can be shown that the operators listed here span the entire space, meaning that any other Lorentz invariant operator can be expressed as a sum of the above.

An equivalent expression for Eq. 1.4 can be written in terms of the interaction Hamiltonian $\mathcal{H}_{\text{int}}$, as:

$$\mathcal{M}_{fi} = \int \mathcal{H}_{\text{int}}\,\mathrm{d}V. \tag{1.7}$$

To obtain a full solution to the above, we will make use of the Lee-Yang interaction Hamiltonian, which provides a generalized combination of the Lorentz invariant operators and fits neatly into Eq. 1.7 [14]:

$$\begin{aligned}
\mathcal{H}_{\text{int}}\,/\,G_F \;=\;& (\bar{\psi}_p\psi_n)(C_S\,\bar{\psi}_e\psi_\nu + C'_S\,\bar{\psi}_e\gamma_5\psi_\nu) \\
&+ (\bar{\psi}_p\gamma_\mu\psi_n)(C_V\,\bar{\psi}_e\gamma_\mu\psi_\nu + C'_V\,\bar{\psi}_e\gamma_\mu\gamma_5\psi_\nu) \\
&+ \frac{1}{2}(\bar{\psi}_p\sigma_{\lambda\mu}\psi_n)(C_T\,\bar{\psi}_e\sigma_{\lambda\mu}\psi_\nu + C'_T\,\bar{\psi}_e\sigma_{\lambda\mu}\gamma_5\psi_\nu) \\
&- (\bar{\psi}_p\gamma_\mu\gamma_5\psi_n)(C_A\,\bar{\psi}_e\gamma_\mu\gamma_5\psi_\nu + C'_A\,\bar{\psi}_e\gamma_\mu\psi_\nu) \\
&+ (\bar{\psi}_p\gamma_5\psi_n)(C_P\,\bar{\psi}_e\gamma_5\psi_\nu + C'_P\,\bar{\psi}_e\psi_\nu) + \text{H.C.},
\end{aligned} \tag{1.8}$$

Here, C_X and C'_X (with $X = \{V, A, S, T, P\}$) are complex coupling constants for vector, axial, scalar, tensor, and pseudoscalar interactions, and ψ_Y (with $Y = \{p, n, e, \nu\}$) are the wavefunctions for the interaction's proton, neutron, electron, and neutrino. Operators γ_5 and γ_μ are Dirac gamma matrices, and $\sigma_{\lambda\mu} = -\frac{i}{2}(\gamma_\lambda\gamma_\mu - \gamma_\mu\gamma_\lambda)$. As usual, "H.C." represents the Hermitian conjugate of the previous terms within the Hamiltonian.

It can be seen from the form of the Hamiltonian that the V, A, S, T, P couplings within are described as such because they *behave* as vectors, axial-vectors, scalars, tensors, and pseudoscalars (respectively) under a Lorentz transform, where the Lagrangian itself must be a scalar both before and after a Lorentz transform [14] [47] [48].

The fact that there are two coupling constants (primed and unprimed) for each type of coupling relates to the *handedness* of the interaction. Both left-handed and right-handed couplings, or a combination thereof, are *a priori* possible, and the form of Eq. 1.8 does not give preference to either.

While it is possible to define an interaction's handedness in a rigorous and mathematical way, the reader may gain more clarity by simply remembering the rule of thumb that a left-handed weak force couples only to left-handed regular matter leptons and right-handed anti-leptons — where the handedness of a lepton or other particle is defined by the direction of its spin relative to its direction of motion. That description is exact in the limit where such a particle travels at the speed of light (otherwise a clever Lorentz transform can change the result), but the underlying mathematics is well defined for slower particles as well. For neutrinos, which are so light they were long believed to be massless, the description is nearly perfect. For electrons and positrons emitted in beta decay, which are massive but often emitted at relativistic speeds, the description is modified by inserting a factor of v/c to quantify the handedness exactly.

Over the years, we have collectively learned much about which simplifications to Eq. 1.8 can be justified. Typically, reference to the pseudoscalar couplings is one of the first things to be dropped, because it is suppressed at typical beta decay energies, and as such its presence would be difficult to demonstrate and have very little effect on experimental results. It is also now widely understood that the nuclear weak force involves primarily (or entirely) vector and axial vector couplings, and is primarily (or entirely) a left-handed interaction in which parity is maximally (or nearly maximally) violated.

Although the physics community has largely come to a consensus on the *dominant* behaviour of the nuclear weak force, there still exists a range of possible *sub-dominant* behaviours that cannot be ruled out by theoretical considerations alone, and therefore must be tested experimentally. With the weak force already so well described, searching for indications of unexpected behaviours is the domain of precision measurements. This class of non-dominant behaviours is sometimes described as exotic physics, or with the imprecise label of physics beyond the standard model (BSM), or even the wildly inaccurate misnomer, "new physics" [49][50][51][52][53][54][55].

Many types of exotic physics have, in fact, already been described by Lee and Yang's 1956 interaction Hamiltonian, which was originally motivated by the question of parity conservation within beta decay[14]. Despite the original motivations, the authors were very thorough in their description of possible interaction types. By starting with Fermi's contact interaction model of beta decay, incorporating Gamow and Teller's selection rules, and enforcing Lorentz invariance, they arrived at a nucleon-level Hamiltonian (quarks had not been discovered yet) which accounted for *all* possible coupling behaviours [13].

1.4 Our Decay

Here, we will focus on the decay,

$$^{37}\mathrm{K} \quad \rightarrow \quad ^{37}\mathrm{Ar} + \beta^{+} + \nu_{e}, \tag{1.9}$$

which is extremely well suited to the type of experiment to be the discussed in this thesis. The parent, ^{37}K, is an isotope of potassium—an alkali. Though this fact may initially seem unremarkable, it is their hydrogen-like single valence electron which allows alkalis to be readily trapped within a magneto-optical trap, a critical component of our experimental design (see Chapter 2).

A potential concern in any experiment concerned with the angular correlations resulting from one particular decay branch is the background from competing decay branches. As can be seen in Fig. 1.3, the decay of ^{37}K is dominated by a single branch which contributes nearly 98% of ^{37}K decay events, and the remaining events nearly all arise from a single branch contributing around 2% of the decay events. The other branches combined account for only around 0.04% of decays. Taken all together, this means that the background events which must be accounted for are both infrequent and well understood.

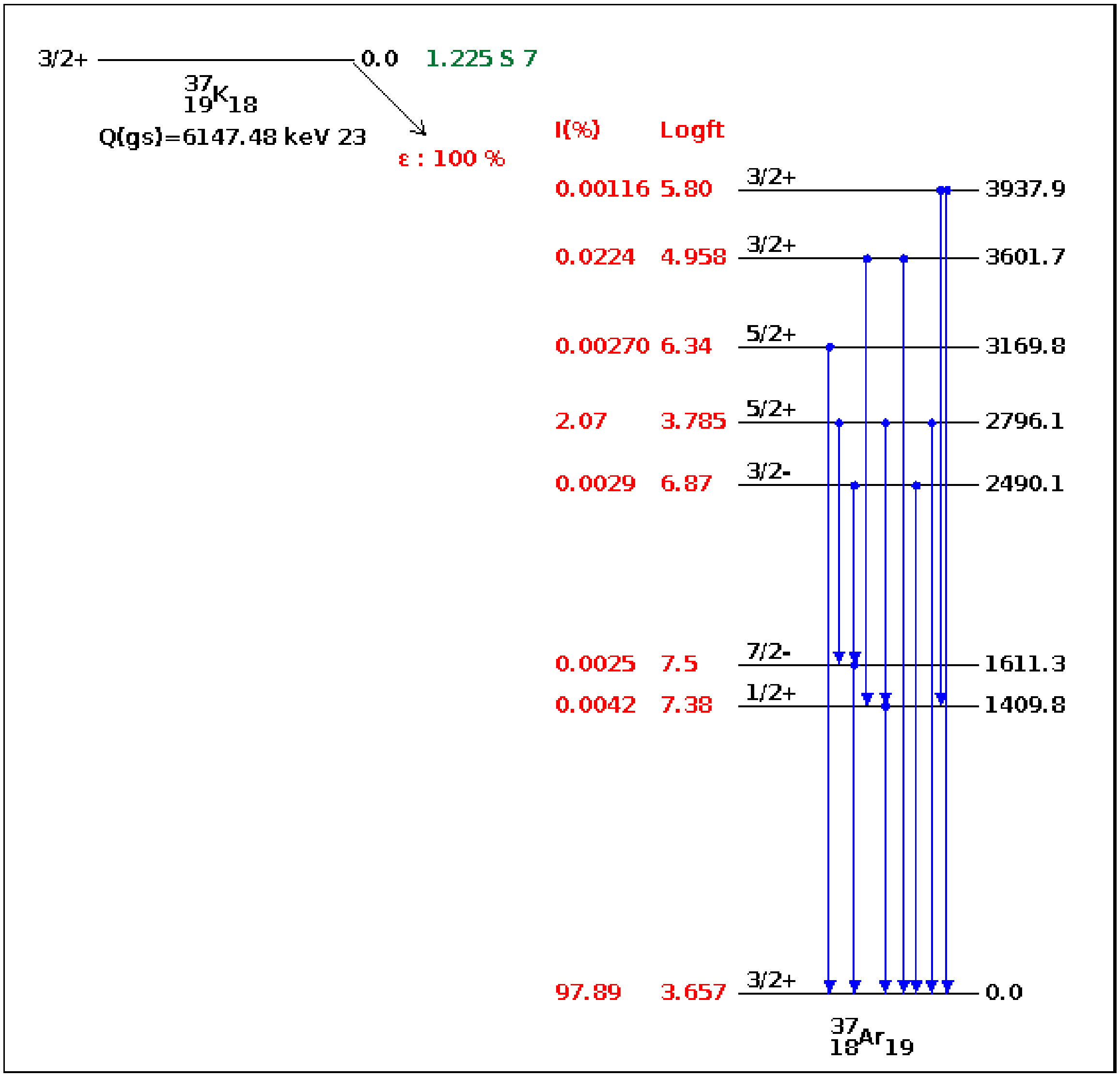

Figure 1.3: A Decay Scheme for ^{37}K, generated with the NuDat3 database toolset. The $I(\%)$ column indicates the fraction of total decays which proceed to each level, and 'Logft' gives a measure of the absolute decay rate[46]. The column immediately to the right of Logft indicates nuclear spin and parity, and the far right column is the energy relative to the ground state, in keV[56][57][58].

As in any decay, the angular correlations between the emerging daughter particles provide a rich source of information about the type of interaction that produced the decay. This particular decay involves a set of isobaric mirror nuclei, meaning that the nuclear wavefunctions of the parent and daughter are identical up to their isospin quantum number and corresponding electrical charge. Because the two wavefunctions are so similar, effects to the decay from nuclear structure corrections are well understood and can be kept to a minimum, making it possible to place especially strong constraints on the size of the theoretical uncertainties associated with the decay.

1.5 The Physical Signature of the Fierz Interference

In this section, we consider how scalar and tensor interactions within the beta decay process might manifest as a physical observable. As this section is, in part, intended to aid the reader in gaining a physical intuition for certain aspects of decay behaviour, only the leading order terms are described. However, the full mathematical formalism including many higher-order terms is worked out in detail within Appendix C. The probability density function (PDF) below provides a description of beta decay in terms of the outgoing beta's energy and direction relative to the nuclear spin, in terms of (almost) all mathematically consistent types of couplings. (Pseudoscalar couplings are neglected in this treatment, because they are relativistically suppressed at the energy scales characteristic of typical beta decays.) This PDF is a simplification of the one presented in the classic Jackson–Treiman–Wyld (JTW) paper, and is accurate to leading order [1][2][59]. For the dominant branch of ^{37}K decay, we have:

$$\mathrm{d}^2\Gamma(E_\beta,\theta) \;=\; W(E_\beta)\left[1 + b_{\mathrm{Fierz}}\frac{m_e c^2}{E_\beta} + A_\beta\,\frac{p_\beta c}{E_\beta}\,|\vec{\boldsymbol{P}}|\cos\theta\right]\mathrm{d}E_\beta\,\mathrm{d}\theta, \tag{1.10}$$

where $\vec{\boldsymbol{P}}$ is the overall nuclear spin polarization, E_β and p_β are the energy and momentum of the outgoing beta particle, and θ is the angle between $\vec{\boldsymbol{P}}$ and the beta emission direction. As usual, m_e is the mass of the electron and c is the speed of light. The expression's overall energy dependence has been absorbed into the term $W(E_\beta)$, so that

$$W(E_\beta) \;:=\; \frac{2}{(2\pi)^3}\,F_-(Z',E_\beta)\,\xi\,p_\beta E_\beta(E_0-E_\beta)^2, \tag{1.11}$$

where E_0 is the maximum possible beta energy associated with the transition. The function $F_-(Z', E_\beta)$ is a Fermi function for outgoing positrons, with Z' the proton number of the daughter nucleus. The Fermi function accounts for the force from the electric charge of the daughter nucleus and its orbital electrons acting on the outgoing electron/positron. It is computed with the Dirac equation using various levels of approximation to describe the nuclear charge distribution and screening of that charge distribution by electrons near the nucleus.

We now turn our attention to the parameters A_β (the beta asymmetry), b_{Fierz} (the Fierz interference), and ξ that are used in Eqs. (1.10)-(1.11). These parameters are unique to the transition under consideration, but are nevertheless closely related to certain universally applicable coupling strengths. They can be written in terms of the universally applicable complex coupling constants C_X and C'_X of Eq. (1.8) as follows:

$$\begin{aligned}
\xi &= |M_F|^2 \left(|C_S|^2 + |C_V|^2 + |C'_S|^2 + |C'_V|^2\right) \\
&+ |M_{GT}|^2 \left(|C_T|^2 + |C_A|^2 + |C'_T|^2 + |C'_A|^2\right) \qquad (1.12) \\
b_{\text{Fierz}}\, \xi &= -2\gamma\, \text{Re}\big[|M_F|^2 \left(C_S C_V^* + C'_S C'^*_V\right) + |M_{GT}|^2 \left(C_T C_A^* + C'_T C'^*_A\right)\big] \qquad (1.13)
\end{aligned}$$

$$\begin{aligned}
A_\beta\, \xi &= \frac{4}{5}\, |M_{GT}|^2 \left[\text{Re}[C_A C'^*_A - C_T C'^*_T] + \frac{\alpha Z m_e c^2}{p_\beta c}\, \text{Im}[C_T C'^*_A + C'_T C^*_A]\right] \\
&+ 2\left(\frac{3}{5}\right)^{1/2} M_F\, M_{GT} \Bigg[\text{Re}[C_S C'^*_T + C'_S C^*_T - C_V C'^*_A - C'_V C^*_A] \\
&- \frac{\alpha Z' m_e c^2}{p_\beta c}\, \text{Im}[C_S C'^*_A + C'_S C^*_A - C_V C'^*_T - C'_V C^*_T]\Bigg]. \qquad (1.14)
\end{aligned}$$

In the above expressions, M_F and M_{GT} are the Fermi (vector coupling) and Gamow-Teller (axial coupling) matrix elements unique to a particular transition, and $\gamma := (1 - \alpha^2 Z'^2)^{1/2} \approx 1$, using fine structure constant α.

The expressions above have many free parameters, and some simplifications and assumptions must be made before any experimental measurement can be interpreted in a physically meaningful way. We note that each type of interaction X (for $X = \{V, A, S, T\}$) is described by *two* complex coupling constants, C_X and C'_X; this extra degree of freedom is necessary in order to describe couplings to both left-handed and right-handed helicity leptons. In practice, we already know that the weak force couples (almost) entirely to left-handed electrons and right-handed positrons. Separately, we know that the interaction proceeds (almost) entirely by vector and axial couplings. Taken together, this suggests that neutrinos and anti-neutrinos, as leptons, must (predominantly) follow the same helicity selection rules that apply to electrons and positrons. This is because, *e.g.*, a decay mediated by either scalar or tensor couplings would produce two outgoing leptons/anti-leptons of the *same* helicity.

It is this subtlety which gives rise to the energy dependence $(m_e c^2/E_\beta)$ by which b_{Fierz} is multiplied in Eq. (1.10). That is, if we have restricted ourselves to interactions involving right-handed anti-neutrinos travelling at the speed of light, then the scalar or tensor components of this interaction, if present, must also couple to right-handed helicity electrons. The lower the energy of the outgoing electron, the greater the fraction of available phase space in which the electron appears to be right-handed from the reference frame of the mediating W-boson. In other words, this term describes a mechanism by which scalar and tensor couplings can effectively compete with the expected vector and axial couplings [48][60].

As a practical matter, the $(m_e c^2/E_\beta)$ dependence of the Fierz term suggests that b_{Fierz} is best measured by a relatively low-energy experiment (such as the one described here) in order to maximize sensitivity; a high-energy experiment would have trouble constraining it.

We will henceforth take $C_X = C'_X$, which is equivalent to a requirement that all couplings are left-handed. We define a set of purely left-handed couplings:

$$g_V = \frac{1}{\sqrt{2}}\left(C_V + C'_V\right) \tag{1.15}$$

$$g_A = \frac{-1}{\sqrt{2}}\left(C_A + C'_A\right) \tag{1.16}$$

$$g_S = \frac{1}{\sqrt{2}}\left(C_S + C'_S\right) \tag{1.17}$$

$$g_T = \frac{-1}{\sqrt{2}}\left(C_T + C'_T\right). \tag{1.18}$$

Furthermore, we will also require going forward that all C_X must be *real*; this is equivalent to requiring that the interactions obey time-reversal invariance. We also introduce ρ, the ratio of Gamow-Teller and Fermi couplings:

$$\rho \ := \ \frac{C_A M_{GT}}{C_V M_F} \ = \ \frac{-g_A M_{GT}}{g_V M_F}. \tag{1.19}$$

The value of ρ is unique to a particular transition, and must be extracted experimentally (see Sec. 1.7).

Using the above notation and the simplifying assumptions that give rise it, and dropping terms of order (small)^2 or higher, it is possible to re-write Eqs. (1.12)-(1.14) as:

$$\xi \ = \ 2\, C_V^2 \, |M_F|^2 \left(1+\rho^2\right) \tag{1.20}$$

$$b_{\text{Fierz}} \ = \ \frac{-2\gamma}{1+\rho^2}\left(\frac{g_S}{g_V}+\rho^2\frac{g_T}{g_A}\right). \tag{1.21}$$

$$A_\beta \ = \ \frac{\frac{2}{5}\rho^2 - 2\rho\sqrt{\frac{3}{5}}}{1+\rho^2}, \tag{1.22}$$

where b_{Fierz} reduces to 0 in the standard model limit where $g_S = g_T = 0$. Notably, b_{Fierz} is the only term within our beta decay PDF which includes (small) exotic couplings at the *linear* order; g_S and g_T arise only at quadratic order within the other terms, and thus have been dropped from Eqs. (1.20) and (1.22) above.

1.6 The Superratio

In considering Eqs. (1.10)-(1.11), we see that the b_{Fierz} term includes an explicit energy dependence. From this, it seems natural to conclude that the shape of the beta energy spectrum can be used to measure the value of b_{Fierz}. This assertion is correct as far as it goes — but a direct measurement of the complete energy spectrum is arguably not the best way to approach the matter. In fact, it is possible to extract a much clearer signal to measure both A_β and b_{Fierz} by making some clever choices in how our data should be processed. To see this, it is helpful to consider the A_β term within Eq. (1.10), which carries an explicit angular dependence as well as its own explicit energy dependence.

Though a judicious choice of detector placements, it is possible to measure the beta energy spectrum at its angular extrema, with $\cos\theta \approx \pm 1$ (recall that θ is defined to be the angle between direction of nuclear polarization and beta emission). With differing contributions to each angle-selected beta spectrum from the A_β term (and no other angular dependence), it is clear that any nonzero b_{Fierz} term must provide a different *fractional* contribution to the full spectrum as a function of angle.

One way to quantify this fractional difference might be to take a simple ratio of the two spectra, evaluated at each energy bin — however the effect of a non-zero b_{Fierz} term would be quite small in comparison with the overarching angular dependence of A_β. Indeed, with the observed beta spectra explicitly selected according to emission angle, it makes little sense to attempt to extract a measurement of b_{Fierz} without a simultaneous measurement of A_β. With this caveat kept in mind, we will now work towards finding an expression for A_β in terms of experimental observables, with the understanding that an expression for b_{Fierz} will follow naturally.

We will approach the problem by first separating beta energy spectral data into categories relating to the angular dependence of an individual event with respect to the direction of nuclear spin. If, as in our case, these sets of data can be further subdivided into categories that can be expected to measure similar physical behaviours, but which may have differing systematic effects, it is possible to force many of these these systematic effects to cancel out at leading order, as we will soon see.

For example, within the TRINAT experimental setup, the polarization is flipped periodically between two states (+/-), within a (mostly) symmetric apparatus. Two similar beta detectors (T/B) are positioned opposite one another along the vertical axis of polarization at the top and bottom of the experimental chamber (see Chapter 3). Then, with two detectors and two polarization states, we can describe four different experimental count rates based on Eq. (1.10). Neglecting scattering effects, we have:

$$
\begin{aligned}
r_{\mathrm{T}+}(E_\beta) &= W(E_\beta)\,\varepsilon_{\mathrm{T}}(E_\beta)\,\Omega_{\mathrm{T}}\,N_+\left[1 + b_{\mathrm{Fierz}}\frac{m_e c^2}{E_\beta} + A_\beta\,\frac{v}{c}|\vec{\boldsymbol{P}}_+|\langle\cos\theta\rangle_{\mathrm{T}+}\right] && (1.23)\\
r_{\mathrm{B}+}(E_\beta) &= W(E_\beta)\,\varepsilon_{\mathrm{B}}(E_\beta)\,\Omega_{\mathrm{B}}\,N_+\left[1 + b_{\mathrm{Fierz}}\frac{m_e c^2}{E_\beta} + A_\beta\,\frac{v}{c}|\vec{\boldsymbol{P}}_+|\langle\cos\theta\rangle_{\mathrm{B}+}\right] && (1.24)\\
r_{\mathrm{T}-}(E_\beta) &= W(E_\beta)\,\varepsilon_{\mathrm{T}}(E_\beta)\,\Omega_{\mathrm{T}}\,N_-\left[1 + b_{\mathrm{Fierz}}\frac{m_e c^2}{E_\beta} + A_\beta\,\frac{v}{c}|\vec{\boldsymbol{P}}_-|\langle\cos\theta\rangle_{\mathrm{T}-}\right] && (1.25)\\
r_{\mathrm{B}-}(E_\beta) &= W(E_\beta)\,\varepsilon_{\mathrm{B}}(E_\beta)\,\Omega_{\mathrm{B}}\,N_-\left[1 + b_{\mathrm{Fierz}}\frac{m_e c^2}{E_\beta} + A_\beta\,\frac{v}{c}|\vec{\boldsymbol{P}}_-|\langle\cos\theta\rangle_{\mathrm{B}-}\right], && (1.26)
\end{aligned}
$$

where the $\varepsilon_{\mathrm{T/B}}(E_\beta)$ are the (top/bottom) detector efficiencies, $\Omega_{\mathrm{T/B}}$ are the fractional solid angles from the trap position to the (top/bottom) detector from the trap position, $N_{+/-}$ are the number of atoms trapped in each (+/-) polarization state, and $|\vec{\boldsymbol{P}}_{+/-}|$ are the magnitudes of the polarization along the detector axis for each polarization state. $\langle\cos\theta\rangle_{\mathrm{T/B},+/-}$ is the average of $\cos\theta$ for *observed* outgoing betas, for each detector and polarization state combination. This latter term is approximately ±1 as a result of our detector geometry, but contains important sign information.

For a pointlike trap in the center of the chamber, 103.484 mm from either (DSSSD) detector, each of which is taken to be circular with a radius of 15.5 mm, we find that $\langle|\cos\theta|\rangle_{\mathrm{T/B},+/-} \approx 0.994484$, and is the same for all four cases. Note that a horizontally displaced trap will decrease the magnitude of $\langle|\cos\theta|\rangle$, but as it is an expectation value of an absolute value, all four will remain equal to one another. In the case of a vertically displaced trap, these four values will no longer all be equal, however it will still be the case that $\langle|\cos\theta|\rangle_{\mathrm{T}+} = \langle|\cos\theta|\rangle_{\mathrm{T}-}$, and $\langle|\cos\theta|\rangle_{\mathrm{B}+} = \langle|\cos\theta|\rangle_{\mathrm{B}-}$.

Recalling the form of the overall energy dependence $W(E_\beta)$ from Eq. (1.11), we note that the presence of the Fermi function $F_-(Z', E_\beta)$ at any reasonable level of approximation makes $W(E_\beta)$ integrable only by numerical methods. As a result, there is little that could be changed to make the expression more difficult to work with, so we can safely take $W(E_\beta)$ to be an arbitrary function. Therefore, for the remainder of this section, we will take $W(E_\beta)$ to implicitly include the small corrections to overall energy dependence that arise from e.g. recoil-order corrections, as described by Holstein [61].

These four beta spectra can be used to construct the so-called superratio and superratio asymmetry, both of which have some very useful properties. The latter of these is the measure that will eventually be used to extract the values of A_β and b_{Fierz}.

We define the superratio, s, as:

$$s \;=\; s(E_\beta) \;:=\; \frac{r_{\mathrm{T}-}\, r_{\mathrm{B}+}}{r_{\mathrm{T}+}\, r_{\mathrm{B}-}}, \tag{1.27}$$

and the superratio asymmetry, A_{super}, as:

$$A_{\text{super}} = A_{\text{super}}(E_\beta) := \frac{1-\sqrt{s}}{1+\sqrt{s}} \tag{1.28}$$

$$= \frac{\sqrt{r_{\text{T}+}\, r_{\text{B}-}} - \sqrt{r_{\text{T}-}\, r_{\text{B}+}}}{\sqrt{r_{\text{T}+}\, r_{\text{B}-}} + \sqrt{r_{\text{T}-}\, r_{\text{B}+}}}. \tag{1.29}$$

This is explicitly an experimental quantity that is measured directly by the above combination of count rates, however it is obvious that it reduces, under appropriate limits, to be equivalent to a naive asymmetry. In particular, if we require that the physical conditions and relative detector positions and sensitivities are identical when the polarization is flipped, then we have $r_{\text{T}+}(E_\beta) = r_{\text{B}-}(E_\beta)$, $r_{\text{T}-}(E_\beta) = r_{\text{B}+}(E_\beta)$, and $|\vec{\boldsymbol{P}}_+| = |\vec{\boldsymbol{P}}_-|$. With these simplifying assumptions, the superratio asymmetry quickly reduces into a more intuitive quantity that we might use for a measurement with only a single polarization state, e.g.,

$$A_{\text{super}} \rightarrow \frac{r_{\text{T}+} - r_{\text{B}+}}{r_{\text{T}+} + r_{\text{B}+}} \xrightarrow[b_{\text{Fierz}}=0]{} A_\beta \frac{v}{c} |\vec{\boldsymbol{P}}_+| \,\langle |\cos\theta| \rangle. \tag{1.30}$$

The superratio, and superratio asymmetry, has been used for precision beta decay measurements in the past to measure the neutron's beta asymmetry[62], and our own collaboration has also used it to measure the beta asymmetry in ^{37}K [63]. More recently, it has been used to measure the neutron's Fierz interference term [64][65] as well, with notably more impressive results than using the earlier 'supersum' data combination method [66].

While Eq. 1.30 is conceptually encouraging, the assumptions that gave rise to it are too simplifying. Fortunately, as we'll soon see, the key to the effectiveness of the superratio technique is that many systematic effects can be made to cancel at the leading order, at the cost of some statistical resolving power. We will introduce some less restrictive assumptions for what follows, along with shorthand notation for improved readability (and to make it obvious which quantities are to be considered small). First, we require that the magnitude of the polarization vector is the same for both polarization states (within the present experiment, $|\vec{\boldsymbol{P}}_+| = |\vec{\boldsymbol{P}}_-|$ is correct to a high degree of precision), and also that the average of the magnitude of $\cos\theta$ for a given detector does not change when the polarization is flipped (equivalent to a requirement that the trap position doesn't change when the polarization is flipped). Then:

$$P := |\vec{\boldsymbol{P}}_{+}| = |\vec{\boldsymbol{P}}_{-}| \tag{1.31}$$

$$\langle|\cos\theta|\rangle_T := \langle|\cos\theta|\rangle_{\mathrm{T}+} = \langle|\cos\theta|\rangle_{\mathrm{T}-} \tag{1.32}$$

$$\langle|\cos\theta|\rangle_B := \langle|\cos\theta|\rangle_{\mathrm{B}+} = \langle|\cos\theta|\rangle_{\mathrm{B}-}, \tag{1.33}$$

and we can further define

$$c = \langle|\cos\theta|\rangle := \frac{1}{2}\left(\langle|\cos\theta|\rangle_T + \langle|\cos\theta|\rangle_B \right) \tag{1.34}$$

$$\Delta c = \Delta\langle|\cos\theta|\rangle := \frac{1}{2}\left(\langle|\cos\theta|\rangle_T - \langle|\cos\theta|\rangle_B \right) \tag{1.35}$$

and

$$\tilde{A} = \tilde{A}(E_\beta) := A_\beta \frac{v}{c} \tag{1.36}$$

$$\tilde{b} = \tilde{b}(E_\beta) := b_{\mathrm{Fierz}} \frac{mc^2}{E_\beta}, \tag{1.37}$$

$$\tilde{r} = \tilde{r}(E_\beta) := 1 + \tilde{b}. \tag{1.38}$$

With this new set of variables defined, we can re-write Eqs. (1.23-1.26) as

$$r_{\mathrm{T}+}(E_\beta) = W(E_\beta)\,\varepsilon_{\mathrm{T}}(E_\beta)\,\Omega_{\mathrm{T}}\,N_{+}\left[\tilde{r} + \tilde{A}P\left(c + \Delta c \right)\right] \tag{1.39}$$

$$r_{\mathrm{B}+}(E_\beta) = W(E_\beta)\,\varepsilon_{\mathrm{B}}(E_\beta)\,\Omega_{\mathrm{B}}\,N_{+}\left[\tilde{r} - \tilde{A}P\left(c - \Delta c \right)\right] \tag{1.40}$$

$$r_{\mathrm{T}-}(E_\beta) = W(E_\beta)\,\varepsilon_{\mathrm{T}}(E_\beta)\,\Omega_{\mathrm{T}}\,N_{-}\left[\tilde{r} - \tilde{A}P\left(c + \Delta c \right)\right] \tag{1.41}$$

$$r_{\mathrm{B}-}(E_\beta) = W(E_\beta)\,\varepsilon_{\mathrm{B}}(E_\beta)\,\Omega_{\mathrm{B}}\,N_{-}\left[\tilde{r} + \tilde{A}P\left(c - \Delta c \right)\right], \tag{1.42}$$

and the superratio becomes

$$s = \frac{\left(\tilde{r} + \tilde{A}Pc\right)^2 - \left(\Delta c\right)^2}{\left(\tilde{r} - \tilde{A}Pc\right)^2 - \left(\Delta c\right)^2} \tag{1.43}$$

where all factors of $W(E_\beta)$, $\varepsilon_{\mathrm{T}/B}(E_\beta)$, $\Omega_{\mathrm{T}/B}$, and $N_{+/-}$ have been cancelled out entirely.

For simplicity we take $\Delta c = 0$ in what follows. Although this is not strictly accurate within the present experiment, this assumption greatly simplifies the expressions that follow. Then, absent other corrections (*e.g.* backscattering, unpolarized background, ...), it is clear that if $\tilde{b} = 0$ as in the Standard Model,

$$A_{\text{super}} \;=\; \tilde{A}Pc \;=\; A_\beta \, \frac{v}{c} \, |\vec{P}| \, \langle |\cos\theta| \rangle \tag{1.44}$$

In the case where $\tilde{b} \neq 0$, we find that

$$\begin{aligned} A_{\text{super}} &= \frac{\tilde{A}Pc}{1+\tilde{b}} && (1.45) \\ &\approx \tilde{A}Pc\,(1 - \tilde{b} + \tilde{b}^2), && (1.46) \end{aligned}$$

where we have utilized the assumption that $\tilde{b} \ll 1$. Thus, to leading order in terms of $\tilde{b}$,

$$A_{\text{super}} \;\approx\; A_\beta \, \frac{v}{c} \, |\vec{P}| \, \langle |\cos\theta| \rangle \left(1 - b_{\text{Fierz}} \frac{mc^2}{E_\beta}\right). \tag{1.47}$$

In addition to eliminating systematic effects, the superratio asymmetry also provides an enhanced signal to be evaluated, as can be seen in Fig. 1.4. The price for this clear signal and reduction in systematics is, unfortunately, a decrease in overall statistical resolving power. Given the difficulty of controlling many of the cancelled systematics, this can potentially be a very good trade-off.

There are some limitations to what the superratio technique is able to deal with effectively, however — notably, scattering effects don't cancel out particularly well. Within the present project, this is a major systematic.

Scattering, unpolarized background, *and* the variety of effects effectively addressed by the superratio asymmetry construction are all included within the simulations to which the experimental data is compared, and the effects are propagated through the analysis to the end; although many systematic effects can be reduced by the technique described above, they must still be evaluated.

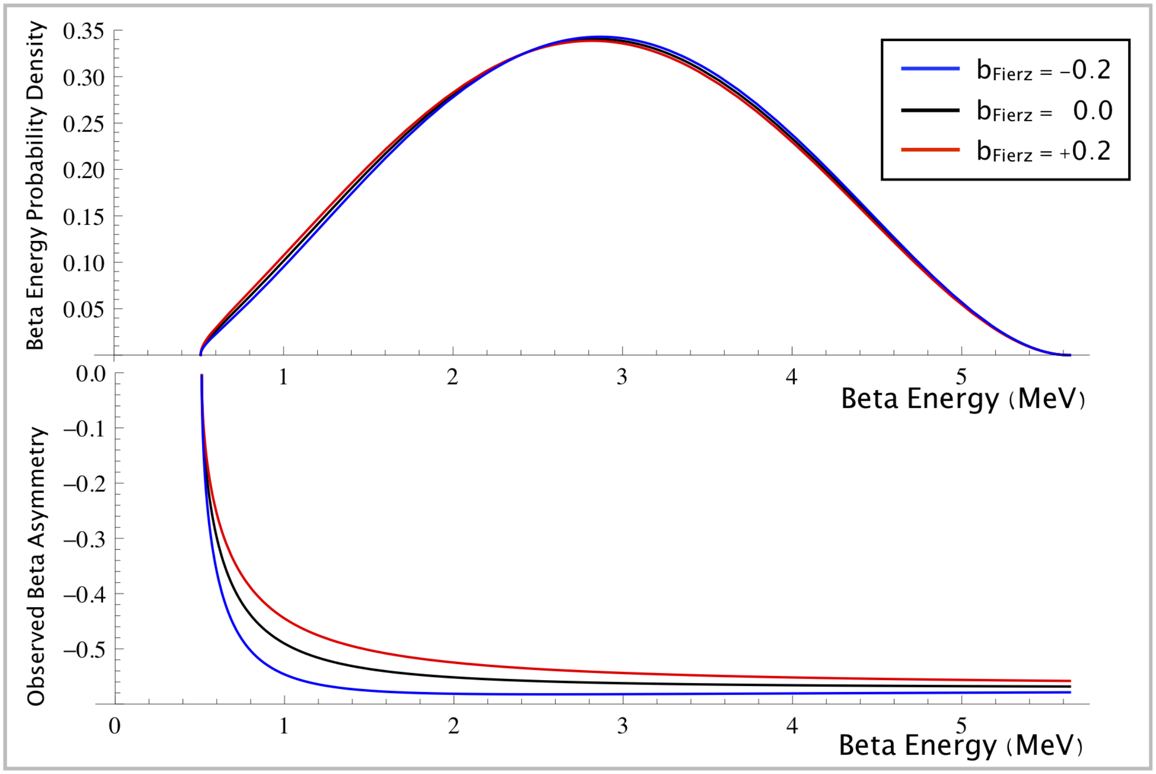

Figure 1.4: A generated beta energy spectrum (top), and the superratio asymmetry associated with it (bottom) are constructed to measure a b_{Fierz} signal at the values shown. The supersum method of Ref. [66] is roughly equivalent to constructing the top plot's beta energy spectrum. Note that the magnitude of these b_{Fierz} values has been made to be unphysically large so that the effect to the top plot can be seen; both scalar and tensor couplings of the size needed to produce this effect have already been ruled out.

1.7 The Gamow-Teller/Fermi Mixing Ratio and Related Constraints

It is clear from Sec. 1.5 that in order to make a prediction about the behaviour of outgoing particles within a particular beta decay transition, it is fundamentally important to know the value of the mixing ratio ρ.

Of course, it is possible to perform a relatively direct measurement of ρ through an observation of one of the other JTW parameters (e.g., a measurement of A_β in combination with Eq. (1.22) rapidly leads to a value for ρ.). However, this strategy has certain drawbacks – notably, the apparatus required to perform such a measurement *well* must be fairly complex; the TRINAT setup, for example, cannot readily be used with isotopes of most chemical elements.

For ^{37}K in particular, this direct approach *has* been used in the past, both with the present dataset as well as with previously collected data, yielding an overall value of $\rho = 0.576 \pm 0.006$ [63][57][67].

As we do not wish to re-use the same data twice within a single measurement, we take as our baseline the value of ρ as extracted in a more roundabout way as described below.

It is useful to define the strength, ft, of a transition — also known as the ft value. This is fundamentally an experimental quantity. Though the ft value is in principle the product of two quantities — the statistical rate function f and the partial half-life t — it is common to treat the product as a single unit. The statistical rate function f must be split into vector and axial components (f_V and f_A) in order be evaluated, and f_V in particular is often used alone, as we will see below. The statistical rate functions are, in essence, integrals over the accessible lepton phase space, and both f_V and f_A are mathematically non-trivial objects[68][69], but can be evaluated by, e.g., the methods of Refs. [70][71][72]. Such calculations are beyond the scope of the present work, however we will note that f_V and f_A are characterized primarily by the beta endpoint energy E_0 (scaling as $\sim E_0^5$), a quantity which can readily be measured.

The partial half-life t can be quickly calculated given knowledge of the total half-life $t_{1/2}$ and branching ratio R, as:

$$t \quad = \quad \frac{1}{R} \left(1 + P_{\mathrm{EC}}\right) \, t_{1/2}, \tag{1.48}$$

where P_{EC} is the electron capture probability (in the case of ^{37}K, $P_{\mathrm{EC}} = 0.0008$ makes only a small contribution [73]). It is also possible to write down an expression for t based on something closer to a first principles approach:

$$t \quad = \quad \frac{K}{G_F^2 \, V_{ud}^2 \left(f_V \, C_V^2 |M_F|^2 + f_A \, C_A^2 |M_{GT}|^2\right)}. \tag{1.49}$$

Here, $K = (\hbar c)^6 2\pi^3 \hbar \ln(2) (m_e c^2)^{-5}$ is a simple combination of physical constants, and, as described in Sec. 1.5, C_V (C_A) is the universal complex coupling parameter associated with vector (axial) currents, while M_F (M_{GT}) is the transition matrix element associated with vector (axial) coupling for a specific decay. G_F is the weak interaction coupling constant, which is measured experimentally through muon decay. V_{ud} is the up-down mixing element within the Cabibbo–Kobayashi–Maskawa (CKM) matrix; its precise determination is an active area of research, motivated in part by the attempt to search for or constrain the possible presence of a fourth generation of quarks.

It is worthwhile, at this stage, to briefly discuss the corrections to the Fermi and Gamow-Teller matrix elements, M_F and M_{GT}, that have already been implicitly applied. Although the uncorrected matrix elements M_F^0 and M_{GT}^0 are in some sense the more fundamental quantities, the corrected matrix elements are what is measured by an experiment. M_F^0 and M_{GT}^0 are related to their corrected counterparts according to:

$$|M_F|^2 = (1+\delta_R')(1+\delta_{NS}^V-\delta_C^V)(1+\Delta_R^V)\,|M_F^0|^2 \tag{1.50}$$
$$|M_{GT}|^2 = (1+\delta_R')(1+\delta_{NS}^A-\delta_C^A)(1+\Delta_R^A)\,|M_{GT}^0|^2, \tag{1.51}$$

where δ_C^V (δ_C^A) is the isospin symmetry breaking correction for the vector (axial-vector) current. Here, δ_R' is the portion of the outer radiative correction (*i.e.*, it is dependent on the specific transition in question) that depends *only trivially* on the nucleus; it is identically the same for vector and axial couplings. The δ_{NS}^V (δ_{NS}^A) term is the portion of the outer radiative correction for the vector (axial-vector) current with a *non-trivial* dependence on nuclear structure. These require a detailed shell model calculation to evaluate, as described in *e.g.* Refs. [74][75][76][77][78]. Finally, the quantities Δ_R^V and Δ_R^A arise from inner radiative corrections (*i.e.*, independent of the specific transition being considered) to the vector and axial-vector currents, and may be calculated as in Refs. [79][80][81][82]. Although they do not depend on the specifics of any transition, the Δ_R^V and Δ_R^A terms are included here within the expressions for (transition-specific) M_F and M_{GT} for our later convenience. This convention is sometimes, but not always, followed within the published literature [73][83].

We will now consider the special case of superallowed $0^+ \to 0^+$ decay (of which ^{37}K is *not* an example). As a general rule, these are strong, clean transitions which proceed only through vector coupling with no axial components. Quantitatively, this amounts to setting $M_{GT}^0 = 0$ and $M_F^0 = 2$ within Eq. (1.49). As always, $C_V = 1$ by construction. With all axial couplings eliminated completely, the superallowed $0^+ \to 0^+$ decays are ideal candidates for measurements of the fundamental vector coupling strength. If the conserved vector current (CVC) hypothesis holds (and there is some reason to believe that it does [84][83]), then this coupling strength is common to *all* transitions. We will soon see how knowledge of this absolute vector coupling strength taken from measurements of $0^+ \to 0^+$ decay allows us to make predictions about the decay of ^{37}K as well.

In practice, the ft values measured in superallowed $0^+ \to 0^+$ transitions need some small corrections in order to arrive at a universally applicable measure of the vector coupling strength. We define a corrected ft value for these transitions, $\mathcal{F}t^{0^+\to 0^+}$ (sometimes simply $\mathcal{F}t$), as:

$$\mathcal{F}t^{0^+\to 0^+} := (f_V t)\Big|_{0^+\to 0^+}(1+\delta_R')(1+\delta_{NS}^V-\delta_C^V) \tag{1.52}$$

$$= \frac{K}{2\,G_F^2\,V_{ud}^2(1+\Delta_R^V)}, \tag{1.53}$$

where we have made use of Eq. (1.49). Within Eqs. (1.52)-(1.53) above, only the parameters t and G_F are measured directly, while the other parameters must be calculated. If all measurements and calculations have been performed perfectly, then Eq. (1.52) is expected to yield the same $\mathcal{F}t$-value for *any* superallowed $0^+ \to 0^+$ transition, as the contributions from nuclear structure have all been removed. The above relationship is commonly used to extract an experimental value for V_{ud}, which cannot be calculated directly.

While Eq. (1.53) describes physical parameters that are universal, it is important to remember that we have only arrived at this result by specializing our description to the superallowed $0^+ \to 0^+$ transitions; Eqs. (1.52)-(1.53) are not applicable as-is to other types of transitions. It is, however, also possible to write down an analogous expression to describe the universal vector coupling strength using parameters related to other types of decays. As the axial current is not conserved, we will still only be interested in the vector components of such transitions, and it will take a bit more work to separate these out within a transition where both couplings contribute. We will consider the mixed (Fermi/Gamow-Teller) mirror decays (of which ^{37}K *is* an example). Again, $C_V = 1$ (it is a universal parameter), however for the case of mirror transitions, $M_F^0 = 1$ and $M_{GT} \neq 0$.

It is useful, at this stage, to recall the definition of ρ, the axial-vector/vector mixing ratio for a specific transition from Eq. (1.19). In the notation of Eqs. (1.50)-(1.51), we have:

$$\begin{aligned}
\rho &:= \frac{C_A\, M_{GT}}{C_V\, M_F} \\
&= \frac{C_A\, M_{GT}^0}{C_V\, M_F^0}\left[\frac{(1+\delta_{NS}^A-\delta_C^A)}{(1+\delta_{NS}^V-\delta_C^V)}\frac{(1+\Delta_R^A)}{(1+\Delta_R^V)}\right]^{1/2} &\quad (1.54)\\
&\approx \frac{C_A\, M_{GT}^0}{C_V\, M_F^0}. &\quad (1.55)
\end{aligned}$$

As before, we use Eq. (1.49) to write down $f_V t$, this time for the mixed mirror transitions:

$$\begin{aligned}
(f_V t)\bigg|_{\text{mirror}} &= \frac{K}{G_F^2 V_{ud}^2 C_V^2 |M_F|^2 \left(1+\frac{f_A}{f_V}\rho^2\right)} &\quad (1.56)\\
&= \frac{K}{G_F^2 V_{ud}^2 (1+\delta_R')(1+\delta_{NS}^V-\delta_C^V)(1+\Delta_R^V)\left(1+\frac{f_A}{f_V}\rho^2\right)} &\quad (1.57)
\end{aligned}$$

We now define a corrected $\mathcal{F}t$ value, $\mathcal{F}t^{\text{mirror}}$, for mirror transitions by applying the same nuclear structure corrections that were used in Eq. (1.52). Then:

$$\begin{aligned}
\mathcal{F}t^{\text{mirror}} &:= (f_V t)\bigg|_{\text{mirror}} (1+\delta_R')(1+\delta_{NS}^V-\delta_C^V) \\
&= \frac{K}{G_F^2 V_{ud}^2 (1+\Delta_R^V)\left(1+\frac{f_A}{f_V}\rho^2\right)} &\quad (1.58)
\end{aligned}$$

Using a measured value of ρ, it is possible to extract a measurement of V_{ud} from Eq. (1.58) above. However, as a separate measurement of ρ is not always available, it is perhaps more common to approach the above result as a way to *find* ρ. Comparing with Eqs. (1.53) and (1.58):

$$\mathcal{F}t^{0^+\to 0^+} = \frac{1}{2}\left(1+\frac{f_A}{f_V}\rho^2\right)\mathcal{F}t^{\text{mirror}}. \quad (1.59)$$

We see, perhaps counterintuitively, that Eq. (1.59) makes it possible to extract the value of ρ for one transition by using (in part) information measured in an entirely separate class of transitions.

Of course, this method for evaluating ρ relies on the accuracy and precision of the theoretical calculations involved to reach this point. It is worth noting that the lepton phase space integrals f_V and f_A for vector and axial couplings, which directly affect the extracted value of ρ in Eq. (1.59) above, are identically the same under the allowed approximation. However, when higher-order corrections are taken into account, they are found to differ by $\sim 0.9\%$ for the primary ^{37}K decay branch [85].

Chapter 2

An Overview of Selected Techniques in Atomic Physics

2.1 The Shake-off Electron Spectrum

Although the beta decay process is primarily concerned with the emission of beta particles (electrons or positrons) from a weak interaction that occurs within the nucleus, it is common for one or more *orbital* electrons to also be lost in the process. Although beta particles are emitted over a continuous energy spectrum, they commonly carry several MeV of kinetic energy. By contrast, an atomic electron that becomes unbound in this process is likely to only carry a few eV of kinetic energy. These are referred to as shake-off electrons (SOEs), since they are in some sense shaken off.

We will amend Eq. 1.9 to reflect the presence of N such SOEs within each decay event, as

$$^{37}\mathrm{K} \;\; \rightarrow \;\; ^{37}\mathrm{Ar}^{(N-1)+} + \beta^+ + \nu_e + N\, e_{\mathrm{SO}}, \tag{2.1}$$

where it is clear that, since the parent ^{37}K atom was electrically neutral before its decay by β^+ emission, the daughter ^{37}Ar will initially have an extra orbital electron (and therefore a negative net charge) if no electrons are shaken off. We also note that it is common for multiple SOEs to be created in a given decay event.

A further consideration is that the outer electron in an $^{37}\mathrm{Ar}^-$ ion is not bound[86], and in an electric field such as is present within our experimental chamber, this outer electron is removed immediately to be accelerated through the field, leaving behind a neutral ^{37}Ar atom. Although this is in principle a different physical loss mechanism, we will refer to unbound electrons resulting from either process as SOEs.

It is useful to consider the energy spectrum of these shake-off electrons. The most straightforward component of the SOE energy spectrum arises from the electrons that are lost immediately *after* the decay, and we take these to initially have 0 eV kinetic energy.

For the shake-off electrons arising from the nuclear decay process, the initial energy spectra for SOEs originating in a particular atomic orbital shell can be estimated according to the procedure outlined by J.S. Levinger in 1953 [87]. The strategy is to assume that the sudden approximation holds, meaning that the change in the shape of the potential well between initial and final states occurs so rapidly that the wavefunction of (in this case) the atomic electron does not have time to adapt. Then, one simply calculates the overlap in wavefunctions between the bound initial state and the eigenstates of the final post-decay system. The final state of the electron may be either bound or unbound, and analytic expressions to describe the energy of the unbound electrons may be obtained if the atom is treated as being hydrogenic — as ^{37}K is an alkali, this treatment is well justified.

Unfortunately, this treatment cannot determine the fractional contribution of each orbital to the total, nor can it determine the *number* of electrons likely to be removed in a single decay event. The implications of the SOE energy spectrum to the present experiment are discussed further in Chapter 5.5.

2.2 Zeeman Splitting

In the presence of an external magnetic field $\vec{B}$, the Hamiltonian associated with an atom's orbital electrons will acquire an additional "Zeeman Shift" term, given by [88]

$$H_{\text{Zeeman}} = -\vec{\mu} \cdot \vec{B}, \tag{2.2}$$

where $\vec{\mu}$ is the magnetic moment associated with the orbital under consideration. In the limit where the magnetic field is too weak to significantly disrupt the coupling between the electron's spin- and orbital angular momenta, $\vec{\mu}$ may be treated as being fixed with respect to changes in the magnetic field. It is this weak field regime which will be primarily of interest to us in work with magneto-optical traps.

With $\vec{\mu}$ fixed, it is clear that the magnitude of the energy shift must scale linearly with the strength of the magnetic field. In considering the perturbation to the energy of a particular *transition*, the perturbations to the initial and final states must of course be subtracted:

$$\Delta E_{\text{transition}} = -(\vec{\mu}_f - \vec{\mu}_i) \cdot \vec{B}. \tag{2.3}$$

2.3 Optical Pumping

The optical pumping process necessary for this work involves using a laser to stimulate atomic transitions. By applying a circularly polarized laser beam tuned to match the atomic resonance, the aggregate effect to the atoms on which the laser is incident is to introduce a biased random walk towards a state of high spin-polarization (sometimes called a *stretched state*). Although the transitions to which the laser couples are often thought of as atomic transitions, the coupling of angular momenta between orbital electrons and the nucleus results in *both* becoming polarized.

With every absorbed photon, one unit of angular momentum is transferred to the atom, and an orbital electron jumps to a higher energy level. By ensuring that the incident polarization laser is fully circularly polarized (and choosing an appropriate axis of quantization), it is possible to ensure that all the absorbed photons must *increase* the angular momentum projection quantum number. After absorbing a photon, the excited electron will eventually decay to a lower energy level, emitting a photon in the process. The emitted photon carries one unit of angular momentum, and is emitted in a random direction – therefore the resulting change in atomic angular momentum projection is also randomized, provided that there exists an available lower energy state for the orbital electron to decay into. When the electron has been moved to the maximally polarized ground state, it can no longer be excited by the laser beam that drove it there (assuming perfect circular polarization for the laser), because there is no excited state available with higher angular momentum.

Given that the process is accurately modeled as a biased random walk towards a particular state, it should be clear that once a majority of the atoms have arrived at the stretched state, the optical pumping process has progressively diminishing returns, as there are fewer and fewer unpolarized atoms available to be polarized. As a practical matter, the entire process takes several microseconds before the system arrives at something of a steady state, with depolarizing forces balanced against the optical pumping rate.

We now consider the two primary depolarization mechanisms. The first and most straightforward of these arises as a result of incomplete circular polarization in the optical pumping laser. The overall laser polarization can be represented as a linear combination of left-handed and right-handed ($\sigma_{\pm}$) circularly polarized components. If the σ_{+} light *increases* the angular momentum projection in the atomic system on which it is incident, then the σ_{+} light must necessarily *decrease* that same quantity. In practice, it is impossible to completely polarize the optical pumping laser, so it is inevitable that there will be some depolarizing component, however small, within the optical pumping laser.

The cloud polarization can also be disrupted by the presence of a non-uniform magnetic field as the result of Larmor precession. In a simplified semi-classical picture (which translates remarkably well to the quantum mechanical reality), this would result in any spins that are not fully aligned (or anti-aligned) with the magnetic field precessing about the local magnetic field lines. If the magnetic field is aligned with the intended axis of polarization, the spins will precess, but the overall polarization (ie, the spin projection onto the selected axis) will be unchanged.

By contrast, if the magnetic field is misaligned with the polarization axis, then a spin (even one initially aligned with the polarization axis) will experience a time-dependent depolarization force as it precesses. Worse yet, if the magnetic field is non-uniform, then the spins on one side of the atom cloud will precess about a different axis, at a different rate, than the spins on the opposite side.

This time-dependent depolarization mechanism is critical to nuclear magnetic resonance (NMR) measurements, but for our purposes here, we wish to suppress it. To minimize depolarization effects arising from magnetic field non-uniformities, an additional uniform magnetic field may be applied along the axis of polarization. This has the effect of decreasing the *fractional* size of any non-uniformities that may be present. The applied field must also be kept relatively small ($\sim$ 2.3 Gauss, in our case) in order to prevent the atomic and nuclear angular momenta from becoming decoupled. The optical pumping process is described in more detail within our collaboration's

Ref. [89].

2.4 Doppler Cooling

We consider a setup in which a cloud of two-level atoms lies along the path of two counter-propagating laser beams, both tuned to resonance. For simplicity, we treat this cloud as being one dimensional along the axis of laser propagation. With two counter-propagating laser beams of equal intensity and detuning, the "push" from interaction with one beam is, on average within the lab frame, perfectly counteracted by the push from the opposite-propagating beam, so there is no net velocity transfer to a cloud initially at rest. These pushes, however, are applied on the level of the individual atom, and are the result of individual photons being absorbed and emitted. Because this process is probabilistic rather than deterministic, each individual atom will undergo a random walk.

We now consider the effect of detuning on this process. We will suppose that both lasers are equally detuned slightly to the red of resonance. This will obviously decrease absorption by atoms at rest within the lasers' path – however the atoms within the cloud are not at rest, but rather are undergoing thermal motion. As such, within the rest frame of each individual atom, the two laser beams will appear to be Doppler shifted in opposite directions, with the sign dependent on atomic motion. In particular, atoms moving against a laser's direction of propagation will see that laser beam as being blueshifted within their own rest frame. Since the laser was redshifted relative to resonance within the lab frame, adding an additional blueshift will serve to bring the photons' energy back towards resonance, making them more likely to be absorbed. For this same atom, the laser propagating in the same (lab frame) direction as the atom itself will appear further redshifted, and its photons are less likely to be absorbed.

The result of many such atom-photon interactions is that an individual atom, no matter which way it's moving at any given time, will absorb more photons from the direction where the momentum transfer slows them down, and fewer from the direction where the momentum transfer speeds them up. In short, each individual atom is *greatly* slowed down. At the macroscopic level, this translates to a decrease in the *temperature* of the atom cloud. Such a setup is sometimes referred to as a (one-dimensional) "optical molasses" due to the viscous drag force induced on atomic motion, and it is straightforward to extend this model to three dimensions.

Although this setup will decrease atomic velocity, it does not create a confining force, so (eg, in three dimensions) the atoms are still free to move out of the lasers' path, albeit at a decreased speed.

2.5 Atom Trapping with a Magneto-Optical Trap

Since its initial description by Raab et. al. in 1987 [90], the magneto-optical trap (MOT) has become a widely used technique in many atomic physics laboratories. The MOT produces confined samples of cold, electrically neutral and isotopically pure atoms confined within a small spatial region. It is these properties that make the MOT a valuable tool not only in atomic physics, but for precision measurements in nuclear physics as well, and the TRINAT collaboration has adopted the technique wholeheartedly.

The technique is used predominantly with alkalis due to their simple orbital electron structure, and once set up it is quite robust. The MOT's trapping force is specific to the isotope for which the trap has been tuned. This feature makes it ideal for use in precision radioactive decay experiments, since the daughters are unaffected by the trapping forces keeping the parent confined.

A MOT combines the slowing features of an optical molasses (Sec. 2.4) with the Zeeman splitting (Sec. 2.2) arising from a quadrupolar magnetic field to produce a robust and isotope-specific trapping force in all three dimensions.

A MOT can be created from relatively simple components: a quadrupole-shaped magnetic field, typically generated by two current-carrying coils of wire, and a circularly polarized laser tuned to match one or more atomic transitions in the isotope of interest. Because a MOT is easily disrupted by interactions with untrapped atoms, the trap must be created within a vaccuum system. Finally, a source of atoms to be trapped is required. See Fig. 2.1.

The quadrupolar magnetic field is typically generated using a set of two current carrying electrical coils in a geometry similar to a Helmholtz coil, but with the two coils' currents flowing anti-parallel to one another. This anti-Helmholtz coil is constructed to surround the trapping region, and introduces a quadrupolar magnetic field. Within the central region where the trap is located, the magnetic field $\vec{B}$ has the approximate shape,

$$\vec{B} = 2B_0 z\,\hat{z} - (B_0 x\,\hat{x} + B_0 y\,\hat{y}), \tag{2.4}$$

where B_0 represents the overall strength of the magnetic field, $\hat{x}$, $\hat{y}$, and $\hat{z}$ are coordinate unit vectors such that the $\hat{z}$ axis points along the axis of the anti-Helmholz coil, and x, y, and z represent the position (relative to the central point between the two coils) at which the magnetic field is being described. In particular, this implies that the field magnitude is zero at the centre, and increases linearly in every direction as one moves away from the centre.

The retroreflecting lasers are red-detuned and circularly polarized in a direction selected to couple to the Zeeman shifted energy level which will push a given atom towards the centre. This provides a restoring force in all three dimensions to atoms that have moved too far from the centre. See Fig. 2.1.

2.6 The AC-MOT

One specialized type of magneto-optical trap, the AC-MOT, allows for the trap's magnetic field to be rapidly shut off. First described by Harvey and Murray in 2008 [92], the AC-MOT is so named because of the sinusoidal alternating current (AC) used in its anti-Helmholtz coils — in contrast to the constant direct current used in a typical MOT (hereafter referred to as a DC-MOT to eliminate ambiguity). Although the DC-MOT's robust trapping mechanism cannot be fully matched by a similar AC-MOT, the DC-MOT is very slow to turn off, and it is this latter consideration that has led the TRINAT collaboration to implement an AC-MOT in its second trap.

Although the trapping mechanism itself can be rapidly destroyed in both an AC- and DC-MOT by simply shutting off the trapping lasers, the DC-MOT's magnetic field is comparatively slow to dissipate and challenging to control during this time. Because the optical pumping process necessary to spin-polarize the atoms requires a uniform magnetic field over the region of interest (in contrast to the uniform magnetic field *gradient* needed for a functional MOT), we do not consider the MOT to have been fully shut off until any residual magnetic fields have completely dissipated. Put another way, for optical pumping, a weak dipole-shaped magnetic field is preferred,

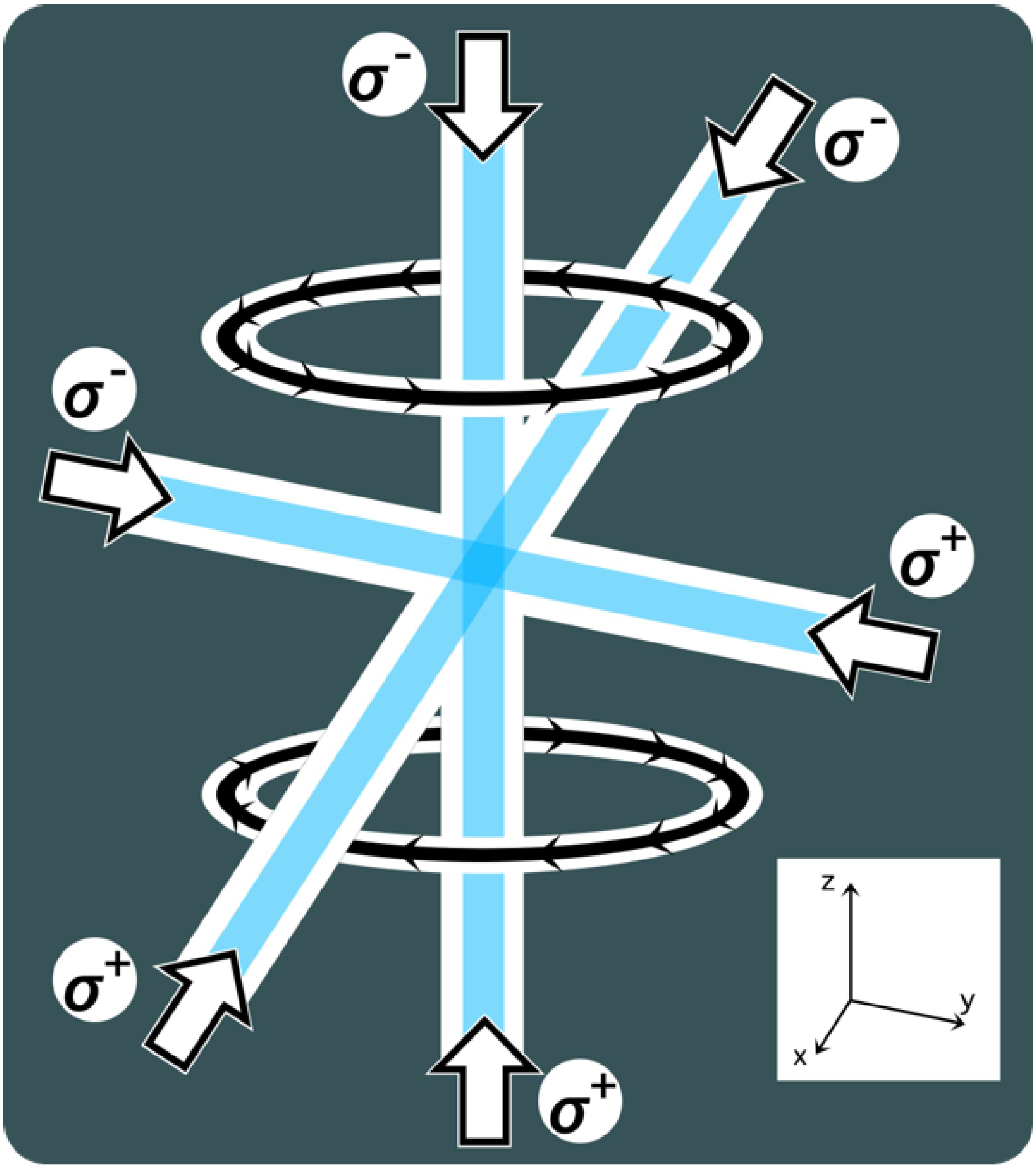

Figure 2.1: Components of a magneto-optical trap, including counterpropagating circularly polarized laser beams (with $\sigma^{\pm}$ polarization) intersecting at the centre, and current-carrying electrical coils above and below the central intersection point, used to generate a magnetic field gradient. With antiparallel currents, the magnitude of the field in the region near the centre is linear in all directions. Diagram taken from [91]

.

and this is not possible while the MOT's quadrupole field is in place.

With the DC-MOT designed to operate continuously, it should be unsurprising that it is fairly slow to turn off. The limiting factor is the speed at which the magnetic field can be eliminated; it is particularly problematic when electrically conductive materials are present nearby, as is the case for our experimental chamber. This is because a rapidly changing magnetic field will necessarily induce an electrical potential, producing a current in any nearby conductors. These induced eddy currents will, themselves, produce a magnetic field and further eddy currents as that magnetic field dissipates. The result is a magnetic field which is slow to dissipate and difficult to control during the dissipation process. In general, the atoms do not remain reliably confined while the magnetic field dissipates, as the field during this time may include anomalies which could result in atoms actively being pushed out of the trap by the trapping lasers. For similar reasons, the atoms also cannot be successfully polarized during this time period.

It is clearly important that as little time as possible be wasted in this intermediate stage where the atoms can neither be confined nor polarized. The more straightforward reason behind this is simply that any time wasted during beamtime is data lost. A slightly more subtle but related reason is that when the trapping mechanism is removed, the atom cloud undergoes thermal expansion ($\sim$1 mK). If the cloud is retrapped quickly enough, the whole process can be done with minimal atom loss — however once the cloud has dissipated it cannot be re-trapped, as the trapping forces act on only a small spatial region.

The principle behind the AC-MOT is to simply run a sinusoidal current through one's anti-Helmholtz coils while flipping the laser polarization to remain in sync with the magnetic field. Crucially, the phase of the magnetic field will lag somewhat behind the phase of the current in the anti-Helmholtz coils, as a result of induced eddy currents in nearby materials. The precise amount of phase lag in a given system is a function both of the geometry and electrical impedence properties of the nearby materials, as well as the frequency of the sinusoid.

Chapter 3

The Experimental Setup

3.1 An Overview of the Double MOT System and Duty Cycle

The experimental subject matter of this thesis was conducted at TRIUMF using the apparatus of the TRIUMF Neutral Atom Trap (TRINAT) collaboration. The TRINAT laboratory offers an experimental set-up which is uniquely suited to precision searches for exotic beta decay physics by virtue of its ability to produce highly localized samples of cold, isotopically pure atoms within an open detector geometry. Although the discussion in this chapter will focus on the methodologies used to collect one particular dataset, taken over approximately 7 days of beamtime in June 2014, the full apparatus and the techniques used are fairly versatile, and can be (and have been) applied to several related experiments using other isotopes.

The TRINAT lab accepts radioactive ions delivered by the ISAC beamline at TRIUMF. These ions are collected on the surface of a hot zirconium foil where they are electrically neutralized, and subsequently escape from the foil into the first of two experimental chambers (the "collection chamber"). Further details on the neutralization process are presented in a previous publication [93]. The collection chamber is held at ultra-high vacuum (UHV) to facilitate continuous collection of one specific isotope – for the purposes of this thesis, ^{37}K – into a MOT from the tail end of the thermal distribution. Although this procedure preferrentially traps only the slowest atoms, once trapped, atoms will be cooled further as a side-effect of the MOT's trapping mechanism. The result is a small ($\sim 1\,$mm diameter), cold ($\sim 1\,$mK) cloud of ^{37}K

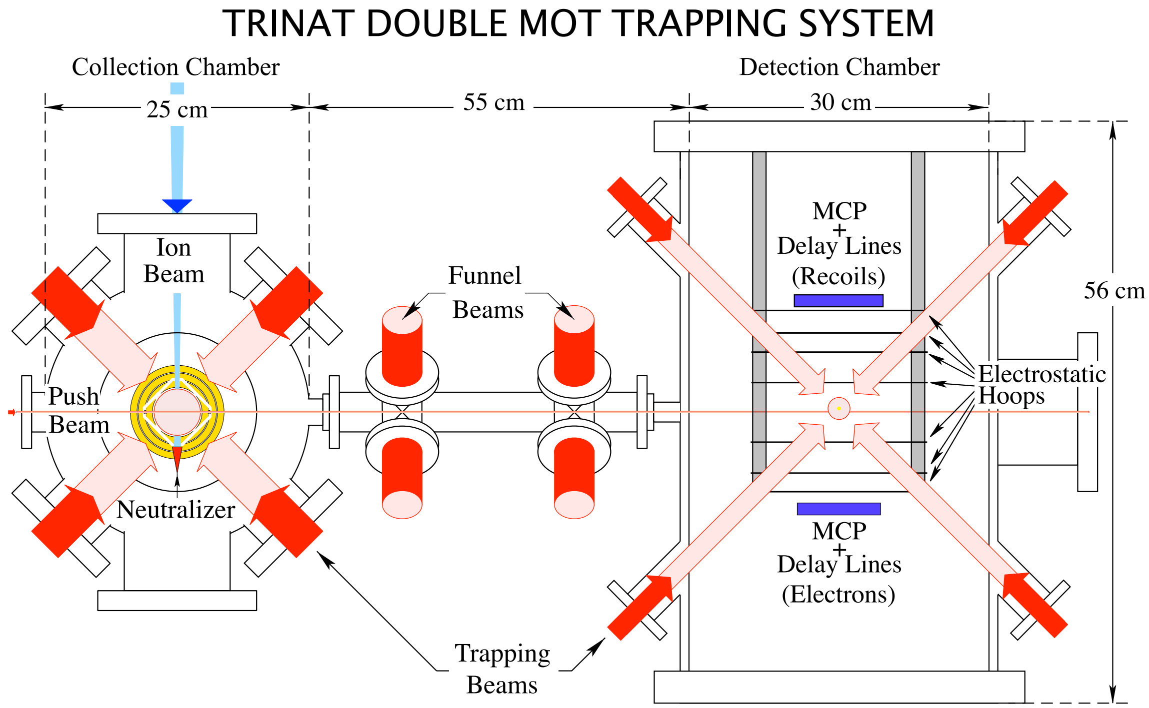

Figure 3.1: The TRINAT experimental set-up, viewed from above. Ions from the beamline pass through the collection chamber onto the neutralizer, which is held at ground. The neutralizer is heated to release the neutral atoms from its surface back into the collection chamber, where some are collected into a MOT. Atoms from the collection chamber's MOT are transferred directly into the detection chamber's MOT approximately once per second, kept focused during the transfer by funnel beams (lasers). Within the detection chamber, background events are dramatically reduced.

atoms.

These properties of the atomic cloud allow for a relatively clean transfer into the second chamber (the "detection chamber"), where they are loaded into a second MOT (see Fig. 3.1). This two MOT approach to the experiment, and the isotope-specific transfer mechanism needed to execute it, was developed primarily as a way to eliminate background events and the beamline contaminants that give rise to them.

The key to the atom transfer mechanism is, in essence, simply a properly tuned laser beam to push the atoms out of the first trap and into the second. The push beam is frequency-tuned such that it can be absorbed by atoms trapped within the first MOT, and pulsed ($\sim$30 ms on) to initiate the transfer. When a trapped atom absorbs a photon from the push beam, there is a transfer of linear momentum, causing the atom to escape the MOT's potential well and continue along into the detection chamber.

To help keep the atoms focused during the transfer, two sets of (laser) funnel beams are placed along the transfer path, together with current-carrying coils to maintain the desired magnetic field in the region where the funnel beams interact with atoms in transit. Each set of funnel beams behaves very much like a two-dimensional MOT, confining and cooling the atoms along the two perpendicular axes as they pass by.

Transferred atoms are guided by the push beam into the detection chamber; the push beam is directed towards a position several millimetres above the pre-existing cloud of trapped atoms there. This is an intentional design choice to prevent atoms from being ejected from the second trap by the push beam that was intended to load it, while simultaneously taking advantage of the gravitational force's tendency to push the atoms slightly down, away from the push beam's path and towards the true location of the second trap. The transfer methodology is discussed in further detail within the collaboration's Ref. [94], though some aspects of the experimental setup have changed in the intervening years.

This push beam setup is able to reliably load approximately 80% of the atoms originally held in the first trap into the second, with the transferred atoms themselves moving at $\sim$40 m/s [94]. In combination with lead shielding between the two chambers, the end result is a significant reduction of background events measured within the detection chamber. During regular operation, atoms are transferred approximately once per second (a timescale comparable to the $\sim$1.2 second half-life of ^{37}K).

We now turn our attention to what happens to the atom cloud in the detection chamber between loading phases (see Fig. 3.2). One of the goals for the 2014 ^{37}K beamtime required that the atom cloud must be spin-polarized, as well as being cold and spatially confined. Although the MOT makes it straightforward to produce a cold and well confined cloud of atoms, it is fundamentally incompatible with techniques to polarize these atoms. The physical reasons behind this are discussed in Section 3.2.

Once the newly transferred set of ^{37}K atoms has been collected into the cloud, the entire MOT apparatus cycles 100 times between a state where it is 'on' and actively confining atoms, and a state where it is 'off' and instead the atoms are spin-polarized by optical pumping while the atom cloud expands ballistically before being re-trapped. These 100 on/off cycles take a combined total of 488 ms. The laser components of

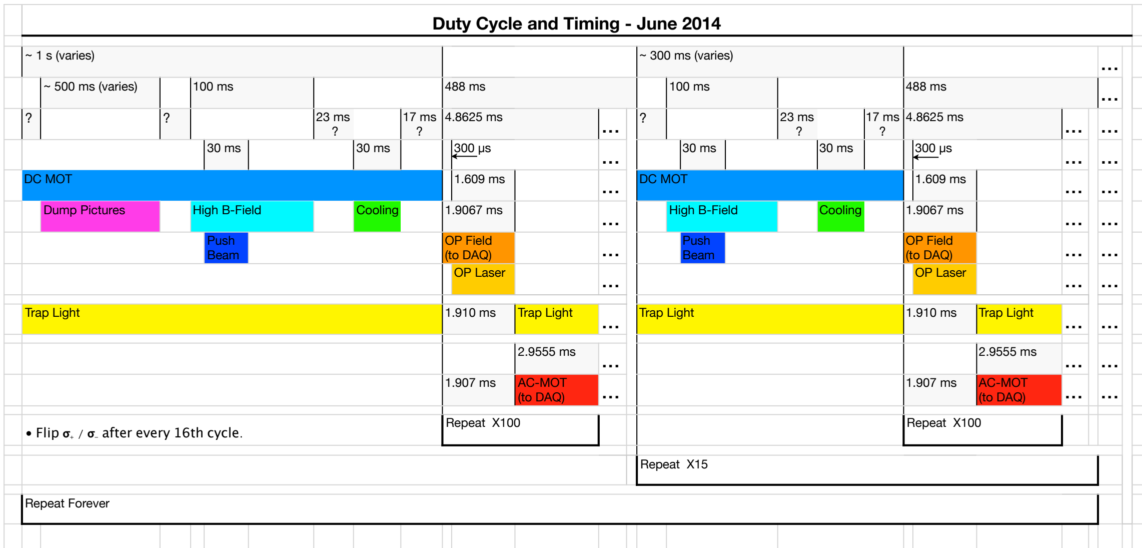

Figure 3.2: The duty cycle used for transferring, cooling, trapping, and optically pumping ^{37}K during the June 2014 experiment. Not drawn to scale. Question marks indicate timings that varied either as a result of electronic jitter or as a result of variable times to execute the control code. Atoms are transferred during operation of the DC-MOT. Though the push beam laser itself is only on for 30 ms, the bulk of the DC-MOT's operation time afterwards is needed to collect and cool the transferred atoms. After 100 on/off cycles of optical pumping and the AC-MOT, the DC-MOT resumes and the next group of atoms is transferred in. After 16 atom transfers, the polarization of the optical pumping laser is flipped to spin-polarize the atoms in the opposite direction, in order to minimize systematic errors.

the trap are straightforward to cycle on and off on these timescales, but the magnetic field is much more challenging to cycle in this manner.

Immediately following each set of 100 optical pumping cycles, another set of atoms is transferred in from the collection chamber to the detection chamber, joining the atoms that remain in the trap (see Fig. 3.2). The details of the trapping and optical pumping cycles are described further in Section 3.2, and the optical pumping technique and its results for this beamtime are the subject of a recent publication [89].

3.2 The AC-MOT and Polarization Setup

Within the TRINAT detection chamber an AC-MOT is used for atom trapping, because it enables the MOT's polarization-destroying magnetic field non-uniformities to be quickly eliminated when the MOT is shut off. Despite the added complication, the AC-MOT allows for a duty cycle in which the ^{37}K atoms are alternatingly trapped and then polarized. Some details of the present implementation of the AC-MOT are given in Ref. [91], done with a separate MOT geometry from this beta decay work. A diagram of showing the operation phases of several key components in our AC-MOT/optical pumping duty cycle is shown in Fig. 3.3.

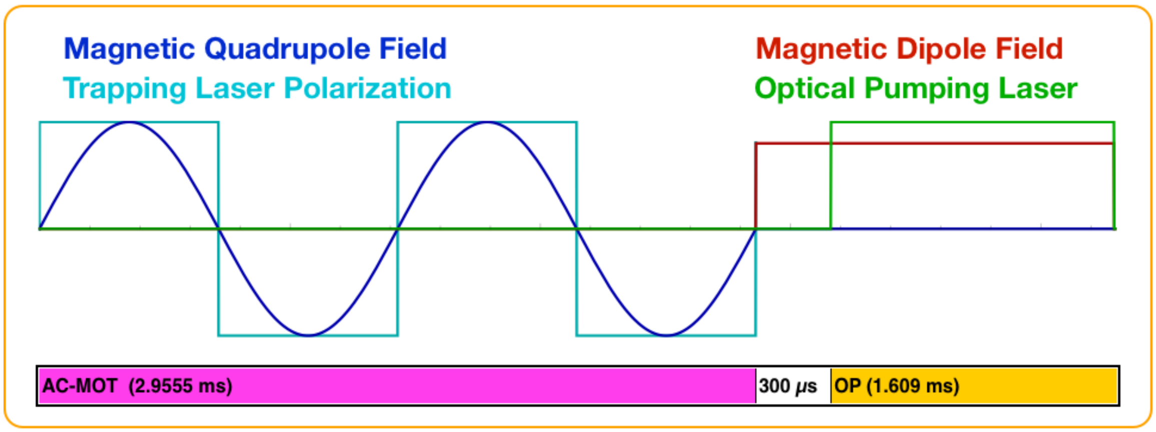

Figure 3.3: One cycle of trapping with the AC-MOT, followed by optical pumping to spin-polarize the atoms. After atoms are transferred into the science chamber, this cycle is repeated 100 times before the next transfer. The magnetic dipole field is created by running parallel (rather than anti-parallel as is needed for the MOT) currents through the two coils.

As alluded to in the previous section (3.1), the measurements in question required a spin-polarized sample of atoms, and a precise knowledge of what that polarization was. This is needed in order to make best use of the superratio asymmetry for both A_β and b_{Fierz} measurements. [63][89].

A MOT requires a quadrupolar magnetic field, and we generate ours with two current-carrying anti-Helmholtz coils located within the vacuum chamber itself. Since these coils are expected to run an alternating current, heat is produced and cannot be dissipated in the vacuum. Therefore the coils themselves are hollow copper tubes, and they are continuously cooled by pumping temperature-controlled water through them.

We spin-polarize ^{37}K atoms within the trapping region by optical pumping (See Ch. 2.3) [89]. In order to optimally polarize a sample of atoms by this method, it is necessary to have precise control over the magnetic field. In particular, the magnetic field must be aligned along the polarization axis, and it must be uniform in magnitude over the region of interest. Note that this type of magnetic field is not compatible with the MOT, which requires a uniform magnetic field *gradient* in all directions (characteristic of a quadrupolar field shape), and has necessitated our use of the AC-MOT.

With ambient magnetic fields from, e.g., the TRIUMF cyclotron and the earth, it is necessary to have available a means to cancel these fields out if we hope to create a well controlled, uniform magnetic field directed along the polarization axis within the trapping region — a necessity for optical pumping.

To this end, the time-constant ambient fields were trimmed in all dimensions using two horizontal pairs of Helmholtz coils along the horizontal axes, and the AC-MOT coils for the vertical direction. These magnetic fields were first trimmed to be near zero using a three-axis giant magnetoresistance 3-axis probe near the chamber center, with the microchannel plate (MCP) assembly removed and the vacuum chamber open to air. Final trimming was done by optimizing the polarization of (stable) ^{41}K atoms with the apparatus assembled. Some details are provided in the supplemental material of Ref. [63].

The AC-MOT and optical pumping magnetic fields were generated using Stanford Research Systems' DS345 arbitrary waveform generators, and amplified by two Matsusada DOP 25-80 bipolar amplifiers (20 kHz bandwidth, with $\pm$25 V and $\pm$80 A). The waveforms were carefully trimmed in shape, time, and amplitude to minimize magnetic fields resulting from induced from eddy currents during the optical pumping cycle, again with the MCP assembly removed and the vacuum chamber kept open to air.

Because the amplifiers' bandwidth was inadequate when using current control mode, so voltage control had to be used instead, allowing only for indirect control of the current. This proved to be a much more time consuming process, requiring empirical iteration. These waveforms used are not the same for the top and bottom coils, as during the optical pumping cycle one coil had to be flipped with respect to the MOT cycle to create the uniform vertical field for optical pumping by a Helmholtz rather than anti-Helmholtz configuration.

The full beta detector assemblies were in place during the field trimming, including a sheet of mu-metal wrapped about the scintillators as a magnetic shield.

All materials near the trap were chosen to minimize both magnetic permeability (to suppress time-constant magnetic field gradients) and conductivity (to suppress eddy currents arising from varying magnetic fields which, themselves, induce a time-varying magnetic field). For example, the electrodes controlling the in-chamber electric fields are made from either glassy carbon semiconductor or titanium alloy. We found that a copper ring (not pictured in Fig. 3.4) with a slit, mounted on each beta detector's stainless steel reentrant flange (directly above and below the trap's (anti-)Helmholtz coils), suppresses the worst eddy currents fighting the magnetic field along the vertical axis. The efficacy of these designs were all confirmed by finite element calculations of another collaboration member.

Ambient magnetic field changes of ~50 milliGauss could cause some polarization perturbations at the precision achieved, but the stray fields were kept under control at that level. The TRINAT lab is in a basement, well shielded from the experimental hall by concrete with rebar, and though 50 mG fields are seen in that hall from an open Helmholtz ion trap, they and the nearby 5-ton crane produce negligible fields when measured at the atom trap. The cyclotron field is ~0.5 Gauss, predominantly vertical, but TRINAT's Helmholtz trim coils are adjusted during calibrations with cyclotron both on and off — and of course the cyclotron is on with a constant field during the ^{37}K delivery. Furthermore, because we switched every few hours between the using the eMCP and rMCP, we were able to rule out the possibility that the polarization might have drifted but escaped notice.

3.3 Measurement Geometry and Detectors

The TRINAT detection chamber operates at UHV and provides not only the apparatus necessary to intermittently confine and then spin-polarize atoms, but also the variety of detectors and implements required to quantify their position, temperature, and polarization. The detection chamber further boasts an array of electrostatic hoops to collect both positively and negatively charged low energy particles into two opposing MCP detectors, each backed by a set of delay lines to measure hit position, and a further set of two beta detectors positioned across from each other along the polarization axis, each of which consists of a 40x40 pixel double-sided silicon strip detector (DSSD) and a scintillator coupled to a photomultiplier tube (PMT) (see Fig. 3.4). The chamber also includes 6 viewports specifically designed to be used for the trapping and optical pumping lasers (see Fig. 3.5.).

3.4 Microchannel Plates and Electrostatic Hoops

Two stacks of microchannel plates (MCPs) have been placed on opposing sides of the chamber, and perpendicular to the axis of polarization. Each stack of MCPs is a relatively large detector backed by a series of delay lines for position sensitivity. These two MCP detectors are designed to operate in conjuction with a series of seven electrostatic hoops positioned within the chamber and connected to a series of high voltage power supplies. The hoops' shape and position have been chosen such that they are able to maintain a constant, nearly uniform electric field across the space between the two MCP detectors, without blocking the necessary laser beams used for trapping, optical pumping, and photoionization, and without blocking the paths to the detectors of particles originating from the central cloud. The resulting electric field acts to pull positively charged ions towards one MCP detector and negatively charged electrons towards the other (see Figs. 3.4 and 3.5).

The detector intended to collect the negatively charged electrons (the eMCP) has an active area of 75.0 mm, and is positioned 100.0 mm from the chamber centre. It features a Z-stack configuration of three plates, and it is backed by a set of three separate delay lines in a hexagonal arrangement for redundant position sensitivity (the "HEX75"). The detector used to collect positively charged ions (the iMCP, or equivalently the rMCP – since many of the ions collected are recoils from decay) is 80.0 mm in diameter and positioned 101.4 mm from the chamber centre. It features only two plates arranged in a chevron configuration, and it is backed by a set of two separate delay lines (the "DLD80") for position sensitivity. In the context of the present work, the rMCP data is used primarily in conjuction with the photoionization laser to characterize the atom cloud (Section 3.6), while the eMCP data is used, together with the beta detectors, as a tag for decay events originating from the cloud.

3.5 Beta Detectors

The beta detectors, located above and below the atom cloud along the axis of polarization (Fig. 3.4), are each the combination of a plastic scintillator and a set of

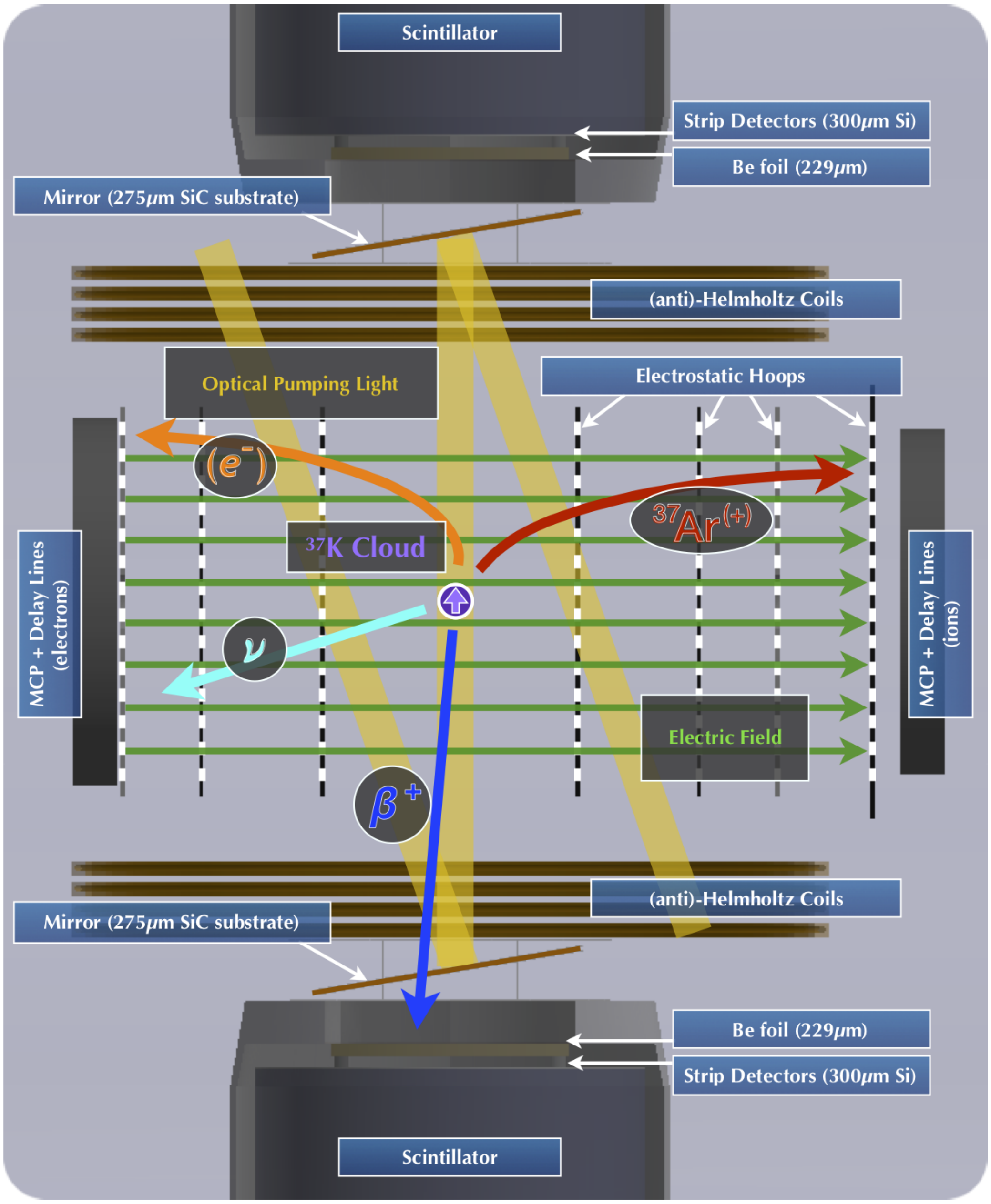

Figure 3.4: A scale diagram of the interior of the TRINAT detection chamber, shown edge-on with a decay event. After a decay, the daughter will be unaffected by forces from the MOT. Positively charged recoils and negatively charged shake-off electrons are pulled towards detectors in opposite directions. Although the β^+ is charged, it is also highly relativistic and escapes the electric field with minimal perturbation.

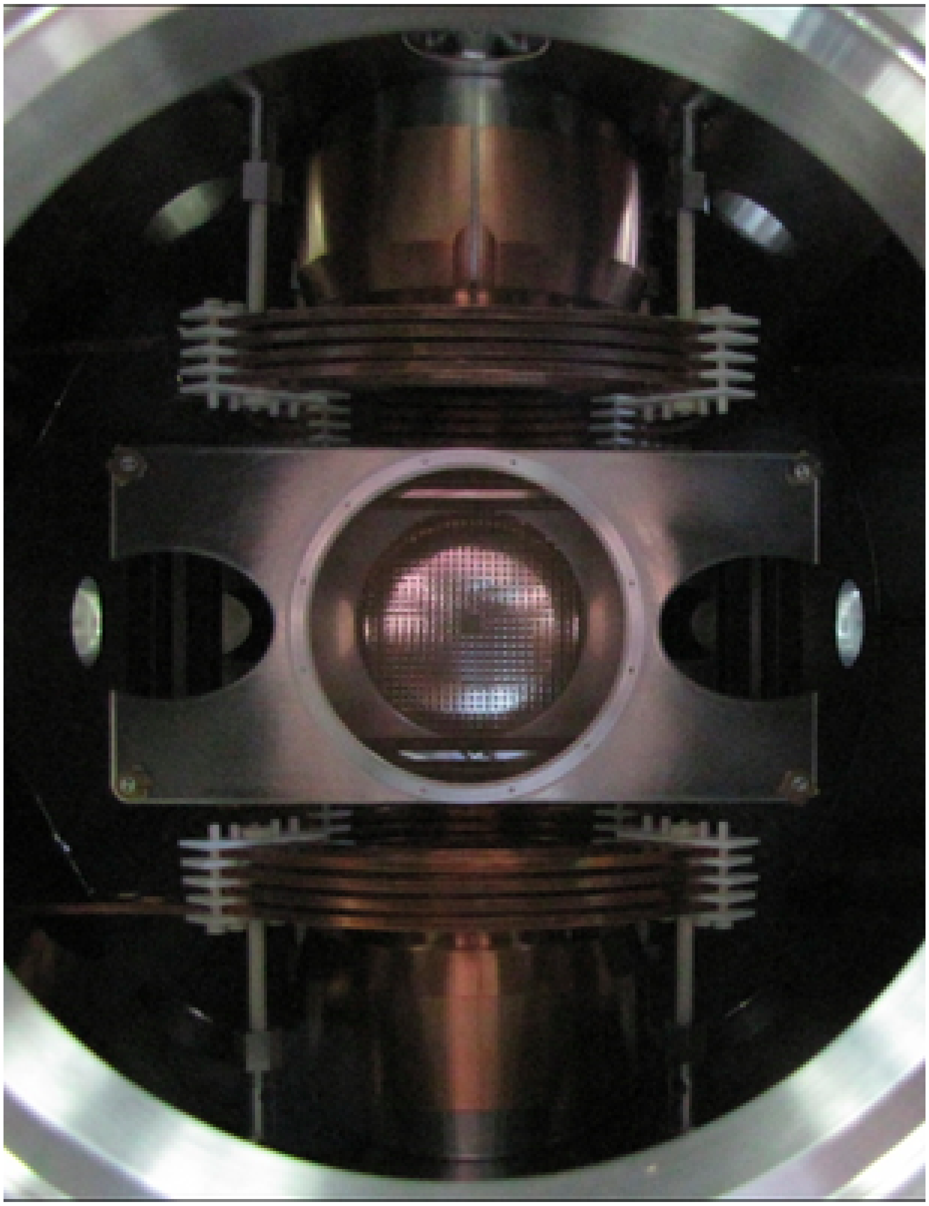

Figure 3.5: Inside the TRINAT detection chamber. This photo is taken from the vantage point of one of the microchannel plates, looking into the chamber towards the second microchannel plate. The current-carrying copper Helmholtz coils and two beta telescopes are visible at the top and bottom. The metallic piece in the foreground is one of the electrostatic hoops used to generate an electric field within the chamber. The hoop's central circular hole allows access to the microchannel plate, and the two elongated holes on the sides allow the MOT's trapping lasers to pass unimpeded at an angle of 45 degrees 'out of the page'.

silicon strip detectors. Using all of the available information, these detectors are able to reconstruct the energy of an incident beta, as well as its hit position, and provide a timestamp for the hit's arrival. Together the upper and lower beta detectors subtend approximately 1.4% of the total solid angle as measured with respect to the cloud position.

The two sets of beta detectors were positioned directly along the axis of polarization. Each beta detector consists of a plastic scintillator and photo-multiplier tube (PMT) placed directly behind a 40×40-pixel double-sided silicon strip detector (DSSD). The scintillator is used to measure the overall energy of the incoming particles, as well as to assign a timestamp to these events, while the DSSD is used both to localize the hit position to one (or in some cases, two) individual pixel(s), and also to discriminate between different types of incoming particles. In particular, though the scintillator will measure the energy of an incoming beta or an incoming gamma with similar efficiency, the beta will lose a portion of its kinetic energy as it passes through the DSSD into the scintillator. By contrast, an incident gamma will deposit only a very small amount of energy in the DSSD layer, making it possible to reject events with insufficient energy deposited in the DSSD as likely gamma ray events. Given that the decay of interest to us emits positrons, we expect a persistent background 511 keV gamma rays that are not of interest to us, so it is extremely important that we are able to clean these background events from our spectrum.

It must be noted that the path between the cloud of trapped atoms and either beta detector is blocked by two objects: a 275 μm silicon carbide mirror (necessary for both trapping and optical pumping), and a 229 μm beryllium foil (separating the UHV vacuum within the chamber from the outside world). In order to minimize beta scattering and energy attenuation, these objects have had their materials selected to use the lightest nuclei with the desired material properties, and have been manufactured to be as thin as possible without compromising the experiment. As the $^{37}\text{K} \rightarrow {}^{37}\text{Ar} + \beta^+ + \nu_e$ decay process releases $Q = 5.125\,\text{MeV}$ of kinetic energy [95], the great majority of betas are energetic enough to punch through both obstacles without significant energy loss before being collected by the beta detectors.

3.6 The Photoionization Laser

In order to measure properties of the trapped ^{37}K cloud, a 10 kHz pulsed laser at 355 nm is directed towards the cloud. These photons have sufficient energy to photoionize neutral ^{37}K from its excited atomic state, which is populated by the trapping laser when the MOT is active, releasing 0.77 eV of kinetic energy, but do not interact with ground state ^{37}K atoms. The laser is of sufficiently low intensity that only $\sim 1\%$ of excited state atoms are photoionized, so the technique is only very minimally destructive.

Because an electric field has been applied within this region (Section 3.4) the ^{37}K$^+$ ions are immediately pulled into the detector on one side of the chamber, while the freed e^- is pulled towards the detector on the opposite side of the chamber. Because ^{37}K$^+$ is quite heavy relative to its initial energy, it can be treated as moving in a straight line directly to the detector, where its hit position on the microchannel plate is taken as a 2D projection of its position within the cloud. Similarly, given a sufficient understanding of the electric field, the time difference between the laser pulse and the microchannel plate hit — which we will sometimes refer to as a time of flight (TOF) — allows for a calculation of the ion's initial position along the third axis.

With this procedure, it is possible to produce a precise map of the cloud's position and size, both of which are necessary for the precision measurements of angular correlation parameters that are of interest to us here. However, it also allows us to extract a third measurement: the cloud's polarization.

The key to the polarization measurement is that only atoms in the excited atomic state can be photoionized via the 355 nm laser. While the MOT runs, atoms are constantly being pushed around and excited by the trapping lasers, so this period of time provides a lot of information for characterizing the trap size and position. When the MOT is shut off, the atoms quickly return to their ground states and are no longer photoionized until the optical pumping laser is turned on. As described in Section 2.3, and in greater detail in [89], the optical pumping process involves repeatedly exciting atoms from their ground states until the atoms finally cannot absorb any further angular momentum and remain in their fully-polarized (ground) state until they are perturbed. Therefore, there is a sharp spike in excited-state atoms (and therefore photoions) when the optical pumping begins, and none if the cloud has been fully polarized. The number of photoion events that occur once the sample has been maximally polarized, in comparison with the size and shape of the initial spike of photoions, provides a very precise characterization of the cloud's final polarization [89].

Chapter 4

Calibrations and Data Selection

In a precision measurement, the bulk of the research is in determining the systematic uncertainties through self-consistent analysis and simulation. Each detector in this experiment is critical and has independent calibrations and cuts, which are described in detail in this chapter. Because this analysis was not blinded, there is an increased importance that the choice of cuts should be clearly justified. The primary goal of blinding was nevertheless achieved — to make sure all analysis is done completely with full redundancy of checks wherever possible — so the discipline entailed must be described in full detail.

4.1 Considerations for Data Collection

Although the detection chamber was designed to feature two MCP detectors on opposing sides of an applied electric field, and intended for simultaneous use, in practice the two detectors produced quite a bit of feedback during simultaneous online operation. As a result, the decision was made to bias only one MPC detector at a time; the detector in use was switched every few hours, collecting approximately the same amount of data with each detector. Thus, the runs are sorted into electron and recoil runs (sometimes eMCP and rMCP runs), depending on what the detector in use was intended to detect.

These two types of runs were used for very different purposes in terms of analysis. The electron runs were used directly to measure nuclear physics parameters A_β and b_{Fierz}. The recoil runs were used to measure cloud polarization, position, and size.

These parameters — particularly the polarization — must be well understood in order to effect the nuclear physics measurements performed with the other detector. The method of switching periodically which detector is in use assures that our knowledge of the atom cloud may be treated as concurrent to the electron run measurements.

The the evaluation of cloud position is discussed in Section 4.5. and the polarization measurement is discussed in Section 4.6, The recoil runs may also be analyzed in the future as part of a search for right-handed weak interactions (discussed further in Chapter 7.4).

4.2 An Overview of Available Data

In addition to dividing up the online data according to the active MCP detector, the data is further sorted into runsets based on when certain settings were adjusted, and the individual runsets are treated separately for nearly all parts of the analysis. The classification of runs is summarized in Tables 4.1 and 4.2.

One parameter that was varied is the overall strength of the electric field; data has been collected with the eMCP at electric field strengths of 66.7 V/cm and 150. V/cm, while rMCP data has been collected at 395. V/cm, 415. V/cm, and 535. V/cm. Note that these field strengths are all too low to significantly perturb any but the least energetic of the (positively charged) betas originating from decay, and those betas already lack the energy that would be needed to travel through the SiC mirror and Be foil vacuum seal into a beta detector.

Electron Runs

	OP Delay	Events	Electric Field	Runs
Runset EA	300 μs	0	66.67 V/cm	314, 362, 363, 383-386, 393.
Runset EB	300 μs	173,640	150.0 V/cm	428-437, 440-445.
Runset EC	700 μs	18,129	150.0 V/cm	476, 477.
Runset ED	400 μs	207,596	150.0 V/cm	478-489, 502-505, 510, 513.

Table 4.1: A list of 2014 online electron runs with potentially usable data. The "Events" column includes only the number of events that passed all cuts.

In considering Tables 4.1 and 4.2, we note that Runsets EA and RA were neglected completely during analysis after it was determined that one scintillator had an im-

Recoil Runs

	OP Delay	Electric Field	Runs
Runset RA	300 μs	395.0 V/cm	303, 308-313, 318, 326, 327, 328, 340, 342, 343, 376, 377, 378, 394, 395, 396, 398-402.
Runset RB	300 μs	535.0 V/cm	409-419, 421-426, 446, 447, 449.
Runset RC	700 μs	395.0 V/cm	450, 454, 455.
Runset RD	700 μs	415.0 V/cm	460-466, 473, 474.
Runset RE	400 μs	415.0 V/cm	491, 497, 498, 499, 509.

Table 4.2: A list of 2014 online recoil runs and associated parameters. A count of good events that pass all cuts is not included because different cuts must be used for polarization and trap position data.

properly set hardware threshold such that lower energy betas weren't being detected at all. Additionally, there was a QDC module failure before Run 450, resulting in an abrupt change in calibration for the two scintillators. The electric field is larger during recoil runs in an attempt to maximize the fraction of nuclear recoils collected, as well as the separation in TOF between different charge states. For electron runs, although not all SOEs were collected, the lower electric fields were preferred in order to decrease background events and the sparking incidents. Although the final analysis uses only the eMCP runs directly, the result could not have been obtained with the same degree of precision had the rMCP data not been present.

4.3 Preliminary Data Selection with the rMCP

As described in Chapter 3.6, the primary function of the rMCP within the context of this experiment is as a probe of the atom cloud, and it provided a critical check of the cloud's position, size, and polarization state over the course of the beamtime. The process of cleaning, calibrating, and analyzing this data is described here.

The two delay lines located just behind the rMCP provide information about hit position. The principle behind a delay line's operation is relatively straightforward. The delay line itself is made from a thin wire wound into a flattened coil that covers the area of the microchannel plate. The second delay line is oriented perpendicular to the first and immediately behind it, but also covers the full area of the microchannel plate. When a charged particle is incident on the stack of microchannel plates, an electron shower is initiated. The shower gains strength as it propagates through the MCPs' microchannels, and emerges on the back side of the stack after having been greatly amplified.

After emerging from the back of the MCP stack, the electron shower is then incident on a delay line, generating an electrical pulse that propagates from the hit point towards both ends of the wire. Although the wire is conductive, the propagation speed is finite, and this fact is key to extracting the hit position. The time of arrival for the electrical pulse is recorded at each end of the delay line wire, and it is the difference between the two times that tells where along the wire the original hit occurred. In general, a single delay line is only precise enough to determine the hit position as projected along the direction perpendicular to its coil's wires. The electron shower continues past the first delay line to hit the delay line immediately behind, which again creates an electrical pulse that propagates towards the ends of that wire, and a similar procedure can be used to evaluate the hit position in the perpendicular direction. Therefore, for an event in which the rMCP is hit and an electron shower is triggered, we expect to have five timestamps associated with that hit – one associated with the MCP stack itself, and two from each delay line.

This understanding of how delay lines work informs the initial stages of data processing for rMCP events. To obtain the cleanest possible rMCP data, the first step is to simply throw out every event which doesn't have a complete set of five timestamps associated with it – even though it would still be possible to make good use of many events which have only partial data. Even though many "real" rMCP hit events came in under threshold in one or more channels, detector noise was plentiful, and that noise varied in both quality and quantity over the course of the beamtime. Therefore, it was decided to be more important for the rMCP data to be as clean as possible, despite the fact that its statistical power would be reduced. (Note that this step is *not* done on the eMCP side – more on that in Section 4.10)

The next stage of rMCP data cleaning is to discard events with an aberrent set of timestamps. A delay line is essentially just a long wire, and the time it takes to propagate a signal from one end of the wire to the other is fixed. This means that no matter where along the delay line a pulse is generated, if one adds rather than subtracts the timestamps at which the pulse arrives at each of the two ends, that sum should be constant after accounting for the time of the original hit – which we can determine from the timestamp associated with the MCP. To that end, we construct delay line sums for the "x" and "z" delay lines,

$$\mathrm{DLA\_XSUM} = (\mathrm{TDC\_DL\_X1}) + (\mathrm{TDC\_DL\_X2}) - 2(\mathrm{TDC\_ION\_MCP}) \quad (4.1)$$
$$\mathrm{DLA\_ZSUM} = (\mathrm{TDC\_DL\_Z1}) + (\mathrm{TDC\_DL\_Z2}) - 2(\mathrm{TDC\_ION\_MCP}). \quad (4.2)$$

For a perfectly operating detector, one would expect for a collection of many measurements of DLA_XSUM and DLA_XSUM should each look like an isolated delta spike. In practice however, our distributions had a more complex set of features. The shapes, widths, and even positions of these distributions changed from run to run, and not all of these changes could be attributed to a known cause (e.g. a change in detector settings). Distributions from a single run are shown in Fig. 4.1.

Because the characteristics of these timing sum distributions varied from run to run, it didn't make sense to aggregate all the data before taking cuts, so any cuts had to be chosen on a run-by-run basis. Because of the asymmetry and occasional bimodality of the distributions, it also didn't make sense to try to fit the distributions to a function such as a gaussian and then cut away some number of sigma from the fit function. The algorithm that was used in the end was to determine the peak's maximum, then discard events from the portion of the distribution in which the distribution's height is less than 10% of the maximum. Fig. 4.2 shows the effect of these cuts on the measured cloud position within a single run.

4.4 Calibrations with the rMCP

A calibration mask was created for the rMCP, to eliminate any nonlinearities in the images produced. Several months before the ^{37}K beamtime was to occur, the mask was attached in front of the rMCP, and a test of the delay lines' ability to produce an image was performed using an alpha source to illuminate the full surface of the detector. The mask was later removed in advance of the beamtime, in order to preserve the highest possible surface area, and calibrations were performed using the older mask data and subsequently applied to the online ^{37}K data.

The calibration to the offline data with a visible mask was performed over a number of steps. The data was given a preliminary rough calibration, performed on each delay line separately, which simply involved taking the difference in pulse arrival

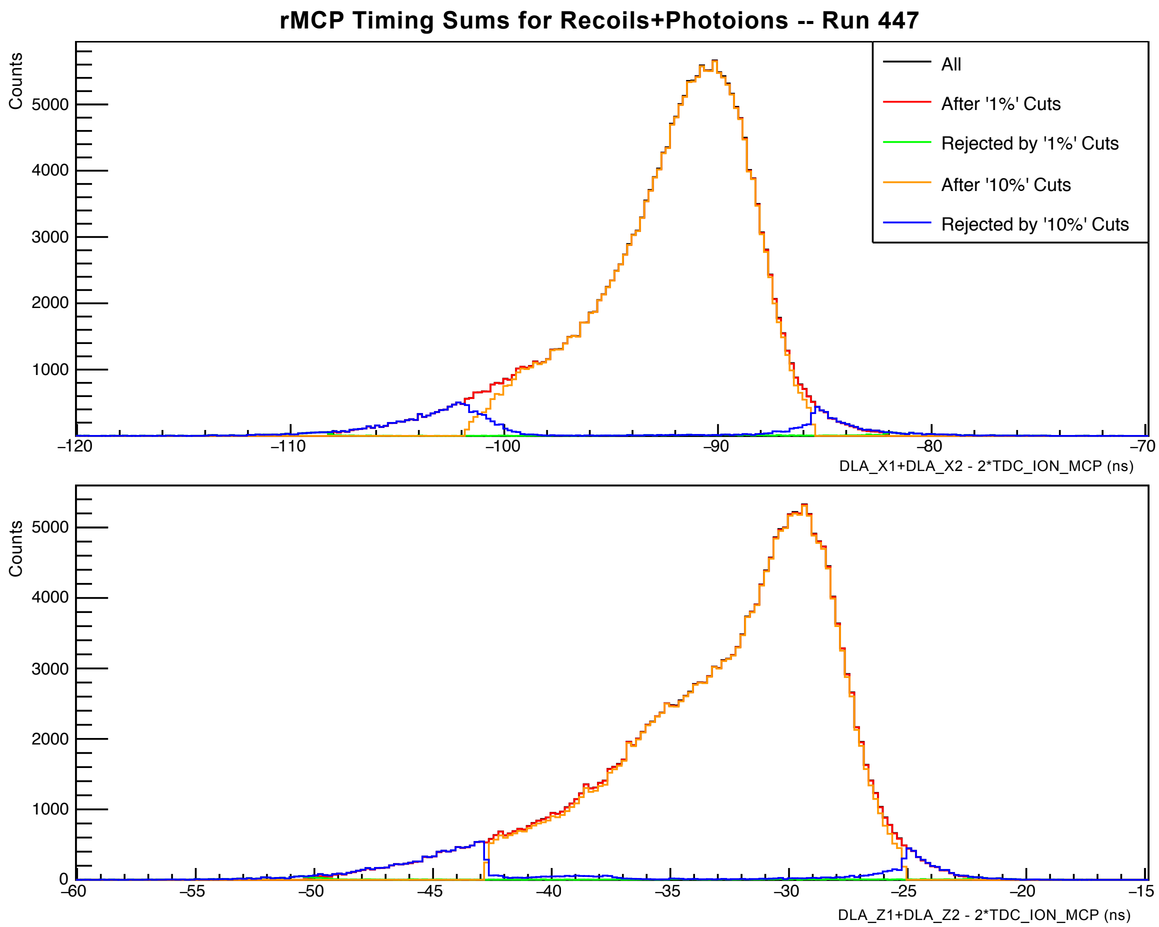

Figure 4.1: Timing sums and associated cuts for the rMCP detector, run 447. The '10%' cuts shown simply eliminate events in which the distribution's height at that value is less than '10%' of that distribution's maximum, and the '1%' cuts are performed in a similar manner. Note that this is *not* the equivalent of eliminating 10% (1%) of events. The above distributions each show the results within their own distribution after cuts are taken on the *other* distribution. Only a single run is shown here to avoid washing out features – because the characteristics of these spectra varied significantly over the course of the beamtime, and not all of the changes can be attributed to a change in settings.

times between each end of the delay line, scaling the result by a factor chosen to get the image to be the approximate correct size, and then subtracting an offset to center the image.

With the preliminary calibration providing a visible image to work with, the '10%' cuts as described in Section 4.3 were applied, significantly sharpening the visual mask

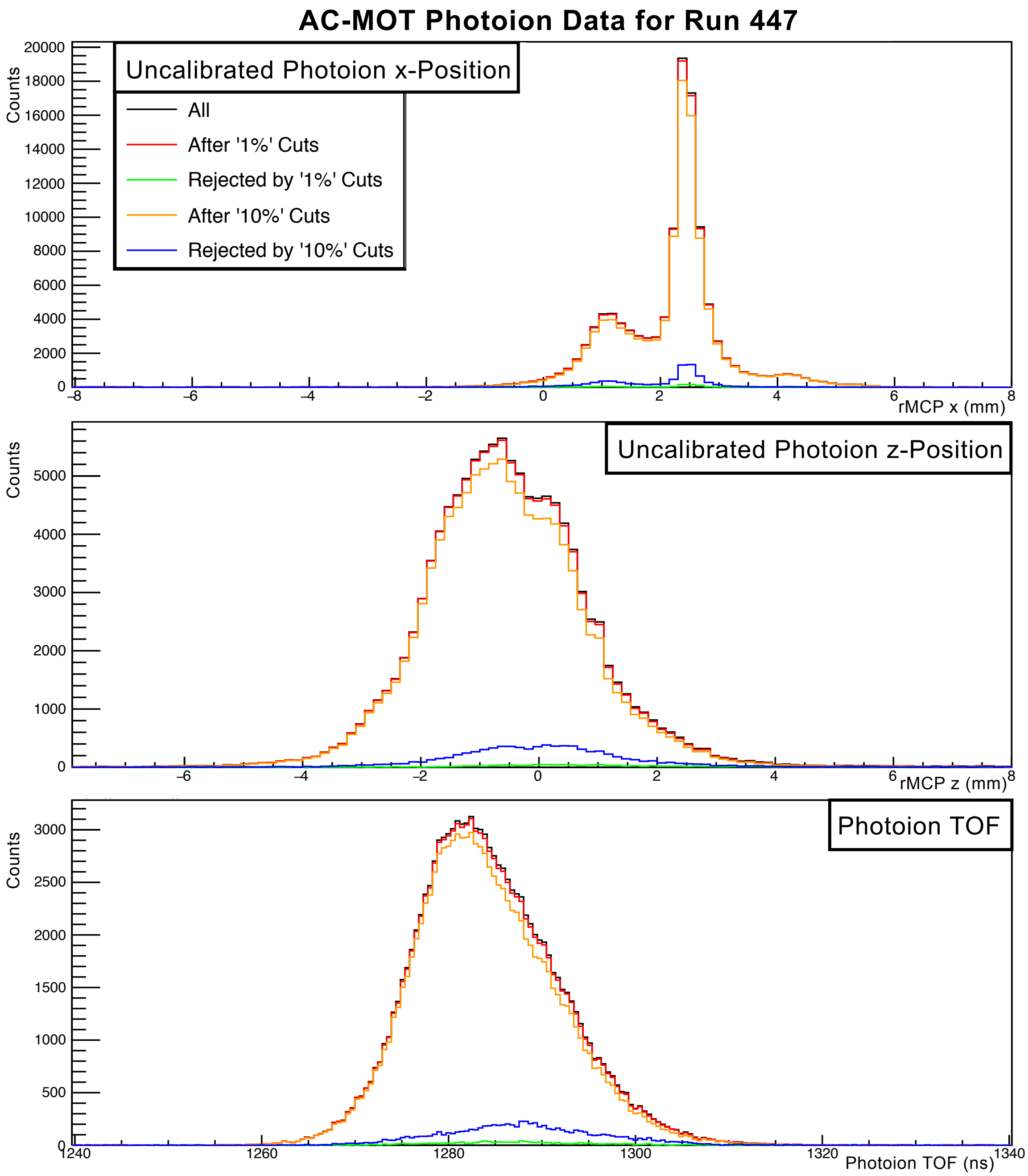

Figure 4.2: Cloud Position for run 447 for rMCP timing sum cuts as shown in Fig. 4.1.

lines and overall image border. Next, a small rotation was applied, followed by a more precise centering algorithm. Following this, a linear stretching algorithm was applied to adjust the height and width of each row and column individually, while aligning the grid lines to their known position on the detector. Finally, an additional radial stretch was applied to only the outer areas of the image. This last adjustment can be justified by noting that it's expected for the outer parts of the detector to produce a more distorted image, and that appeared to be the case here. See Fig. 4.3.

When the online rMCP data was eventually collected, it was found that the rMCP image appeared offset by several centimeters relative to the previous calibration, which necessarily affected the location of the timing sum peaks (similar to those shown in Fig. 4.1). The most likely cause for this is a change in cable lengths between the readout and data acquisition in the months between the calibration and online data collection, but it meant a new set of '10%' cuts needed to be established for the online data, and also cast some doubt on the validity of the established calibrations. In the end, these cuts were established on a run-by-run basis due to the varying shape of the timing sum peaks.

Our ability to confidently accurately apply the old offline calibration to the new online data depended on our ability to center the image correctly, as different parts of the image are stretched and squeezed differently. The appearance of the plate edge–the only remaining indicator of the quality of the centering or overall calibration–changed shape slightly from run to run. Despite this, images from the online data were all summed together after applying run-by-run cuts, and the resulting image was centered by eye.

The centering was performed iteratively, because the subsequent steps in the calibration will distort the image differently depending on how accurately it was centered beforehand. These subsequent steps in which the image is stretched and squished will also change the apparent centering of the overall image. Calibrated and uncalibrated images are shown in Fig. 4.3 for both offline and online data.

The lower plots in Fig. 4.3 show an unfortunate pattern of vertical stripes across the full surface of the rMCP. These stripes persisted over many (but not all) of the online runs. They can still be clearly seen in Fig. 4.4, which is a sum of all Runset RB's photoion events. The cause for these stripes could not be determined, and they could not be removed in post-processing analysis.

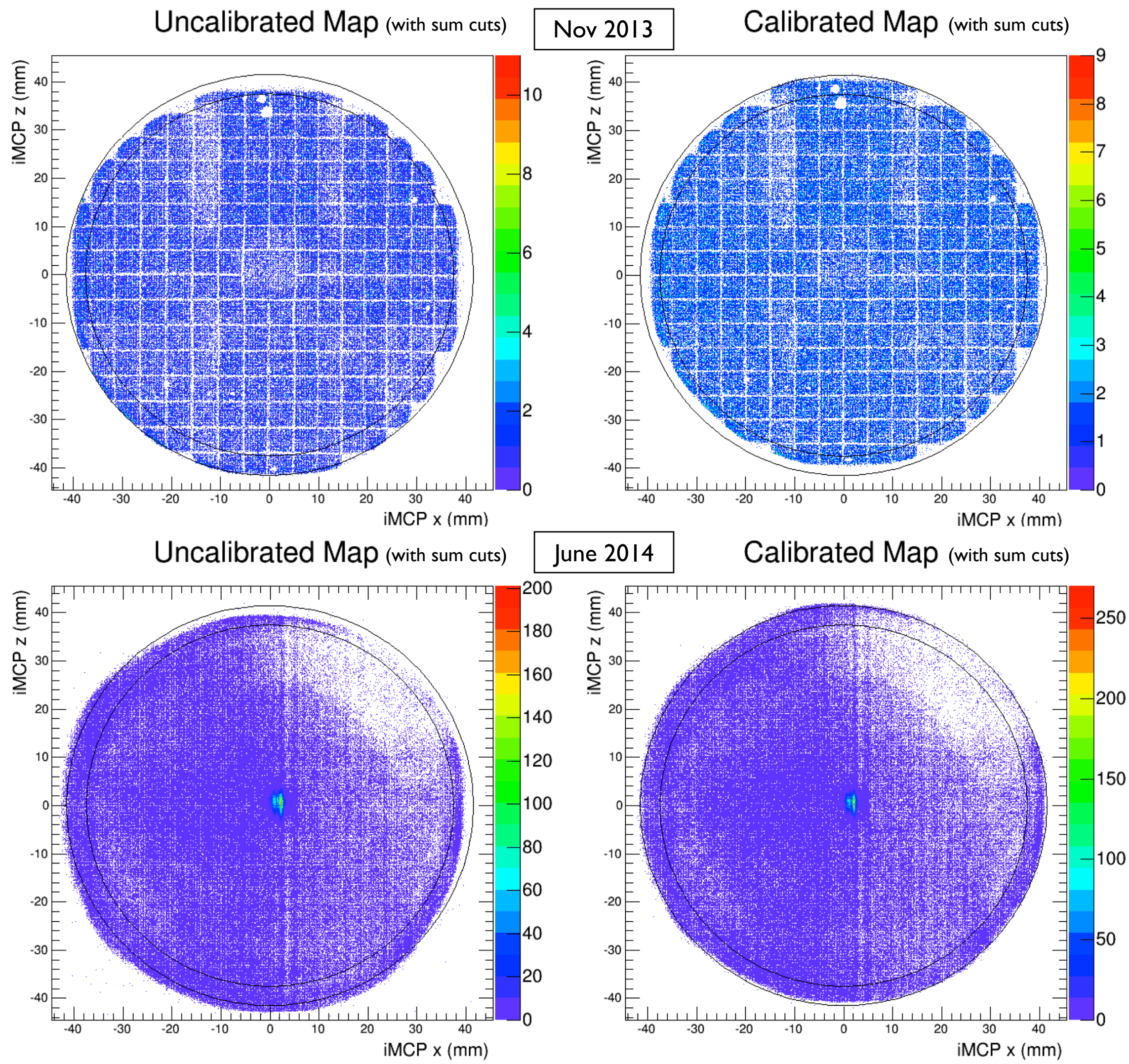

Figure 4.3: rMCP Calibration. The left images show the rMCP hit map with only a basic preliminary calibration; the images on the right are filled with the same hit data, but after the calibration has been performed. The upper two images are from data collected offline in advance of the 2014 beamtime using an alpha source; the shadow from a calibration mask is clearly visible. The lower images show rMCP data taken from a single online run, and includes both photoion and nuclear recoil data, collected over both the polarized and AC-MOT times. The photoion image of the atom cloud visible in the centre of the lower plots.

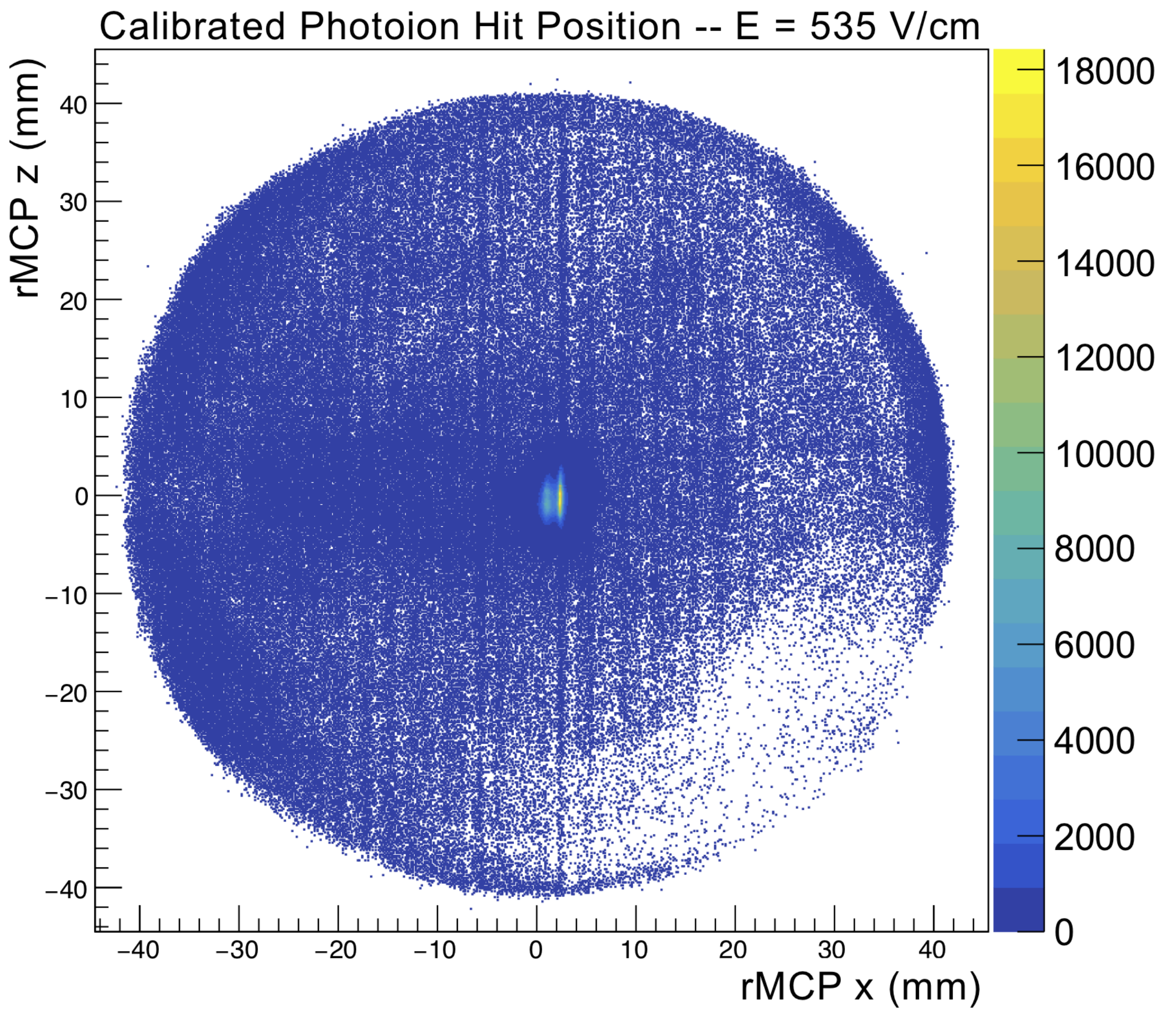

Figure 4.4: Photoion Hit Positions in 2D. This is the entirety of the good photoion data taken at 535 V/cm. The central bright spot is an image of the atom cloud arising from photoionization events of unpolarized atoms; the rest is background. Vertical stripes of indeterminate cause can be seen across the face of the image – it has not been possible to eliminate them in analysis.

4.5 Cloud Position Measurement

With the rMCP detector calibrated (Section 4.4), several types of data may be extracted. It is possible to extract the hit positions and times-of-flight for the incident nuclear recoils, and an analysis of such data could be used to perform a test of right-handed currents within the nuclear weak force, as discussed in Chapter 7.4. However, we will focus here on what may be learned about the *atom cloud* from rMCP events in coincidence with the photoionization laser.

This class of data (events with both an rMCP hit and a photoionization laser hit in coincidence) can be used to measure cloud polarization, and the methodology and results of that process as it applies to this particular experiment are discussed in a recent publication [89]. We are also interested in the cloud's position and size during the periods of time where decay data is collected, since this represents a potential systematic effect that must be accounted for within our models. The latter will be the primary focus of this section.

The first step in such a measurement is to try to eliminate as much background as possible. We have already required that every event considered here must include both an rMCP hit and a photoionization laser pulse. As we are interested in measurements of trap position, it makes sense to also require a *complete* set of position data recorded on the rMCP's delay lines. This is further trimmed by a '10% cut' on the timing sums, as described in Sec. 4.3. Any event including a scintillator hit is rejected, as these events have an increased likelihood for a recoiling ion to be detected on the rMCP instead of- or in addition to the photoion we expect (It is at this stage of the process that Fig. 4.4 is created.). Finally, some fairly loose cuts are applied about the central x- and z-positions, as well as the ion's time of flight (measured with respect to the arrival of a photoionization laser pulse).

With these basic cuts performed, the cloud position and size must be measured. We are particularly interested in measurements of the cloud during the time when it is considered to be *polarized* — however the great majority of photoionization events occur when the cloud is *not polarized* (see Fig. 4.5). This is because the photoionization laser acts only on excited atomic states, which are readily available during the operation of the MOT. When the MOT is shut off, the atoms quickly de-excite. At the start of optical pumping 300 μs later (in the case of the 535 V/cm data), there is a short burst of photoions due to the atoms being temporarily placed into an excited state as part of the optical pumping process. The photoion burst falls away rapidly as atoms are optically pumped into the stretched state and can no longer be excited by the optical pumping laser.

A projection of the cloud's position on the x- and z-axes, and its TOF (indicative of position along the y-axis) is plotted over the course of the repeating alternating current magneto-optical trap (AC-MOT)/optical pumping (OP) cycle in Fig. 4.5.

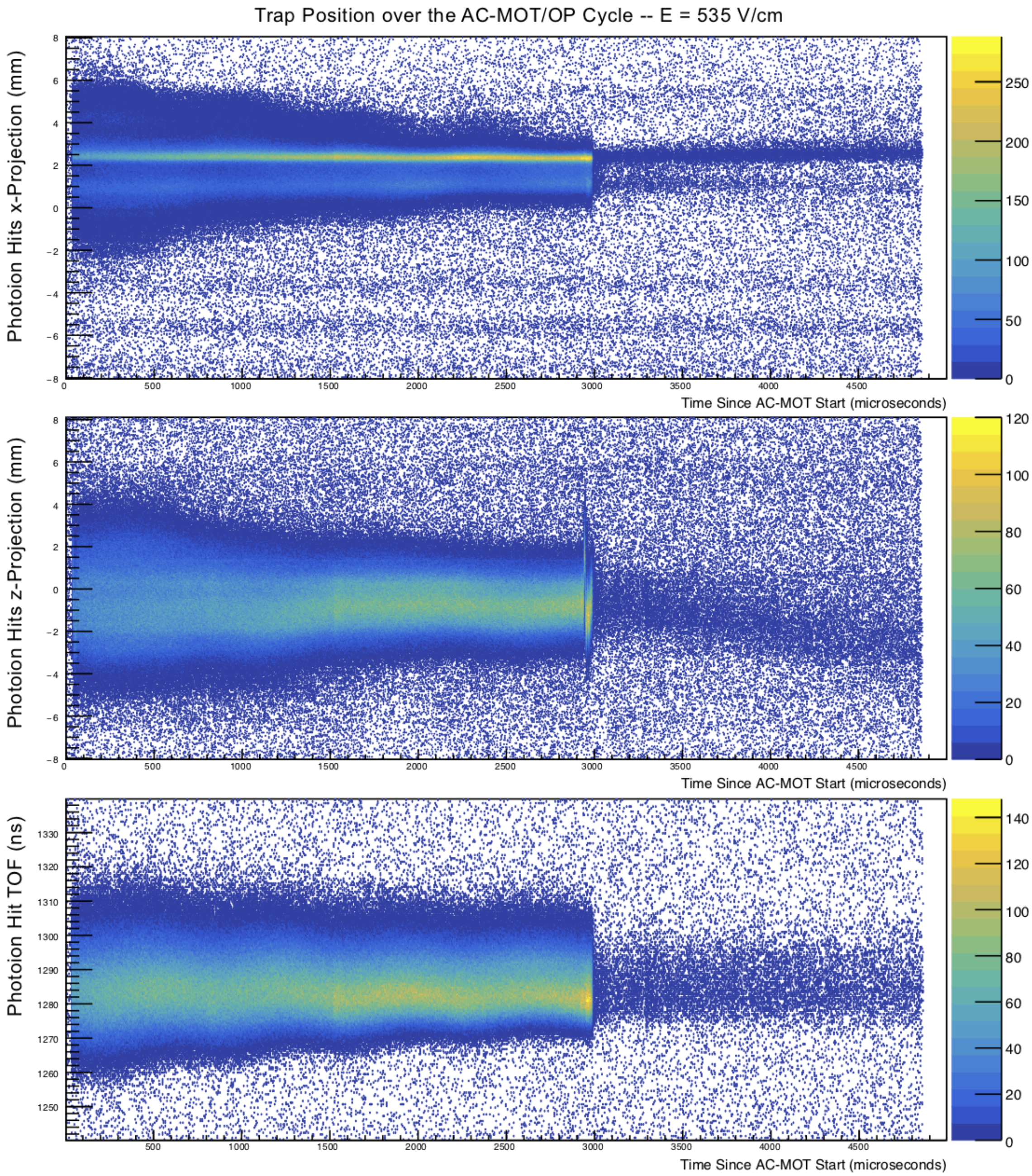

Figure 4.5: Projections of photoion hit positions and TOF at 535 V/cm, as a function of time since the start of the last AC-MOT cycle. The trap's periodic motion can be seen in sync with the AC-MOT's cycles, and it is clear that the cloud is also being compressed during this time, before being allowed to expand ballistically when the MOT is shut off. The photoion burst at the start of optical pumping 300 μs after the AC-MOT is shut off can be seen on the lower two plots.

The mysterious vertical stripes seen Fig. 4.4 are clearly evident in the top plot of Fig. 4.5, and their positions do not change over the AC-MOT cycle, even though cloud motion is clearly visible.

To extract the size and position of the atom cloud as projected onto all three axes, time slices of several hundred μs are taken from the beginning of the AC-MOT cycle, and from the part of the AC-MOT cycle immediately before the MOT is turned off. A gaussian is fitted to the cloud projection, with its parameters describing the trap's size and position during these parts of the cycle. A linear interpolation applied to describe the cloud's 3D size and position during polarized times, as functions of time since the AC-MOT cycle started. Results are shown in Table 4.3.

Runsets		Initial Position	Final Position	Initial Size	Final Size
EB $\leftarrow$ RB	x	1.77 $\pm$ 0.03	2.06 $\pm$ 0.08	0.601 $\pm$ 0.013	1.504 $\pm$ 0.047
	y	-3.51 $\pm$ 0.04	-3.33 $\pm$ 0.05	1.009 $\pm$ 0.013	1.551 $\pm$ 0.018
	z	-0.661 $\pm$ 0.005	-0.551 $\pm$ 0.021	0.891 $\pm$ 0.004	1.707 $\pm$ 0.015
EC $\leftarrow$ RD	x	2.22 $\pm$ 0.05	2.33 $\pm$ 0.11	1.18 $\pm$ 0.04	1.538 $\pm$ 0.087
	y	-3.68 $\pm$ 0.04	-3.31 $\pm$ 0.06	0.965 $\pm$ 0.012	1.460 $\pm$ 0.030
	z	-0.437 $\pm$ 0.09	-0.346 $\pm$ 0.037	0.927 $\pm$ 0.007	1.797 $\pm$ 0.026
ED $\leftarrow$ RE	x	2.274 $\pm$ 0.012	2.46 $\pm$ 0.06	0.386 $\pm$ 0.016	1.382 $\pm$ 0.046
	y	-4.54 $\pm$ 0.04	-4.28 $\pm$ 0.04	0.986 $\pm$ 0.08	1.502 $\pm$ 0.013
	z	-0.587 $\pm$ 0.04	-0.481 $\pm$ 0.018	0.969 $\pm$ 0.003	1.861 $\pm$ 0.013

Table 4.3: Cloud Positions and Sizes – Measured immediately before and immediately following the optical pumping phase of the trapping cycle. Measurements are evaluated using rMCP runs, and are taken to describe the cloud during associated eMCP runs as well. All entries are expressed in units of millimetres, and the size parameters describe the gaussian width.

4.6 Polarization Measurement

To measure the nuclear spin-polarization of the atom cloud, initial data selection was performed using a very similar set of cuts to those used for measurements of cloud position and size (Sec. 4.5). That is, using rMCP data, we require a photoionization laser pulse in coincidence with an rMCP hit including a complete set of position and timing information, and no coincident hit in either scintillator. These events are trimmed down by enforcing a cut on the delay lines' timing sums, and finally, the rMCP hit is required to have occurred within a particular TOF window (relative to the photoionization laser pulse), and within a particular window on the x- and z-axes.

Unlike the position measurement, the polarization measurement is only performed on events that fall within the nominal 'polarization' portion of the duty cycle, for obvious reasons. When the MOT's laser is shut off, the atoms rapidly de-excite and can no longer be photoionized. This period of time after the MOT laser is shut off and before the OP laser is turned on (300-700 μs, depending on the run) is used to measure the amount of background present, and also provides the opportunity for the AC-MOT's magnetic quadrupole field to die away and be replaced by the dipole-configuration magnetic field needed for optical pumping (see Ch. 2.3).

When the OP laser is turned on, there is a brief burst in the photoionization rate that rapidly dies away (faintly visible in Fig. 4.5). Because the photoionization laser is pulsed at a rate of 10 kHz, it frequently misses the initial part of the optical pumping process in which a large number of atoms are in the excited state and able to be photoionized ($\sim 20\,\mu$s or so). As a result, the signal must be integrated over a longer timescale in order for the optical pumping photoions to be clearly visible.

The fraction of the atoms in the excited state during optical pumping was modeled as a function of time by using the optical Bloch equations, and the result fit to the background-subtracted photoionization data. The polarization was evaluated separately for both of the polarization states in use, yielding a result of

$$|\vec{\boldsymbol{P}}_+| = 0.9913 \pm 0.0008 \tag{4.3}$$

$$|\vec{\boldsymbol{P}}_-| = 0.9912 \pm 0.0009, \tag{4.4}$$

consistent with the same polarization magnitude for both states, and precise to $< 0.1\%$. This result could only be attained after weeks of optimization using stable ^{41}K polarization data, with all optical pumping and magnetic field switching parameters kept constant. This result removes the polarization from serious consideration as a systematic for b_{Fierz}, and it is therefore left off the error budget of Table 7.1.

The analysis to extract the polarization was performed primarily by other members of the collaboration, and is discussed thoroughly within the collaboration's Ref. [89].

4.7 Electron Run Data Selection and Preliminary Cuts

Before proceeding further, several basic cuts are performed on the data. For the Electron Runs which are to be processed directly into a physical measurement, we consider only events in which there was a recorded hit *both* on the eMCP *and* on exactly one of the scintillators. The required scintillator hit, of course, is potentially a beta, and so it is obvious why this must be present. Events in which both scintillators record a hit are discarded, as they fall into two categories: an accidental coincidence, where we are seeing two different decays that, by chance, both occurred within the time window allocated to a single event (a few μs before and after the first recorded scintillator hit), a backscatter event in which a beta was incident on one scintillator before being scattered out into the opposite scintillator. Although it would be possible to process the former event type into usable information if we could be certain that it was truly an accidental coincidence, contamination from the latter event type would serve to increase the systematic uncertainty arising from beta scattering–already a dominant source of error.

The eMCP is used primarily to record incident shake-off electrons. As described in Section 2.1, every beta decay event will produce one or more SOEs. Most (but not all) SOEs originating from the atom cloud will be incident on the eMCP, however not all incident SOEs on the eMCP will produce a recorded hit. The electric field is such that SOEs originating elsewhere within the chamber may or may not be incident on the eMCP. Therefore, while imposing an eMCP hit requirement will eliminate some 'good' events originating from the cloud, it also eliminates a much larger fraction of background events originating from other surfaces within the chamber. This ability to 'tag' good events originating in the cloud is absolutely essential to any analysis involving angular correlations within this geometry.

In later sections, we will consider how to evaluate a further cut to be imposed on the time difference between scintillator and eMCP hits (Section 4.10), and some subtleties within analysis relating to this choice (Sections 5.4 and 5.5).

It is also necessary to remove from direct consideration any event which is coincident with a pulse from the photoionization laser. When photoionization occurs within the atom cloud, an orbital electron is removed from the atom and will be accelerated by the electric field into the eMCP, just as a shake-off electron from a decay would be. If, by chance, this photoelectron arrives in coincidence with a scintillator hit, it would be interpreted as a decay event from the trap – unless we preemtively discard it.

Over the course of the runtime, there were several instances where we noted an apparent electrical discharge within the experimental chamber, producing enormous backgrounds for a short time. The detectors typically recovered quickly afterward, so it was neither necessary nor useful to stop an entire run to wait for the system to recover. Instead, the time when the discharge occurred was recorded, and events within approximately one minute of the spark time were discarded.

We use only the "fully polarized" events for which we have a detailed understanding of the nuclear polarization (described in more detail in [89]). This means we must use *only* events from the "optical pumping" portion of the duty cycle (see Fig. 3.2), and discard events when the DC- or AC-MOT is active. After the AC-MOT is shut off, there is a short delay before optical pumping begins (see Tables 4.1 and 4.2) to allow the magnetic field to decay, and it is only after $100\,\mu s$ of optical pumping that we consider the atoms to be fully polarized. Furthermore, because the magnetic field from the DC-MOT is slow to decay (relative to the field from the AC-MOT), all events from the first five AC/OP cycles after every atom transfer are discarded. A further benefit of our insistence on considering only polarized data is that the scintillators' gains are more stable in the presence of only the (small, stable) magnetic field used for optical pumping than they are in the presence of a larger oscillating magnetic field used for trapping [96].

Finally, because this analysis depends heavily on energy measurements from the two scintillators as a proxy for beta energy, it is necessary to remove events in which the pulser LED fired. Although the pulser LED is useful for evaluating the stability of the scintillators, in the case where an LED pulse occurs together with a true beta hit in the scintillator, it may change the measured energy. Therefore, we discard all events that include an LED pulse.

4.8 Further Cuts Using the DSSD

The DSSDs are critical to our ability to veto background events in which the particle incident on the detector is a gamma ray rather than a beta — e.g., from annihilation radiation — however, they must be properly calibrated in order to be useful. The calibration was performed by other members of the collaboration, and the methodology is described in detail in [96]. It is summarized here for clarity.

Although it was not possible to use the DSSD in real-time analysis or event triggering, the DSSDs may be used, after the data has been collected, to distinguish between different types of particles incident on the detector, as more energy will be deposited by heavier particles. When a scintillator hit is triggered by a particle originating within the experimental chamber, that particle will typically have passed through the DSSD before arriving at the scintillator.

In the present experiment, the two primary particles that will concern us are β^+ particles originating from the decay of ^{37}K, and γ rays, which may be produced through a variety of processes, e.g. directly from the 2% decay branch, through annihilation of β^+ particles upon their interaction with regular-matter electrons, or bremsstrahlung radiation from emitted βs.

We would like to look specifically at events involving β^+ particles arriving direct from a decay within the atom cloud, and the DSSD may be used to eliminate events in which the scintillator is triggered by a γ. An incident β will typically deposit some portion of its energy in the DSSD as it passes through, however an incident γ will deposit significantly less energy; for this setup the energy deposited by a γ is generally indistinguishable from background on the DSSDs. Therefore, we require that a 'good' event must include a 'good' hit to the DSSD as well as a hit to the associated scintillator.

In order to proceed at this point, and because the DSSD readout records so much information, it is necessary to develop some criteria to determine whether or not we will accept any given DSSD readout as a β hit.

We read out the full waveform for every strip at each event with a scintillator hit, but in post-processing take *only* the 'time' and 'energy' from the waveform's peak. Each strip will have its own noise spectrum, energy calibration, and energy resolution. To classify an event as a good DSSD hit, we first require a good scintillator hit (as determined by the associated TDC readout) with energy above a nominal 10 keV to eliminate pedestal events, and no pulser LED.

We further require at least one 'x' strip and one 'y' strip within that same detector record an energy above the 'noise threshold', which is determined individually for each strip, and is defined according to the signal-to-noise (SNR) ratio. In other words, for each individual strip, the energy at which a certain fraction of events are 'real' events (as opposed to electronic noise) defines a particular 'noise threshold'. Values are tabulated for each strip at SNRs of 0.25, 0.5, 0.75, 1.0, and 2.0. As a default, the strip-by-strip SNR of 0.25 is used.

We require that the x strip and the y strip agree (to within some number of standard deviations — this is a parameter that can be varied) in amount of energy deposited, and in the time at which that hit occurred. In order to avoid problems resulting from the strips' non-uniform noise thresholds, we further require that the energy deposited be greater than some lower-end cutoff which is selected so as to be higher than every individual strip's noise threshold. In this case, the DSSDs' lower energy uniform threshold was set at 50 keV, a departure from the choice of 60 keV in an earlier analysis [63] [96].

We also elect to use only events where a beta hit the DSSD within a 15.5 mm radius of the center of the detector, as a large fraction of the DSSD hits at larger radii are from betas that have scattered from the collimator walls. Furthermore, events with more than *one* DSSD hit are rejected, as these events are likely either accidental coincidences of two beta decays, or else the result of betas scattering out of a scintillator before their energy can be fully absorbed.

4.9 Further Cuts Using the Scintillators

After all other cuts have been performed, a further cut is made on scintillator energy. It is important that this cut must be performed *after* event vetoes from more than one scintillator being hit are applied, and after the DSSD event vetoes have also been applied, in order to avoid unexpected behaviour in which we fail to reject certain classes of events that we had intended to reject.

For both scintillators, only events where the absorbed energy is between 400 and 4800 keV are accepted. The high energy cutoff is selected so far below the beta cutoff energy ($Q = 5.125\,\mathrm{MeV}$) because the low counting statistics at higher energies result in our observable, the superratio asymmetry, being poorly defined and poorly behaved. In later evaluating the systematic error associated with that cut, spectra with lower cutoffs ranging from 300 to 600 keV are considered, and spectra with upper energy cutoffs between 4600 and 5100 keV are considered separately.

4.10 Timing Improvements with the Leading Edge and Scintillator Walk Correction

The eMCP features a set of three delay lines, intended to be used to record the position of a hit. Though only two delay lines is sufficient to determine the position within the plane of the MCP if they are both hit, the presence of a third delay line allows for some redundancy. In practice, however, a large fraction of otherwise 'good' events include a hit on the eMCP, but have insufficient information recorded on the delay line channels to reconstruct a position.

Because a SOE from the trap is most likely to land in the centre of the plate, while *a priori* the background from other sources not expected to have any particular spatial distribution, it might make sense to accept only events where the eMCP hit is within some radius of the central peak. This methodology was seriously considered because the remaining data after this cut is taken has a much lower fraction of background events polluting it – however even for the most generous eMCP radius cuts, this results in a loss of about half of the events. The overall measurement is limited by statistics rather than systematics, so it was decided that no cuts on eMCP hit position would be taken in the final analysis.

Several years after the data was initially collected, a problem was discovered with our low-level analyzer software, which we had been using to convert large and unwieldy MIDAS data sets into somewhat smaller and more manageable ROOT data sets. In particular, for every timestamp recorded, our raw MIDAS data actually included both a timestamp for the leading edge (LE) of the pulse, and a timestamp for the trailing edge (TE). The analyzer had–for years–been reporting the timestamp associated with the trailing edge of the pulse. Initially it was unclear if there might have been a reason behind this choice, but a closer examination of the data showed that the LE data included less timing jitter and noise, as well as a sharper peak for timing pulses across the board (as in Fig. 4.6), with some channels showing a larger effect than others. This was corrected, and the entirety of this analysis has been performed now using the cleaner LE spectra.

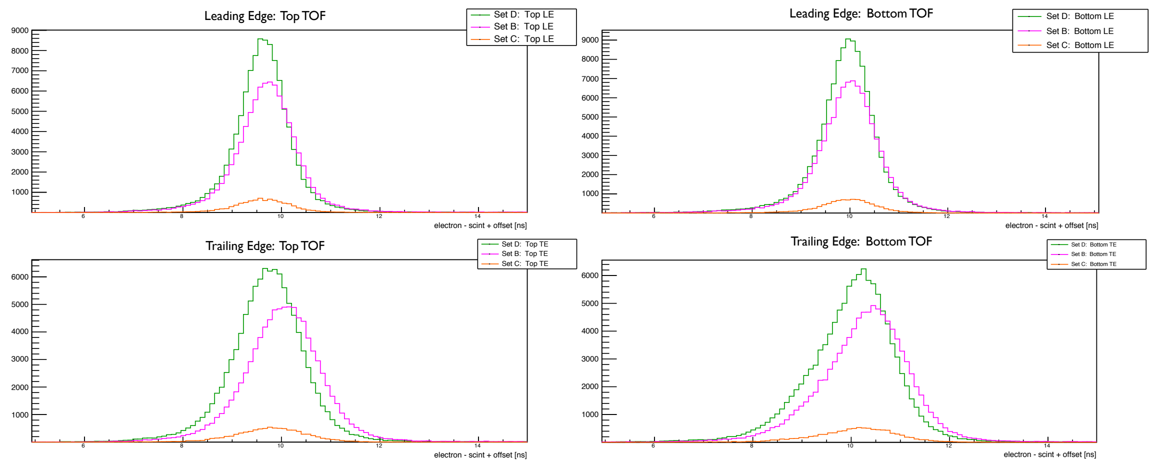

Figure 4.6: SOE TOF peaks (eMPC - Scintillator), using the leading edge (LE) and using the trailing edge (TE). Data is sorted according to runset. For each individual runset, the TE peak is broader than the LE peak. The centroid of each runset is also more variable in the TE plots.

The place where this change between the TE and LE timestamps had the biggest impact on the analysis is in the shake-off electron time-of-flight spectra, on which a cut must eventually be taken. Although this problem was not discovered in time to be used in the previous measurement of A_β using this same data [63], it likely would have had a negligible effect on the final result, because the SOE TOF cut that was used there was comparatively loose, and the evaluation of the background that remained was not a dominant systematic effect.

With the data reprocessed using the leading edge for timestamps, I wanted to eliminate as much background as possible from the SOE TOF spectrum. With this goal in mind, the next step was to correct the scintillator timing for its low energy ‘walk’ (see Fig. 4.7). A quartic polynomial was fit to each of the 2D timing vs energy spectra (the top and bottom detectors were treated separately), and the result was used to produce a ‘straightened’ SOE TOF spectrum with respect to measured scintillator energy, and as expected, the resulting SOE TOF spectrum was a bit more sharply peaked.

With the SOE TOF spectra cleaned up, a cut can be taken to reduce the fraction of background events. Informed by the model of background spectra described in

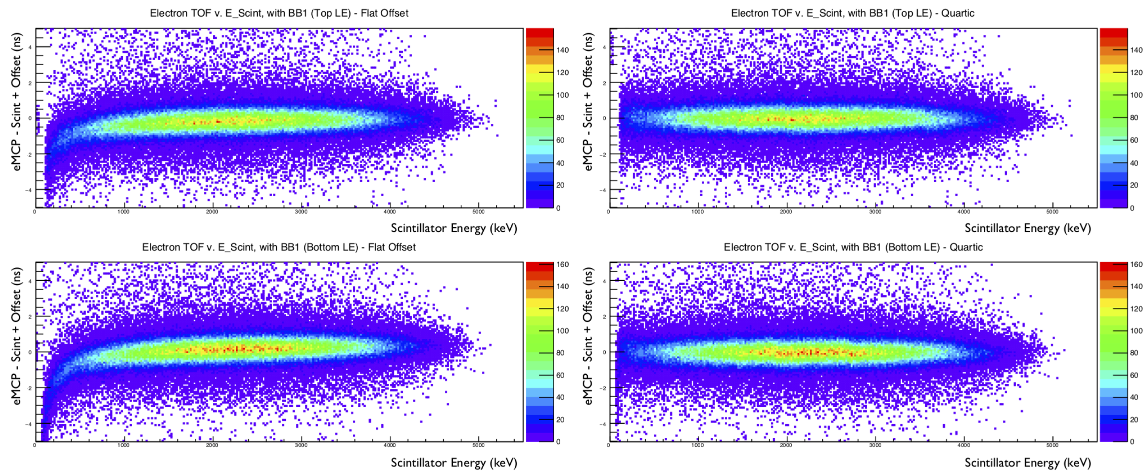

Figure 4.7: SOE TOF walk, measured with respect to scintillator hit time. The effect is actually occuring in the beta detectors, not in the eMPC, and is most likely the result of the constant fraction discriminator settings. Spectra from the top and bottom scintillators are shown before (left) and after (right) applying a quartic adjustment to straighten out the effective TOF.

Section 5.5, a cut was made to include only a 2.344 ns window around the primary peak in further analysis (see Fig. 5.11). With all cuts included, the four cleaned scintillator spectra corresponding to combinations of detector and polarization direction are plotted in Fig. 4.8.

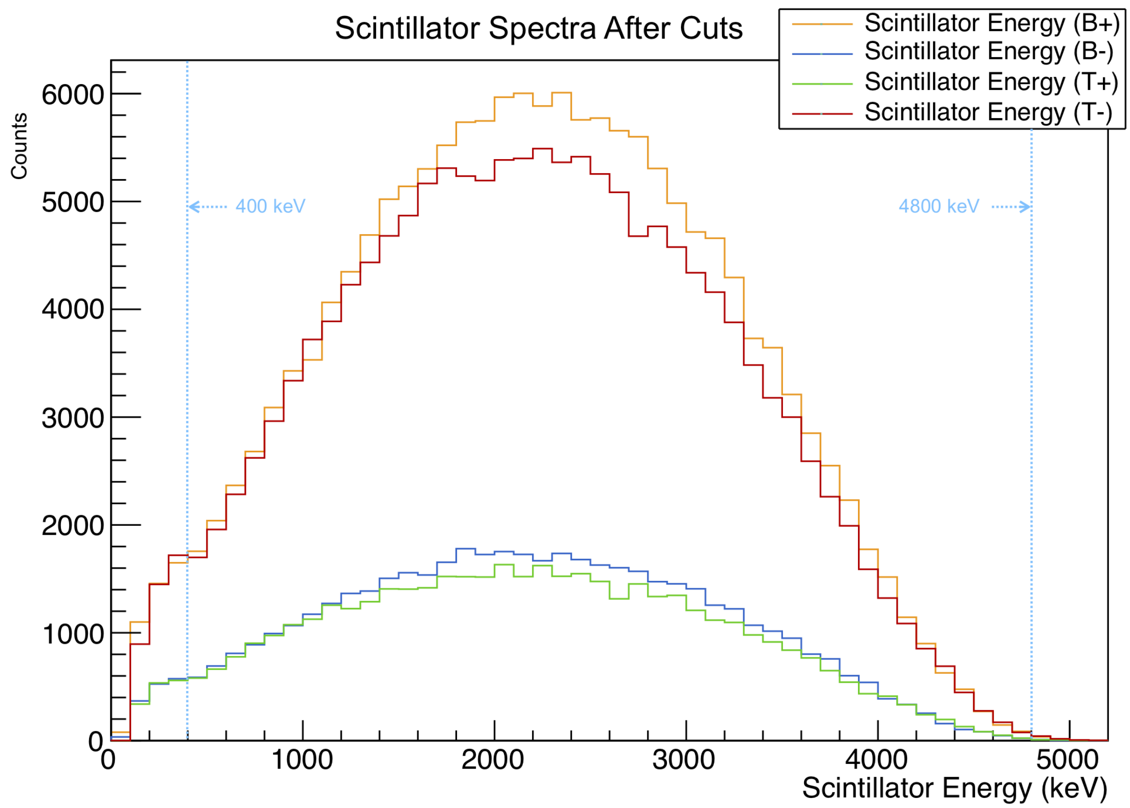

Figure 4.8: Experimental scintillator spectra, for both detectors in both polarization states. These spectra are what remain after all cuts have been taken, and all runsets are included. Binning is selected to match the convention used for the final analysis.

Chapter 5

Simulations

The TRINAT collaboration has created a Geant4 (G4) simulation which models the geometry and materials within the experimental chamber, and uses a monte carlo algorithm to describe generalized physical processes such as particle scattering and energy loss, within the geometry specific to the experiment. This software library has been maintained and updated over several generations of graduate students [96] [97].

5.1 Considerations for Software Upgrade Implementation

Prior to the simulations required for this particular experiment, two different sets of changes to the G4 code were needed – the first to enable multithreading, and the second to introduce certain BSM interactions to the decay distribution.

Enabling multithreading allows for a single instance of the Geant4 simulation to run on several processors at once, effectively speeding up the overall simulation by a factor of the number of processors used. In the years since the simulation was originally created, the Geant4 collaboration had created libraries intended specifically to support multithread usage, and since the running G4 simulations had historically been very time consuming for the TRINAT collaboration, the decision was made to implement multithreading within our own monte carlo software, on the hopes that this would enable faster progress in analysis.

Enabling multithreading support turned out to be quite time consuming, and in the end it might have been faster to have spent those months running simulations one processor at a time. Perhaps the improvement will prove valuable for use in future TRINAT experiments.

The TRINAT G4 monte carlo package had never been used to directly model interactions beyond the standard model within the decay physics. It had previously been set up by the collaboration to use a PDF including most of the terms from Holstein's Eq. (51) [61], which describes both electron and neutrino momenta from polarized beta decay. This treatment is quite robust, and includes corrections at recoil-order, as well as certain other corrections of similar size.

Unfortunately, terms arising from interactions beyond the standard model are not included in Holstein's description of the decay process. To understand the kinematic results of the exotic interactions of interest to us here, we turn to the classic JTW treatment of beta decay [1] [2]. In addition to the (expected) vector and axial interactions, JTW also describes the interaction in terms of (exotic) scalar and tensor interactions, should such be present. Despite JTW's broad ability to describe beta decay under a variety of physical models, this treatment includes only the leading-order terms, and smaller terms, such as recoil-order corrections, are neglected entirely.

Because the present project is a precision measurement of the Fierz interference, a term which arises from scalar and tensor couplings, it was imperative to create an event generator for our G4 simulations that could account for these exotic interactions while also including in its PDF the higher-order effects which, in some cases, can mimic the effects of a scalar or tensor current.

In light of the above, a new event generator was created, based on Holstein's Eq. (52), in which neutrino momentum has been integrated over and is therefore no longer an explicit part of the PDF [61]. As one might guess, Holstein's Eq. (52) is greatly simplified in comparison to Holstein's Eq. (51). A similar integration over all possible neutrino momenta can also be performed on the JTW PDF, causing several terms to vanish. The result in both the Holstein and JTW cases is a PDF over only beta energy and direction as measured with respect to nuclear polarization, and the two expressions can be combined in a straightforward manner by comparing similar terms. The details are provided in Appendix C.

It is this combined Holstein+JTW expression that forms the basis of the new G4 event generator. It must be noted that although the largest effect from any scalar or tensor interactions present would likely be (barring an accidental cancellation of two exotic terms) in a non-zero value of b_{Fierz}, these interactions can also introduce a perturbation to A_β at a higher order. In order for any precision experimental measurement of b_{Fierz} to be generalized to limits on the parameter space of scalar and tensor currents, it is important to incorporate an accurate representation of the results of such exotic interactions on *all* available observables, and the new G4 event generator does this.

5.2 Simulations for the Ninety-eight Percent Branch and the Two Percent Branch

With the new event generator, our G4 simulations are able to generate ^{37}K decay events mediated by Weak interactions with arbitrarily sized scalar and tensor couplings. For simplicity of analysis, and because scalar and tensor couplings produce similar effects on parameters A_β and b_{Fierz}, the decision was made to vary only the scaling of one particular set of BSM coupling constants within the Geant4 simulations. In particular, high-statistics simulations were performed using scalar coupling values,

$$g_S := \frac{1}{\sqrt{2}}(C_S + C_S') \quad = \quad \{0,\, \pm 0.1\}, \tag{5.1}$$

a combination that describes left-handed scalar interactions. These sets of parameters produce values of b_{Fierz}, and perturbations to values of A_β, given by:

$$b_{\text{Fierz}} \quad \approx \quad \{0,\, \mp 0.148661\} \tag{5.2}$$

$$\Delta A_\beta \quad \approx \quad \{0,\, -0.004259\}, \tag{5.3}$$

where we note that the change to the value of A_β is small relative to b_{Fierz}, and always has the same (negative) sign no matter the sign of b_{Fierz}, because while b_{Fierz} scales linearly with g_T, the perturbation to A_β arises from a quadratic term.

In addition to simulations of the dominant decay branch, it is also necessary to create simulations with sufficient statistics of the subleading ('two percent") branch. Because it is responsible only for a small fraction of the overall spectrum, we do not include corrections from BSM parameters in these simulations. These simulations are performed separately from the main branch simulations, and are evaluated using the older Geant4 event generator based on Holstein's Eq.(51) [61]. Simulated events from both branches are combined together in the appropriate ratio before further processing is performed.

5.3 The Simple Monte Carlo and Response Function

Scattering (both forward scattering and backscattering) is an important effect to consider within this experiment, and it must be evaluated through extensive and time consuming monte carlo simulations – in this case, using Geant4. However, there are a number of other systematic uncertainties that must also be evaluated, and it is computationally prohibitive (even after multithreading support was implemented) to evaluate all of them via the same sort of high statistics, scattering included, full monte carlo that we use for scattering effects. Luckily, the systematic effects arising from scattering are largely decoupled from other effects, and this section describes the framework that has been implemented in order to evaluate certain other systematic effects separately.

To this end, a fast-running Simple Monte Carlo (SMC) was developed together with an empirical "response function" similar to the one described by Clifford et al [98] to describe probabilistic beta energy loss before its detection in a scintillator. In the end, the lineshape description became quite involved, and it is unclear whether, in the end, any time was saved this way.

The purpose of the SMC was to *quickly* generate initial particle kinematics probabilistically for beta decay events, and it uses the very same event generator based on Holstein's Eq. (52) [61] that was developed for use with the more sophisticated Geant4 simulations. However, unlike in a G4 simulation, the SMC makes no attempt to track particles through the chamber, and instead simply calculates detector hits based on initial particle momentum. This procedure obviously neglects scattering effects, which can (in differing regimes) both *increase* and *decrease* the number of beta particles incident on a detector. Furthermore, this procedure also neglects any energy absorption in materials through which the beta passes before hitting a scintillator – and the beta *must* pass through several such materials (see Fig. 3.4).

To make the best use of the SMC for evaluating systematic errors, the energy lost before a beta hits a scintillator must be accounted for somehow in order to ensure all relevant physical effects are propagated through. In particular, before hitting a scintillator, a beta must pass through a 275 μm thick silicon carbide mirror, a 229 μm thick beryllium foil, and finally a set of 300 μm thick double-sided silicon strip detectors (DSSDs), before finally having its remaining energy absorbed within a scintillator. Although the DSSDs are themselves detectors with the ability to record the amount of energy deposited by an incident particle, there are some known problems in achieving a uniform level of precision across the full surface of the DSSDs, so adding the DSSD energy back to the scintillator energy to produce a better estimate of the original beta energy has the potential to create some problems for the analysis. Furthermore, given the presence of the mirror, an object with a similar thickness and scattering properties to the DSSDs, re-adding the energy lost in the DSSDs would not eliminate the need to estimate probabilistic energy loss in similar materials.

In order to create a quantitative description of the effective response function, which varies with initial beta kinetic energy (E_{in} below), an analytic function of 14 parameters has been created to model scintillator output for decays from the central cloud for each of the two polarization states in use. Although the form of the model is always the same, the 14 individual parameters will take different values for each of the four detector and polarization combinations. The full response function model, which describes the fraction of events measured at scintillator energy E_{out}, is given by the expression,

$$R(E_{\text{out}} \,|\, E_{\text{in}}, \text{Detector}, \text{Polarization}) = p_{\text{norm}} \left(f_{\text{moyal}} + f_1 + f_2 + f_3 + f_4 + f_5 \right) + f_{511}, \tag{5.4}$$

where p_{norm} is a single parameter, and the other terms within the expression are themselves functions of multiple parameters and are given by,

$$f_{\text{moyal}} = (1 - p_{\text{gfrac}}) \left(1 + \frac{-p_\alpha - p_\beta}{|E_{\text{in}}|} - \frac{p_\Delta}{p_\gamma \, p_W} - p_\gamma \, p_W \right) \times \left(\frac{e^{\left(\frac{E_{\text{out}} - \left(E_{\text{in}} - \frac{1}{2} p_{\text{dE0}} \right)}{2 \, p_{\text{lres}} \left| E_{\text{in}} - \frac{1}{2} p_{\text{dE0}} \right|} \right)} e^{\left(-\frac{1}{2} e^{\left(\frac{E_{\text{out}} - \left(E_{\text{in}} - \frac{1}{2} p_{\text{dE0}} \right)}{p_{\text{lres}} \left| E_{\text{in}} - \frac{1}{2} p_{\text{dE0}} \right|} \right)} \right)}}{\sqrt{2\pi \, p_{\text{lres}} \left| E_{\text{in}} - \frac{1}{2} p_{\text{dE0}} \right|}} \right), \tag{5.5}$$

$$f_1 = p_{\text{gfrac}} \left(1 + \frac{-p_\alpha - p_\beta}{|E_{\text{in}}|} - \frac{p_\Delta}{p_\gamma \, p_W} - p_\gamma \, p_W \right) \left(\frac{e^{\left(-\frac{\left(E_{\text{out}} - \left(E_{\text{in}} + \frac{1}{2} p_{\text{dE0}} \right) \right)^2}{2 \, p_{\text{toeres}} \left| E_{\text{in}} + \frac{1}{2} p_{\text{dE0}} \right|} \right)}}{\sqrt{2\pi \, p_{\text{toeres}} \left| E_{\text{in}} + \frac{1}{2} p_{\text{dEin}} \right|}} \right), \tag{5.6}$$

$$f_2 = \frac{p_\alpha}{|E_{\text{in}}|} \left(\frac{1 - \text{Erf} \left[\frac{(E_{\text{out}} - |E_{\text{in}}|)}{\sqrt{2 \, p_{\text{toeres}} |E_{\text{in}}|}} \right]}{2 \, |E_{\text{in}}|} \right), \tag{5.7}$$

$$f_3 = \frac{p_\beta}{|E_{\text{in}}|} \left(\frac{e^{\frac{p_{\text{k}} * (E_{\text{out}} - E_{\text{in}})}{|E_{\text{in}}|}} * e^{\frac{p_{\text{toeres}} \, p_{\text{k}}^2}{2 |E_{\text{in}}|}}}{2(1 - e^{-p_{\text{k}}})} \right) \left(1 - \text{Erf} \left[\frac{(E_{\text{out}} - E_{\text{in}} + p_{\text{toeres}} \, p_{\text{k}})}{\sqrt{2 \, p_{\text{toeres}} \, |E_{\text{in}}|}} \right] \right), \tag{5.8}$$

$$f_4 = \frac{p_\gamma}{2} \left(\text{Erf} \left[\frac{E_{\text{out}} - E_{\text{in}}}{\sqrt{(2 \, p_{\text{toeres}} \, |E_{\text{in}}|)}} \right] - \text{Erf} \left[\frac{E_{\text{out}} - E_{\text{in}} - p_W}{\sqrt{2 \, p_{\text{toeres}} \, |E_{\text{in}} + p_W|}} \right] \right), \tag{5.9}$$

$$f_5 = \frac{p_\Delta}{2\,p_\gamma\,p_W^3}\Bigg[(E_{\text{out}}-E_{\text{in}})\left(\text{Erf}\left[\frac{(E_{\text{out}}-E_{\text{in}})}{\sqrt{2\,p_{\text{toeres}}\,|E_{\text{in}}|}}\right]-2\,\text{Erf}\left[\frac{(E_{\text{out}}-E_{\text{in}}-p_W)}{\sqrt{2\,p_{\text{toeres}}\,|E_{\text{in}}+p_W|}}\right]\right.$$
$$\left.+\text{Erf}\left[\frac{(E_{\text{out}}-E_{\text{in}}-2p_W)}{\sqrt{2\,p_{\text{toeres}}\,|E_{\text{in}}+2p_W|}}\right]\right)+(2\,p_W)\left(\text{Erf}\left[\frac{(E_{\text{out}}-E_{\text{in}}-p_W)}{\sqrt{2\,p_{\text{toeres}}\,|E_{\text{in}}+p_W|}}\right]\right.$$
$$\left.-\text{Erf}\left[\frac{(E_{\text{out}}-E_{\text{in}}-2p_W)}{\sqrt{2\,p_{\text{toeres}}\,|E_{\text{in}}+2p_W|}}\right]\right)+(2\,p_{\text{toeres}}\,|E_{\text{in}}|)\left(\left(\frac{e^{\left(\frac{-(E_{\text{out}}-E_{\text{in}})^2}{(4\,p_{\text{toeres}}|E_{\text{in}}|)}\right)}}{\sqrt{2\pi\,p_{\text{toeres}}\,|E_{\text{in}}|}}\right)\right.$$
$$\left.\left.+\left(\frac{-2e^{\left(\frac{-(E_{\text{out}}-E_{\text{in}}-p_W)^2}{(4\,p_{\text{toeres}}\,|E_{\text{in}}+p_W|)}\right)}}{(\sqrt{2\pi\,p_{\text{toeres}}\,|E_{\text{in}}+p_W|})}\right)+\left(\frac{e^{\left(\frac{-(E_{\text{out}}-E_{\text{in}}-2p_W)^2}{(4\,p_{\text{toeres}}\,|E_{\text{in}}+2\,p_W|)}\right)}}{\sqrt{2\pi\,p_{\text{toeres}}\,|E_{\text{in}}+2\,p_W|}}\right)\right)\right)\Bigg], \tag{5.10}$$

and

$$f_{511} = |p_{\text{scale}}|\left[\frac{195}{17}\sqrt{\frac{2}{\pi}}\,e^{\left(\frac{-(E_{\text{in}}-308)^2}{578}\right)}+\left(40+\frac{(E_{\text{in}}-210)^2}{900}\right)\left(1-\text{Erf}\left[\frac{E_{\text{in}}-334}{30}\right]\right)\right.$$
$$\left.+\left(\frac{(E_{\text{in}}-505)^2}{1440}\right)\left(1-\text{Erf}\left[\frac{E_{\text{in}}-505}{30}\right]\right)\left(1+\text{Erf}\left[\frac{E_{\text{in}}-334}{30}\right]\right)\right], \tag{5.11}$$

where a p with any subscript is taken to be a variable parameter that must be evaluated. The expressions f_1, f_2, f_3, f_4, and f_5 are motivated by or taken directly from expressions of the same name within Clifford's description, and the individual parameters p_α, p_β, p_γ, p_Δ, p_W, and p_k are closely related to their counterparts of similar name [98]. The expressions f_{moyal} and f_{511} represent a departure from the published treatment, however, and arise from physical behaviours within this experiment which are not described within Clifford's treatment.

In particular, f_{511} is a rather inelegant representation of the annihilation radiation compton edge within our geometry. Although the DSSD provides an effective veto for the overwhelming majority of these events–and indeed within Clifford's treatment this veto is treated as being perfect in its discernment–it is clear both from experimental spectra and the Geant4 simulations intended to represent them that there exist a small number of such events within our scintillator spectra that cannot be vetoed in this manner. These events must be understood and adequately accounted for.

It should be noted that no attempt is made to derive the expression for f_{511} from first principles; the expression was chosen only because of its visual similarity to the spectrum's fit residuals before its inclusion. This expression's contribution to the overall function is negligible at all but the lowest initial beta energies (Eq. 5.11's p_{scale} parameter, showing the absolute normalization of f_{511}, is plotted in the top right of Fig. 5.7.), and is always negligible at scintillator energies above $\sim 500\,\text{keV}$, as can be seen in Fig. 5.5. We note that within the final analysis, all scintillator spectra will be given a low energy cutoff at 400 keV, so the only the higher energy tail of f_{511} will make any contribution.

The expression f_{moyal} arises from the beta particles' energy loss within materials (i.e. the mirror, the beryllium foil, and the DSSD itself, as in Fig. 3.5) before its eventual absorption within the scintillator. Although Clifford's treatment does include a ΔE detector (our DSSD would be the equivalent), the energy absorbed in this detector is added back in to the total before Clifford's final spectra are modeled. Although it would be possible to do something similar with our DSSD spectra, we would still be left with the problem of accounting for the similarly-shaped energy loss within the mirror and foil.

The distribution for energy deposition within a thin material by an energetic charged particle, first described by Lev Landau in 1944 [99], is now known as a Landau distribution. This distribution has a variety of properties that make it challenging to work with – notably its mean, variance, and all higher moments are undefined, and the distribution itself cannot be written in closed form. Its primary redeeming mathematical feature, however, is the fact that the convolution of a Landau distribution with another Landau distribution is, itself, a Landau distribution, and this means that we can represent the sum total of energy absorption within three successive thin materials as a single Landau distribution.

Within the present context, an expression for energy absorption that can be evaluated and re-evaluated quickly by computer with adjusted parameters is needed, as this must be used within a fit function. To this end, we employ a so-called 'Moyal function', which was developed in 1955 to be used as a closed form approximation to the Landau distribution [100]. Indeed, Eq. 5.5 is little more than a Moyal function.

The values of these parameters are allowed to vary with initial beta energy, and must be determined empirically by a series of fits to simulated spectra. To effect this result, the TRINAT Geant4 simulation is used to generate a series of 'mono-energetic' spectra. That is, for each energy value under consideration (with discrete values selected to span the energy range of betas in our decay), events are generated in which every outgoing beta initially has the same amount of kinetic energy, and the angular distribution of these betas is physically appropriate for the polarization and beta energy under consideration. These mono-energetic betas are propagated through the experimental geometry via Geant4, and the resulting scintillator spectra are recorded. Each polarization state must be considered separately, but spectra for both detectors are generated simultaneously, as it is necessary to generate events into a full 4π steradians in order to fully account for betas scattered into- or away from the detectors. Cuts identical to those imposed on the experimental data are applied (see Chapter 4). Several such spectra are shown for the Bottom Detector in the '-' polarization state, with their best fit response functions, components thereof, and residuals of the fit, in Figs. 5.1, 5.2, 5.3, 5.4, and 5.5.

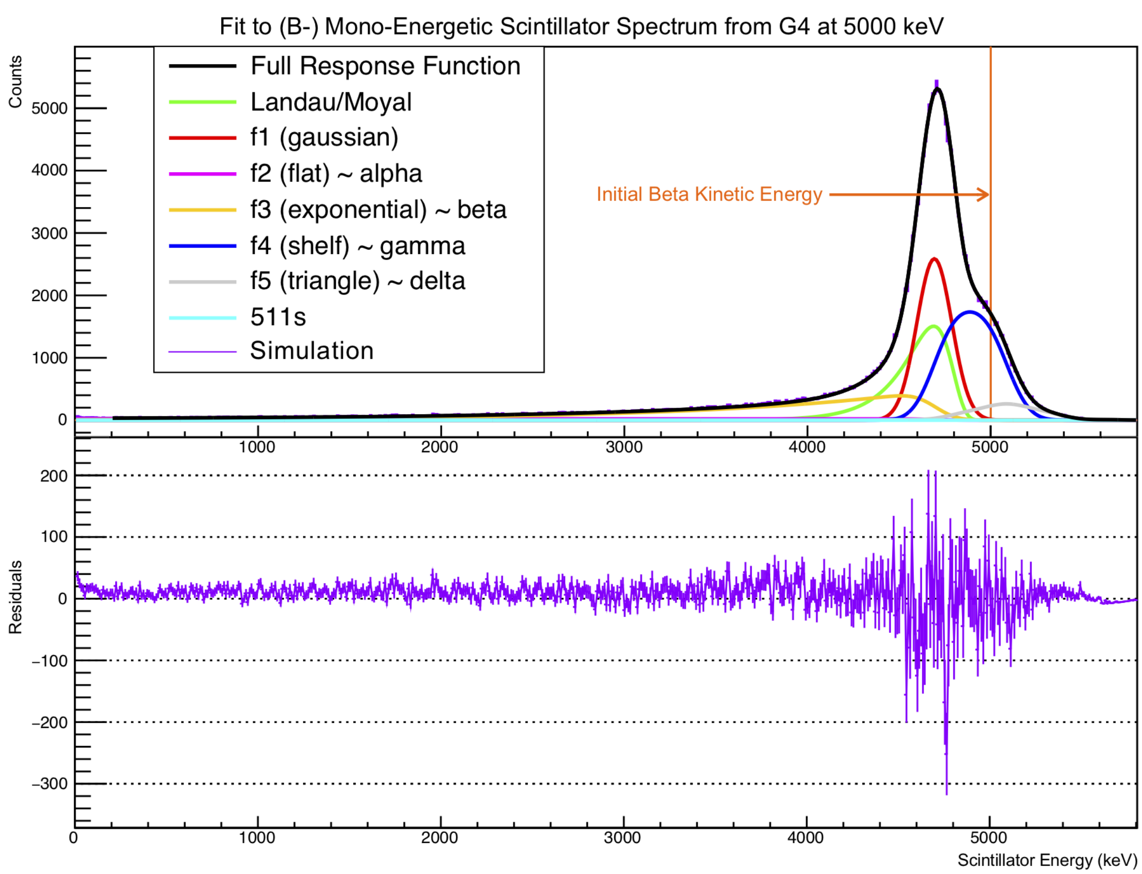

Figure 5.1: Fit to Mono-Energetic Spectrum, 5000 keV (B-)

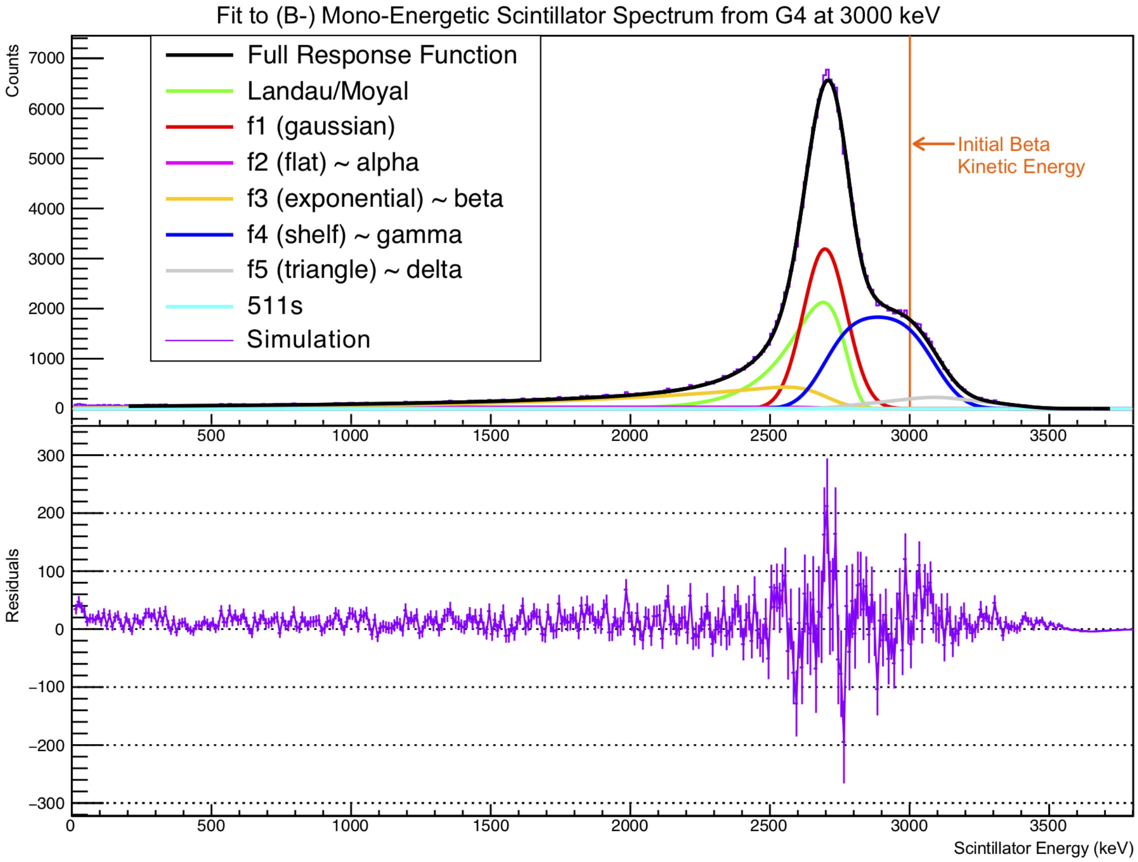

Figure 5.2: Fit to Mono-Energetic Spectrum, 3000 keV (B-)

The values of the individual parameters contributing to the fit functions in, eg, Figs. 5.1, 5.2, 5.3, 5.4, and 5.5 are allowed to vary with initial beta energy, and the energy dependence of each parameter must be modeled in order to extrapolate the shape of the response function to intermediate initial beta kinetic energy values that are not explicitly modeled. For each parameter, the energy dependence is modeled by an analytic function selected to have similar characteristics. Each of these analytic functions is itself a function of several parameters which can be adjusted to optimize its fit to the true best-fit energy dependence of the parameter it models. Because some parameters are only weakly independent, it is necessary to perform these fits iteratively on only a single parameter at a time, revisiting earlier parameter fits after fixing other parameters to updated models. The results of this process are shown in Figs. 5.6, 5.7, and 5.8.

It is useful to consider how well this empirical response function works to model the

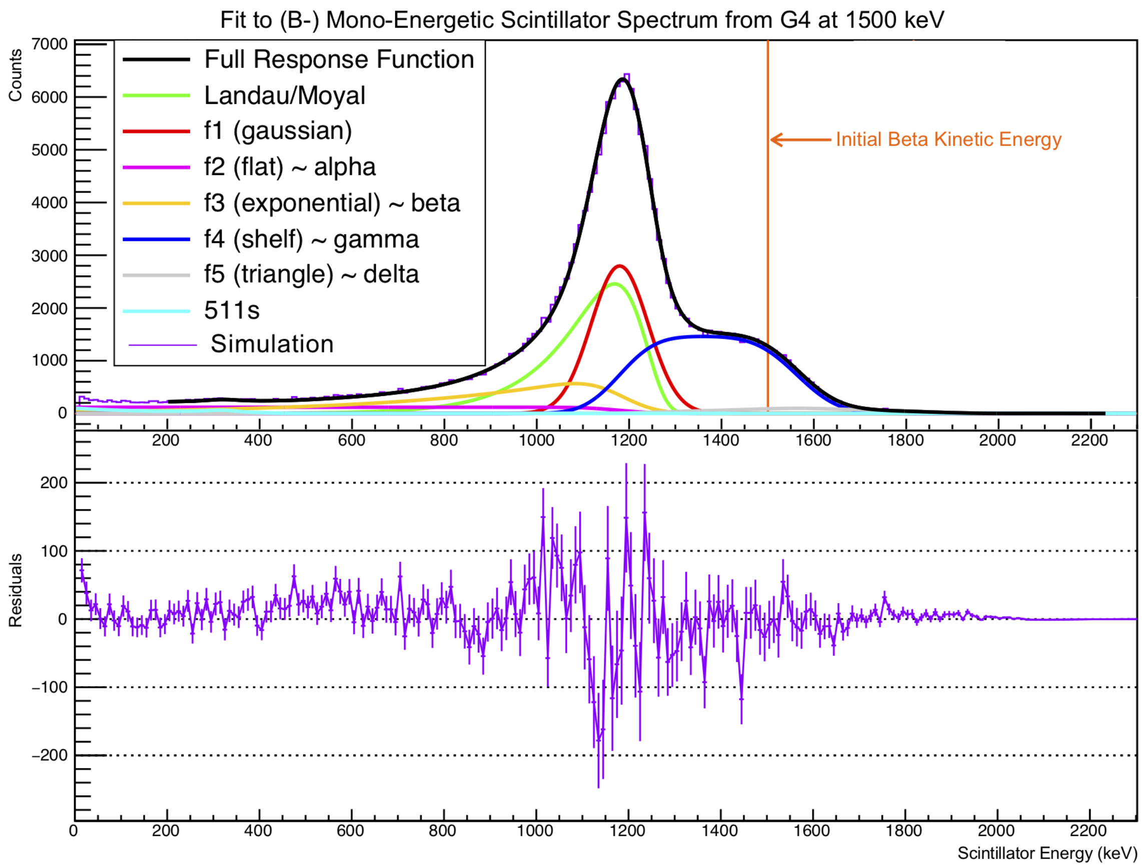

Figure 5.3: Fit to Mono-Energetic Spectrum, 1500 keV (B-)

spectra. One can see clearly from Figs. 5.1, 5.2, 5.3, 5.4, and 5.5 that the fit residuals appear noticeably *worse* at lower initial beta energies. Fig. 5.9 shows the reduced χ^2 values arising from comparing mono-energetic G4 spectra to the empirical response functions described above, for all four detector and polarization combinations.

With the energy dependence for each of the response function's parameters carefully modeled, it becomes possible to make proper use of the full response function. Given a decay event with a known beta energy from a nucleus with its initial polarization known, we can now predict a probabilistic response from *both* scintillator detectors. Obviously, for a single decay event, the full spectrum cannot be realized – however in aggregate the modeled response function agrees well with results from the full Geant4 simulation, particularly at higher beta energies.

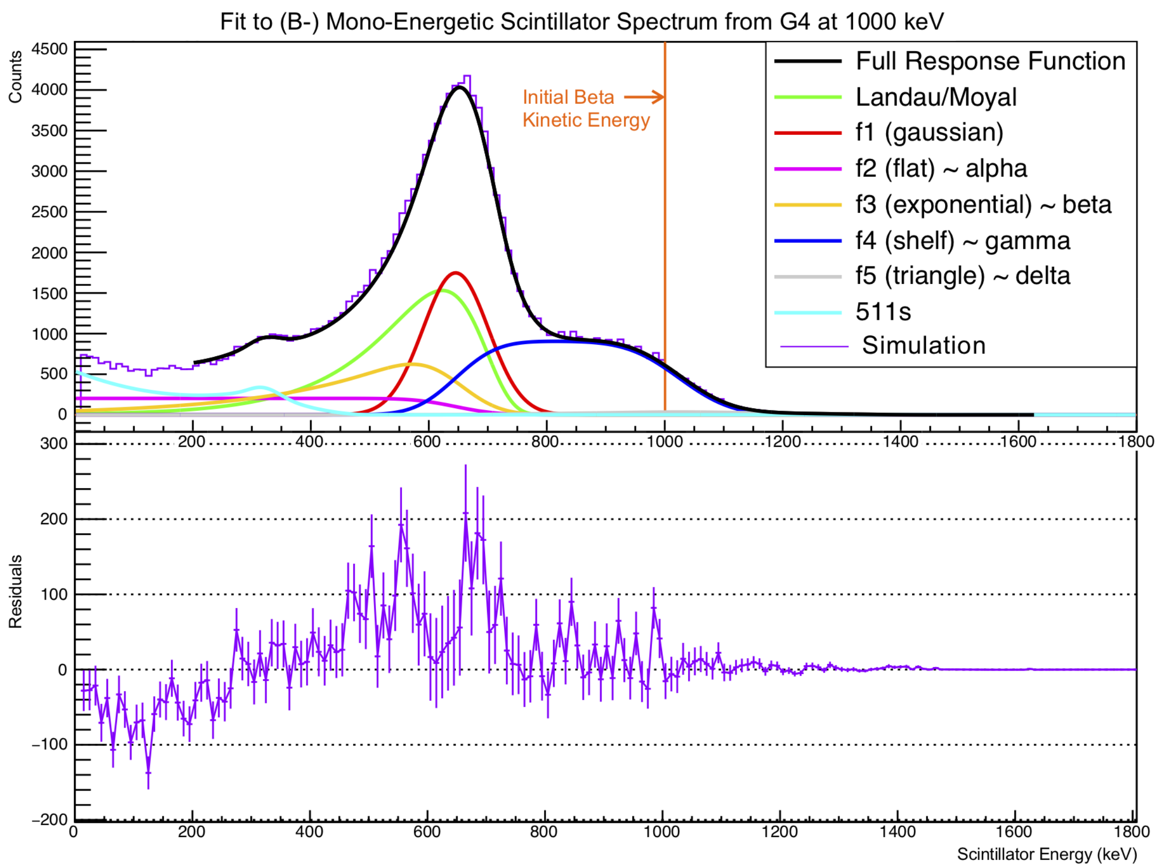

Figure 5.4: Fit to Mono-Energetic Spectrum, 1000 keV (B-)

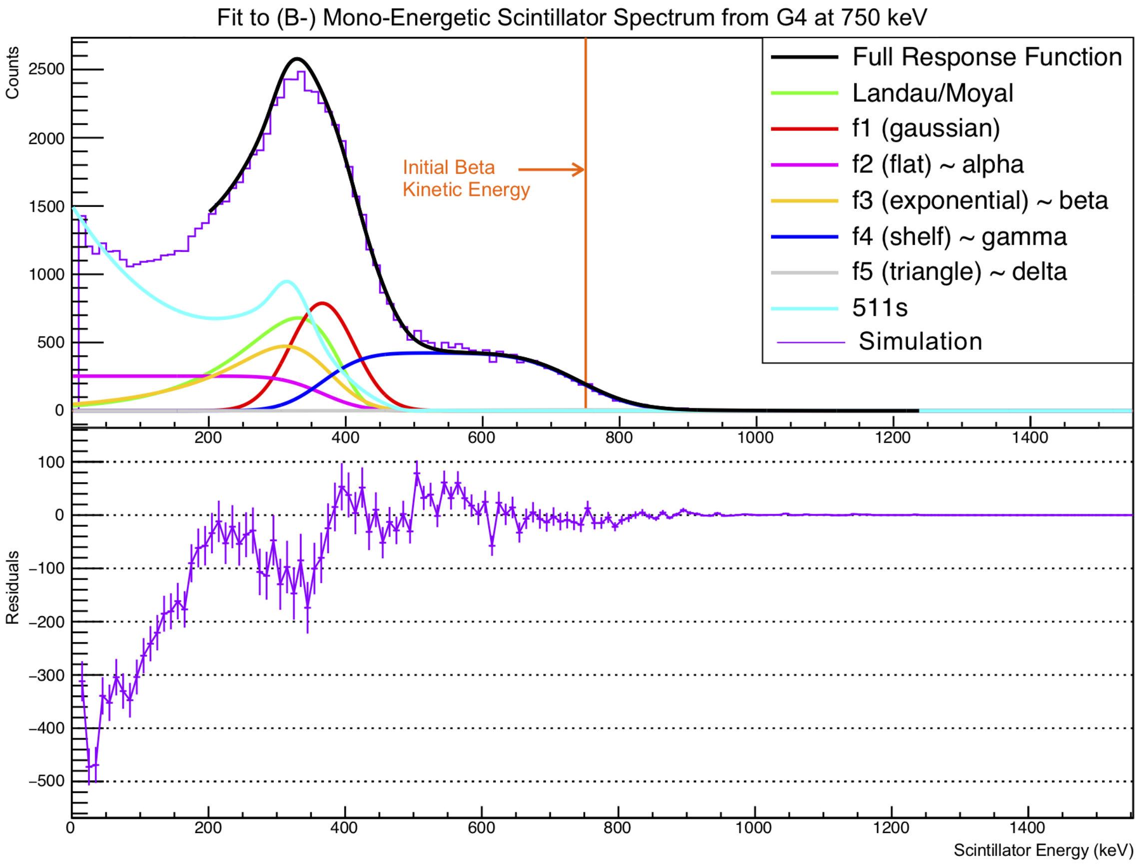

Figure 5.5: Fit to Mono-Energetic Spectrum, 750 keV (B-)

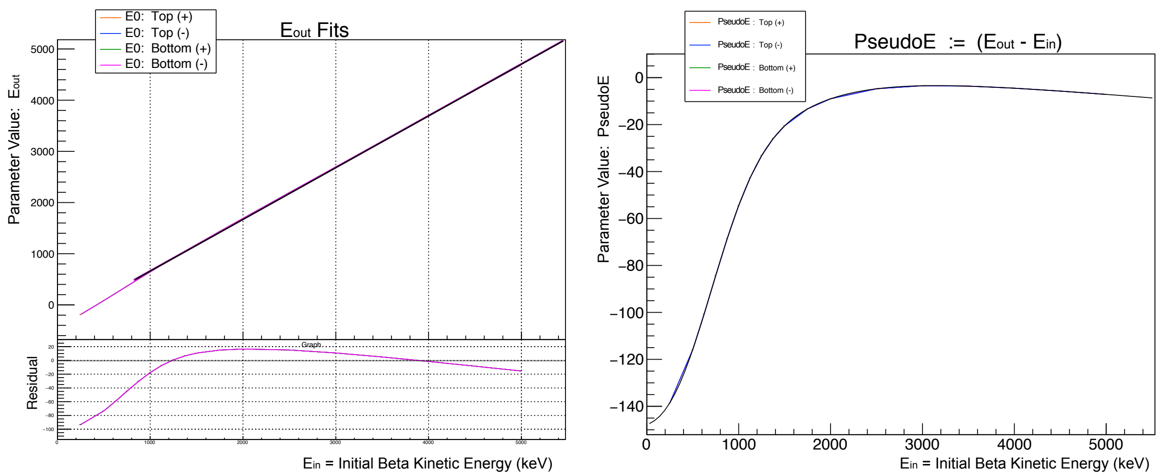

Figure 5.6: Lineshape Parameter Fits (Part 1) – Several parameters for the response function are shown varying smoothly with initial beta energy, after iterative fits comparing mono-energetic spectra from the simple monte carlo + response function to the equivalent mono-energetic Geant4 simulation. These fit outputs are subsequently fit with other functions in order to enforce a smooth variation with energy, and the results of this second fit are shown here and in Figs. (5.7) and (5.8). Above, two plots are shown dedicated to describing the *most probable* difference between initial beta kinetic energy and measured scintillator energy. The left plot shows the results and residuals from a fit to a straight line; the right plot shows what remains (and fits it to an analytic function) after the dominant linear dependence is subtracted away.

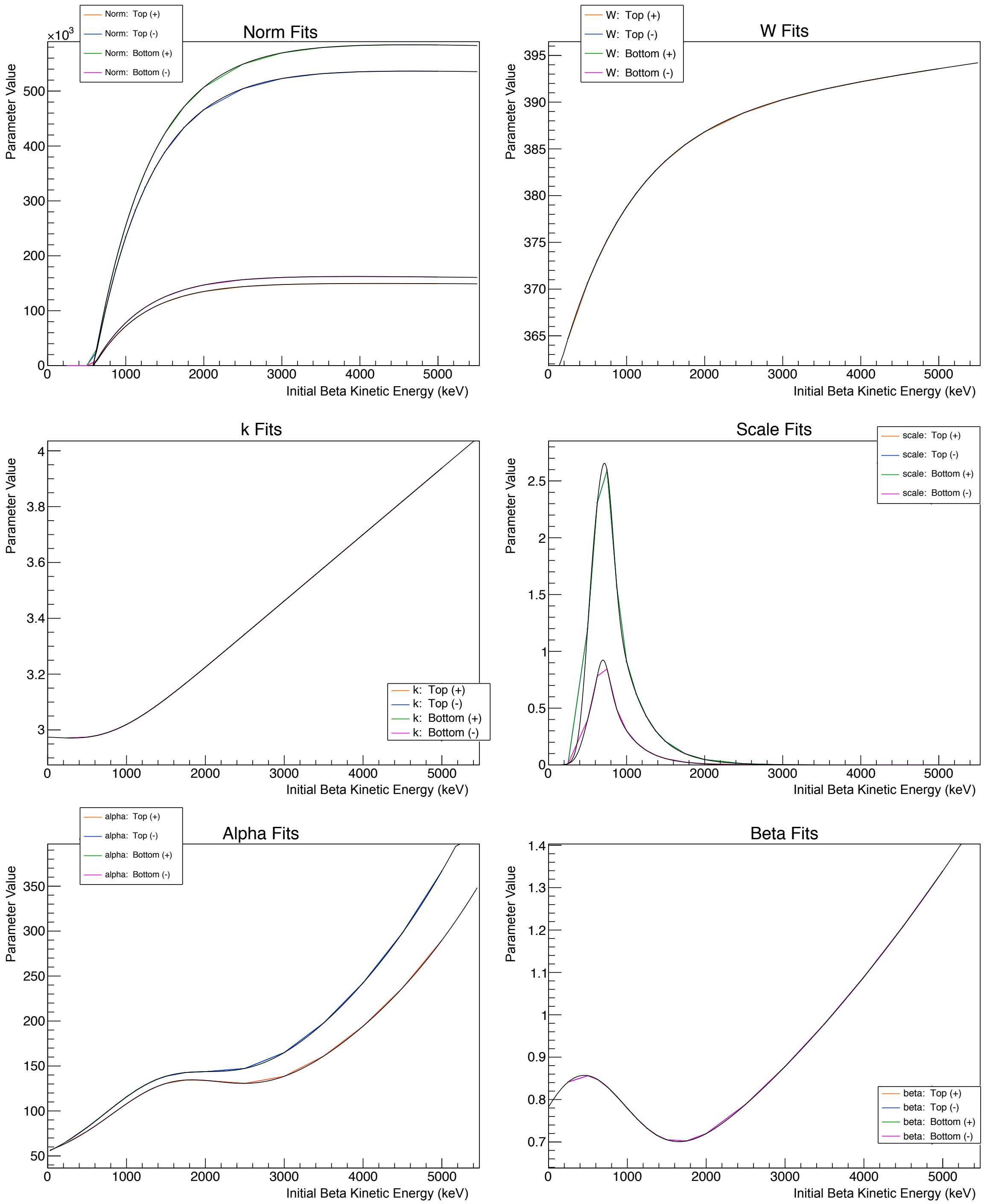

Figure 5.7: Lineshape Parameter Fits (Part 2)

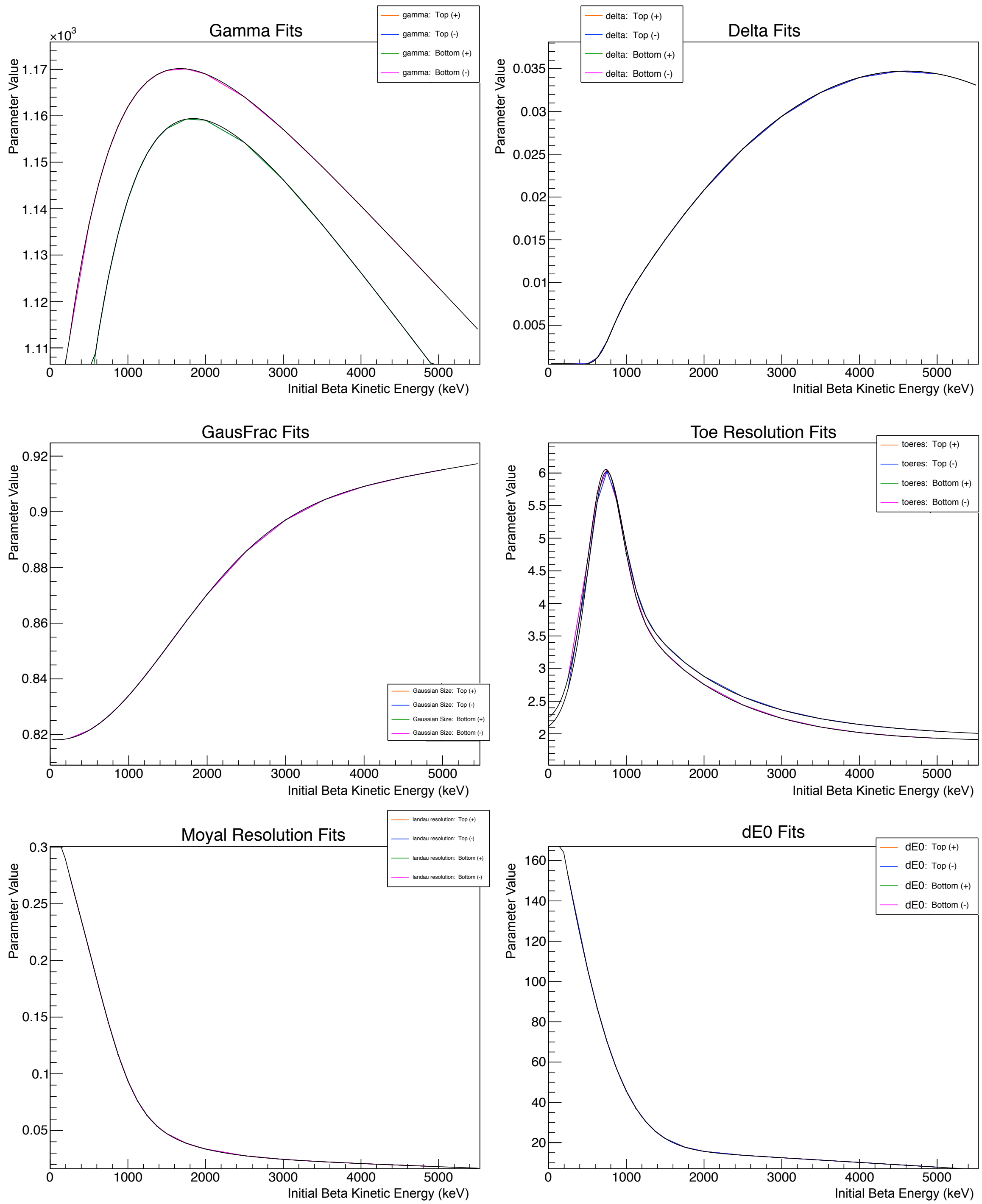

Figure 5.8: Lineshape Parameter Fits (Part 3)

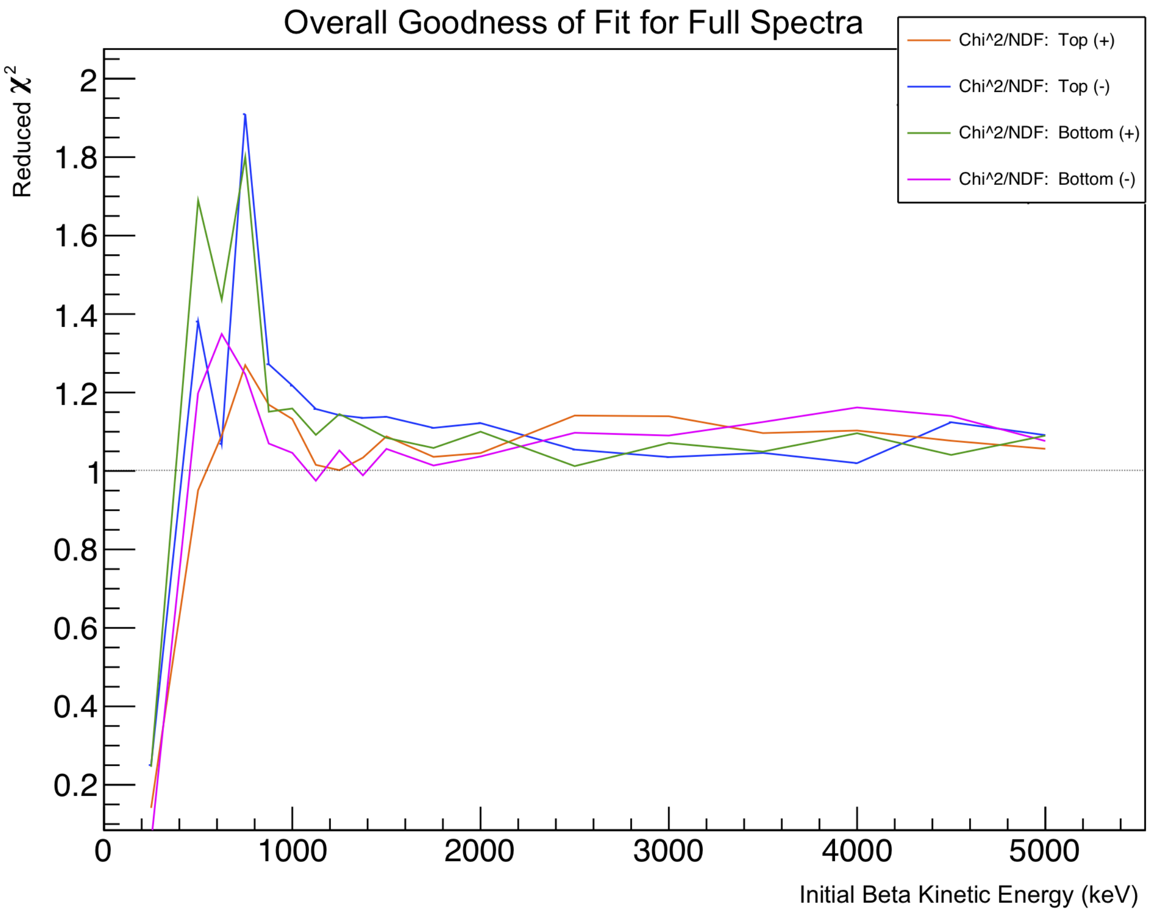

Figure 5.9: Goodness of fit for modeled response functions, for all four detector+polarization combinations. The models are clearly much better behaved at initial energies above $\sim 1200\,\mathrm{keV}$.

5.4 Modeling the Scattering Effects from the Cloud

Beta scattering — in which a beta originating within the atom cloud is incident on a surface within the chamber and changes its trajectory, losing some if its energy in the process — is a significant systematic within this experiment, and it must be evaluated, quantified, and corrected for. While only a small fraction of events are affected, the process results in a change to the beta energy spectrum that can easily be misinterpreted as the exact signal we are searching for. It is therefore imperative that this be well understood.

The scattering process can result both in scenarios where a beta that was initially directed away from the detectors is scattered *into* a detector, and scenarios where a beta that was initially traveling towards a detector is scattered *away* from it. Since this is a polarized decay and the beta asymmetry is not zero, the relative likelihoods of each of these two scenarios depends on whether the nuclear polarization vector is directed toward- or away from the detector in question. In either case, it is clear that some events will be removed, and other events will be added in. As a further complication, betas that have been scattered into a detector will necessarily have a very different energy spectrum than unscattered betas, and neither are the betas that are scattered away from a detector removed uniformly from the original energy spectrum. With the four beta energy spectra comprising the essence of our observable, we must have a clear understanding of the results of this process within our data.

Despite these complications, it is clear that for events in which the beta is scattered from a surface prior to its incidence on a detector, the beta particle will take longer to travel from the position of its initial creation to the detector. Although it is not possible to fully separate scattered and non-scattered events from one another, a judicious choice of cut within the SOE-Beta TOF spectrum can still be used to lower the fraction of scattered events, improve our signal-to-noise ratio, and decrease the overall size of any systematic uncertainties associated with scattering.

It is useful to remember in the discussion that follows that a beta particle emerging from a nuclear decay is, in general, fairly energetic, with perhaps a few MeV of kinetic energy. In comparison, a shake-off-electron ("SOE" – see Chapter 2.1) typically has only a few eV of kinetic energy. As a result, within our experimental time-of-flight spectra, because it is not possible to observe the *true* time of decay, we have commonly used as a proxy the time at which a beta hit is detected. The betas are relativistic and can be treated (for these purposes) as travelling at the speed of light – therefore if we suppose that all detected betas proceed from the position at which they were created directly into a detector, then the beta hit timestamp provides an excellent proxy for the true decay time, with only a small and easily calculable timing offset.

Within this section, however, where the experimental SOE TOF spectra are examined in detail, the above assumption is insufficient, as it is necessary to consider effects from beta scattering – both to the observed beta energy spectra, and also to the observed beta time-of-flight spectra (which, of course, are only experimentally meaningful in comparison with another timed observation).

Using Geant4, a set of beta time-of-flight spectra is generated for decays originating from within the atom cloud for all four detector+polarization combinations, and it is clear that there is a small but non-negligible fraction of such events that arise from beta scattering events. Even within Geant4, where is *is* possible to measure the beta time of flight with respect to the initial time of decay, the scattered and unscattered spectra cannot be fully separated from one another. The strong correlation between emission angle and time-of-flight does, however, suggest that the signal-to-noise ratio could be improved by a judicious cut on the TOF spectra. In order to produce something which can be directly compared with experimental data, a TOF spectrum for SOEs must also be produced and merged with the beta TOF spectrum. Experimentally, this is done as an event-by-event subtraction, so that is also what must be done for the simulations. Unfortunately, these two time-of-flight spectra cannot easily be produced within a single type of simulation. Because scattering is an important effect within the beta time of flight spectra (and resulting beta energy spectra), Geant4 is the tool of choice for this type of particle. For shake-off electrons, which are emitted with little energy and accelerated through the electric field within the chamber, it is much more important to have an accurate model of the electric field and its effects on charged particles. The shake-off electrons' time of flight is therefore evaluated by the TRINAT collaboration using COMSOL to track individual electrons through a model of the electric field within the experimental geometry.

The COMSOL SOEs were generated with starting positions taken from a 3D gaussian distribution near the chamber centre, with the precise position and size parameters taken from measurements using the rMCP, as in Table 4.3. They are emitted with initial trajectories distributed isotropically. Three sets of SOE events are created: two with initial energies taken from the Levinger $4S$ and $3P$ spectra in the range of 0–100 eV, and the third with no initial kinetic energy. The origin of these SOE energy distributions is discussed in Section 2.1.

A final simulated SOE TOF spectrum (relative to the time of decay) was produced as a linear combination of these spectra, comprised of 9% 0 eV events, 77% $4S$ events, and 14% $3P$ events. The relative contributions of each of these components arose from a comparison with experimental data, and the collaboration found that the distribution of hit positions on the eMCP was well modeled by Levinger's formulae. There was only a very weak dependence on the relative number of SOEs removed from the $4S$ and $3P$ shells, though it turned out to be very important that the distributions not be truncated at too low an energy—a surprising result given the fact that both distributions are strongly peaked at much lower energies, and many of the higher energy SOEs are able to escape the central electric field region and therefore escape detection. The addition of the 0 eV events from $^{37}\mathrm{Ar}^-$ ions to the spectrum also greatly improved the fit.

With both a SOE TOF spectrum generated by COMSOL and a beta TOF spectrum generated by Geant4, the two spectra were combined event-by-event to produce a simulated "SOE – Beta" TOF spectrum to match the form of the data collected from the experiment. Note that although the simulated SOEs were generated from a model of the atom cloud, the betas generated by Geant4 were simply treated as originating from a pointlike distribution at the chamber centre. Since the betas are relativistic and the cloud is small, any changes to the beta spectrum as a result of this model would be too small to be seen given the timing resolution of our detectors (~ 0.1 ns).

This "SOE – Beta" spectrum is convoluted with a gaussian of width $\sigma = 0.443$ ns to model the timing jitter within our detectors. The width of this gaussian is taken from a measurement of the "prompt" peak (betas incident on the eMCP before scattering into a scintillator) within the equivalent experimental spectrum. Results for Levinger SOEs and 0eV SOEs are shown in Fig. 5.10.

5.5 Simulating the Background and Time of Flight

One of the largest sources of background events in this experiment is from decaying ^{37}K atoms that have escaped from the trap and become stuck on the other surfaces

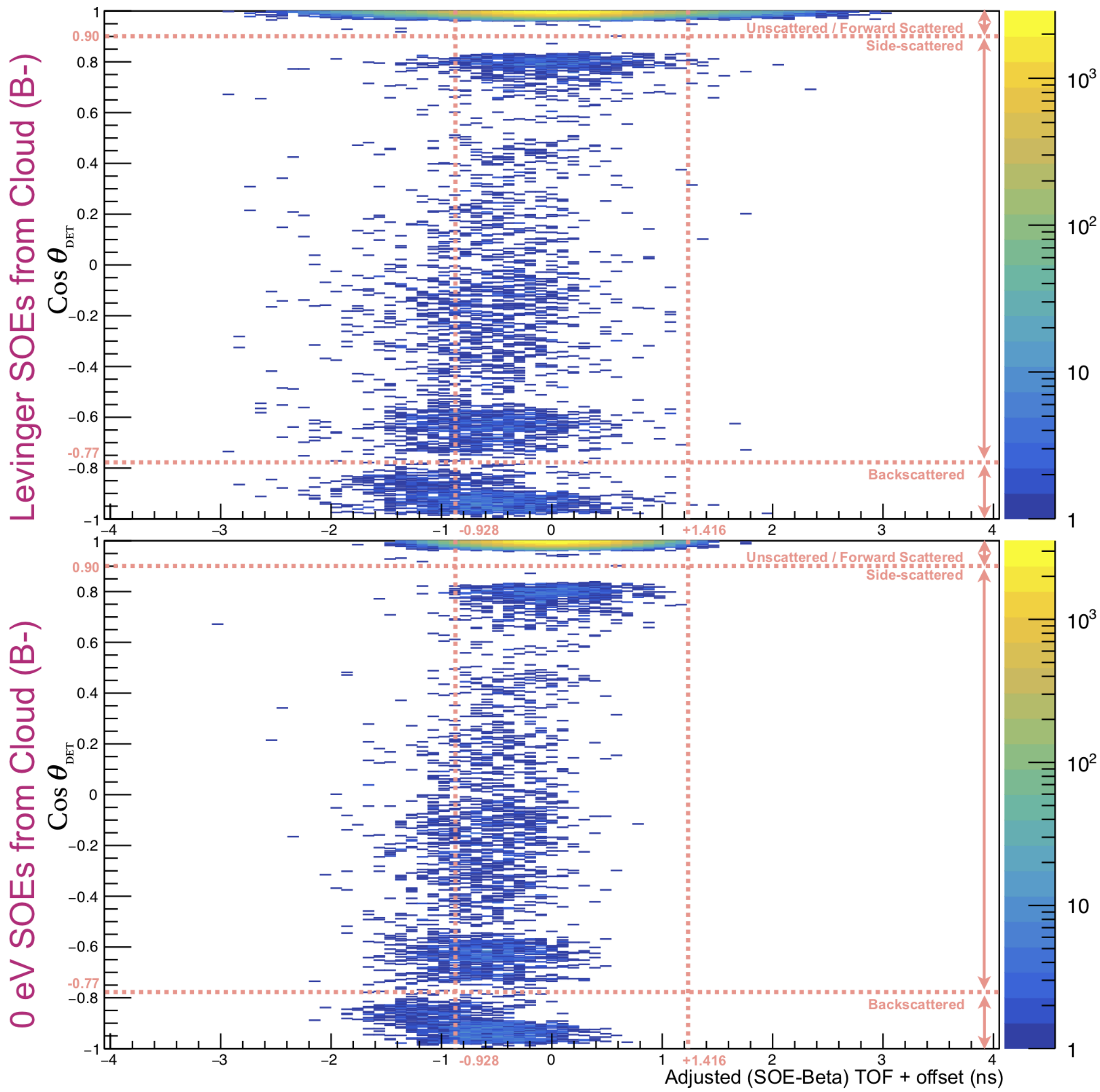

Figure 5.10: Simulated Beta emission angle with respect to the detector in which the event is eventually observed(G4), plotted versus an adjusted SOE – Beta TOF (COMSOL, G4). SOEs are simulated with initial energy distributions adapted from Levinger (top), and with no kinetic energy at all (bottom). The TOF cut that will eventually be taken is shown, and events are classified into scattering categories for later evaluation as a systematic (see Ch. 6.2.1).

within the chamber. The majority of these events can be eliminated simply by taking a time-of-flight cut on the eMCP relative to a scintillator hit time (as described in Section 4.10). Unfortunately, this procedure cannot remove the entirety of the background, so what remains–both background events from chamber surfaces, and events from the atom cloud itself–must be modeled and understood.

The model used for events originating from the atom cloud is described in Section 5.4, and this section will discuss events originating from other surfaces within the chamber. The methodology used is very similar.

Spectra for both the beta time of flight and shake-off electron time of flight (calculated with respect to the time of decay) were generated, using Geant4 and COMSOL, respectively. For these background events, the SOE and beta were both generated to originate on certain surfaces within the experimental chamber. Because the surfaces from which generated SOEs had a viable path through the electric field onto the eMCP is relatively large, the SOE and beta spectrum must be generated, event-by-event, to originate at the same position. This procedure not only allows us to account for differing beta times of flight resulting from different distances to either detector, it also captures the differing energy loss from scattering for observed betas originating at different positions.

To model the distribution of atoms stuck to surfaces within the chamber, we suppose that all escaped atoms were lost from the central cloud in an isotropic manner, so that the number of atoms on an object's (infinitesimal) surface element is given by the (infinitesimal) solid angle spanned by it. This principle is used both to normalize the relative number of decay events between different surfaces, and also to produce the distribution of events on a given surface. Then, for each surface of interest to us, a set of Geant4 beta decay events are generated from starting points on that surface, with those starting points distributed as described above. The beta particles are tracked through the geometry, and only events in which a beta is incident on a scintillator are saved.

For Geant4 events in which a scintillator hit is recorded, these events' start positions are then fed into COMSOL and used as start positions for SOE events, generated by the collaboration with the same energy spectrum that was used for events from within the cloud, as described in Sec. 5.4. For these events, only the ones in which an SOE was incident on the eMCP were preserved. An event-by-event subtraction is then performed on the timing results of the Geant4 and COMSOL Monte Carlo spectra, such that for every event that is preserved, the SOE in COMSOL and the beta in Geant4 will have originated from the same starting position. The results are then convoluted with a $\sigma = 0.443\,\text{ns}$ width gaussian to model timing jitter, as in the case of events originating from the cloud (Sec. 5.4).

With a simulated "SOE – Beta" TOF spectrum to compare with experimental data, it is possible to estimate how many such events remain (and what their energy distribution looks like) after a cut on the experimental spectrum is performed. The results are shown in Fig. 5.11. An upper limit for the fraction of events generated this way can be estimated by assuming that all losses from the cloud not attributable to radioactive decay must emerge isotropically and then stick to whatever object is in its path. This method overestimates the amount of background by around a factor of 2.

In order to check this model's performance, the energy-averaged superratio asymmetry is asembled for each time-of-flight bin within both our simulated and experimental spectra, as in Fig. 5.12. The modeled background is treated as being unpolarized. Although the two plots diverge rapidly outside this TOF range, an evaluation of the χ^2 statistic within this range produces a suspiciously good result.

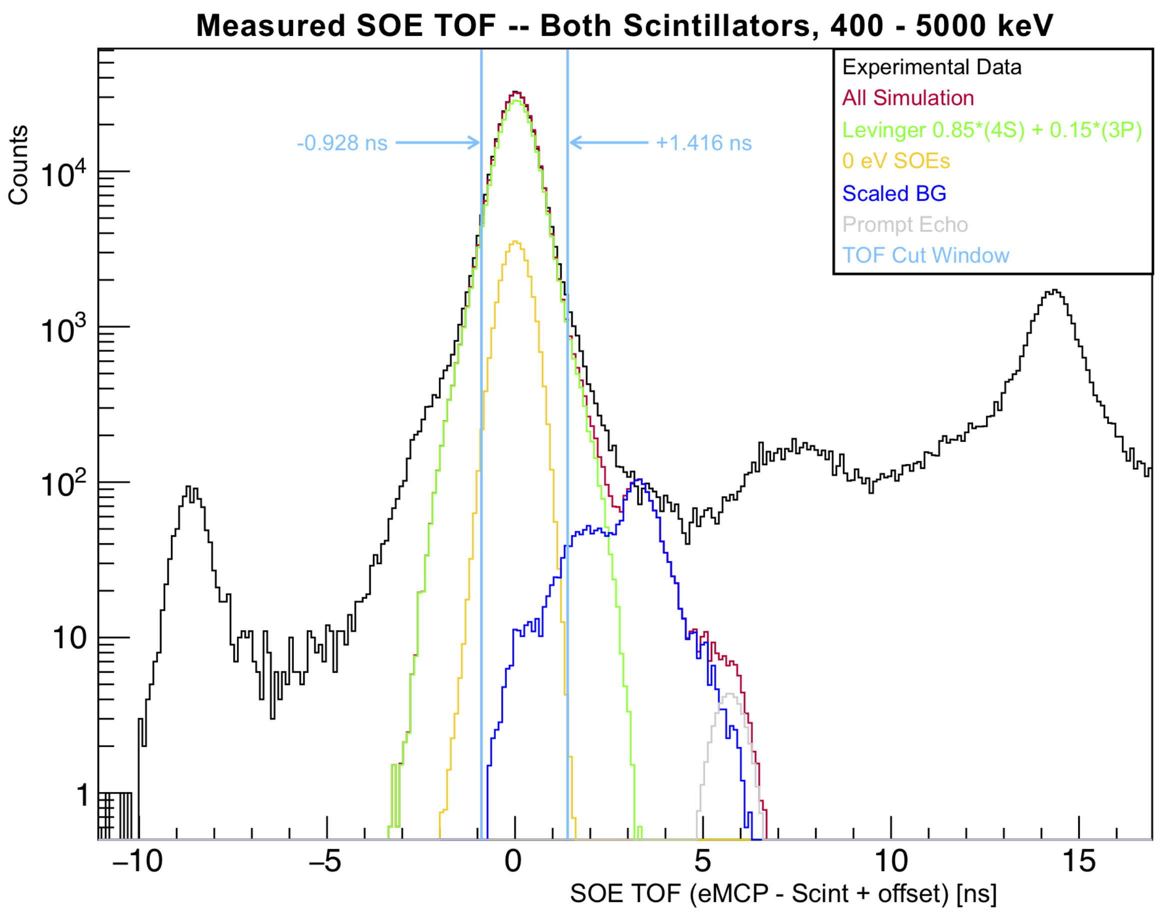

Figure 5.11: (SOE–Beta) TOF, with both model and experimental data shown. Spectra from simulations are separated according to their source, and the final TOF cut is drawn on. The background spectra have been scaled down by about a factor of 2 from their estimated maximum in order to match experimental data. Similar quality results are achieved no matter how the Levinger SOEs are distributed between 4S and 3P orbital shells, however adding the 0 eV electrons to the spectrum produces a large improvement to the agreement between the model and experiment.

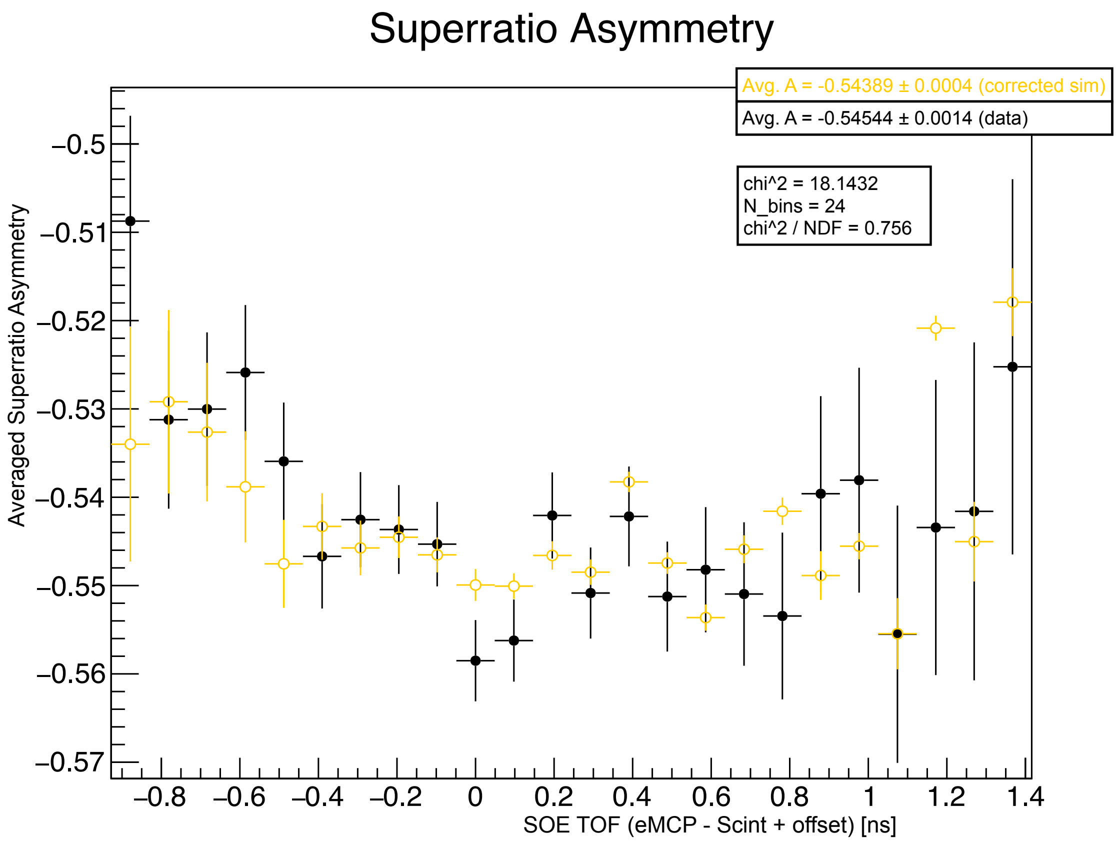

Figure 5.12: The superratio asymmetry, averaged over all scintillator energies between 400-4800 keV, is used to compare the experimental data and simulated TOF model as a proxy for the quality of the model to estimate the background. Background events are treated as being entirely unpolarized. All other cuts have been applied.

Chapter 6

Analysis and Estimates of Systematic Effects

The collaboration has performed an independent analysis using (mostly) the same set of data to measure A_β, fixing b_{Fierz} to zero. Differences with that analysis are interleaved in this section and summarized in Appendix B. Critical physics improvements concern an eMCP-beta timing walk correction which enabled an improved cut against background, also incorporating a more complete modelling of decay backgrounds from untrapped atoms. Technical corrections include a correct treatment of the polarization cycle. An arbitrary change in the DSSD radius cut is kept self-consistent.

6.1 Comparing Simulations to Experimental Data: The General Methodology

The primary parameter measurement strategy in this project involved comparing the experimental data to a 2D parameter space of simulations, and this is true both for evaluation of the best parameter values, and also for evaluations of the uncertainties.

As described in Section 1.6, and in more detail in Appendix 1.6, the primary experimental observable is the superratio asymmetry, which is constructed from four experimental *rates* of beta detection:

$$A_{\mathrm{super}}(E_\beta) \quad = \quad \frac{\sqrt{r_{\mathrm{T}-}\, r_{\mathrm{B}+}} - \sqrt{r_{\mathrm{T}+}\, r_{\mathrm{B}-}}}{\sqrt{r_{\mathrm{T}-}\, r_{\mathrm{B}+}} + \sqrt{r_{\mathrm{T}+}\, r_{\mathrm{B}-}}}. \tag{6.1}$$

This quantity is closely related to the two fundamental parameters we hope to extract, and in the absence of certain systematic effects, we can cleanly describe a relationship between the observable and the two physical parameters (A_β and b_{Fierz}) that we might use to describe the shape of an experimentally measured $A_{\text{super}}(E_\beta)$ curve:

$$A_{\text{super}}(E_\beta) \;=\; \frac{A_\beta \,\frac{v}{c}\, |\vec{P}|\, \langle|\cos\theta|\rangle}{1 + b_{\text{Fierz}} \frac{mc^2}{E_\beta}}. \tag{6.2}$$

Of course, when all systematics are properly accounted for, Eq. 6.2 is no longer an adequate description of the full relationship between the observable and physical parameters and a comparison to monte carlo must be used. A series of Geant4 simulations are performed and the results are (re-)processed with slightly different cuts and calibrations so as to match with the experimental conditions in each of the three electron datasets, and the superratio asymmetries are constructed. The degree to which the simulations and experiment match is evaluated by using a χ^2 comparison of the superratio asymmetries as the figure of merit (see Figs. 6.1,6.2,6.3). This is repeated for a range of A_β and b_{Fierz} values, and a χ^2 mapping of the 2D parameter space is produced.

For each superratio asymmetry constructed from simulated spectra, the scintillator spectra from which the superratio asymmetry is comprised are created as a linear combination of Geant4 beta decay events originating from the atom cloud and from surfaces within the chamber. Both components of the spectra are combined event-by-event with SOE events generated in COMSOL, as described in Sections 5.4 and 5.5, as this is necessary for the critical time-of-flight cut on the "SOE – Beta" spectra. For decays originating within the atom cloud, both the primary decay branch and the subdominant 'two percent' branch are allowed to contribute events, and only the dominant branch is varied as a function of BSM couplings. For background events, only the Standard Model primary branch is simulated.

A major caveat to the above description is that running a high statistics G4 simulation of our experiment is a computationally expensive process, so it was not possible to perform a separate simulation at every 'pixel' within the parameter space. Instead, to evaluate how well the experimental data matched to the expectation for varying values of A_β and b_{Fierz}, only three simulations were performed for different values of b_{Fierz}, all using the same nominal value for A_β. The $A_{\text{super}}(E_\beta)$ spectra representing

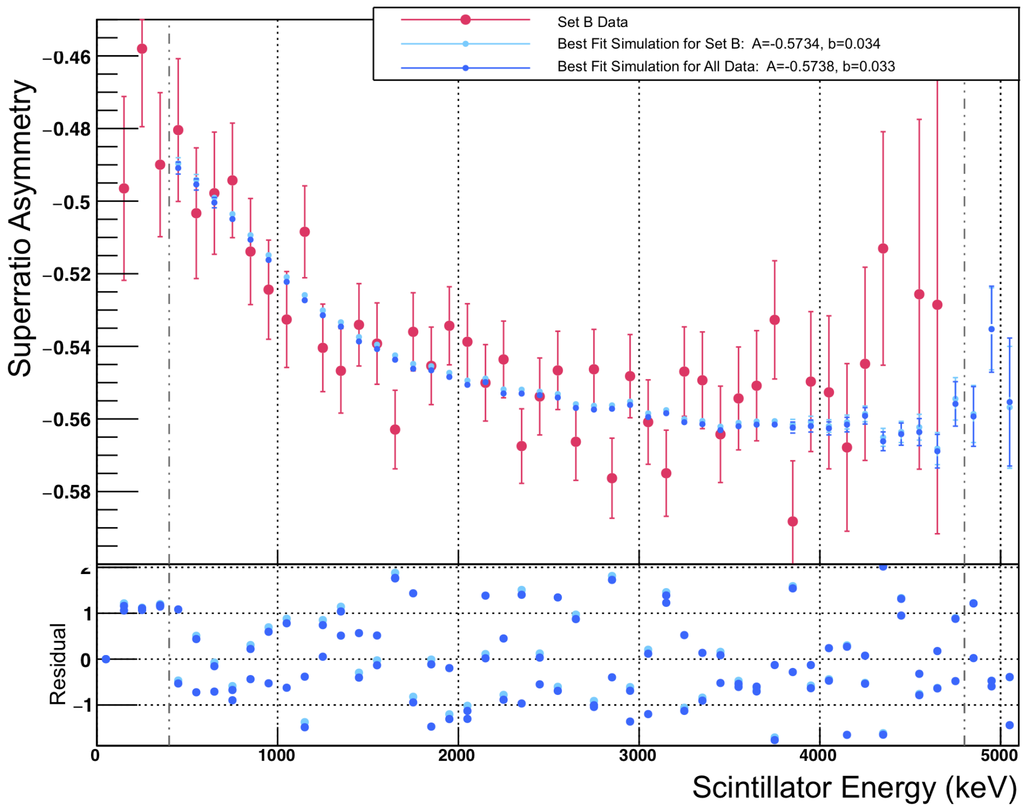

Figure 6.1: A superratio asymmetry from Dataset B, and the best fits from simulations.

intermediate b_{Fierz} values were created from a linear combination of spectra generated at the two closest values of b_{Fierz}.

To vary the effective A_β value, the generated $A_{\mathrm{super}}(E_\beta)$ spectrum was simply scaled. From Eq. 6.2 it is clear that this works well so long as b_{Fierz} is small and any systematics are evaluated separately. This method allows for an arbitrarily finely pixellated 2D χ^2 map to be created. It is done separately for each of the three experimental data sets so as to facilitate evaluation of systematic effects that changed between runsets. See Figs. 6.4,6.5,6.6.

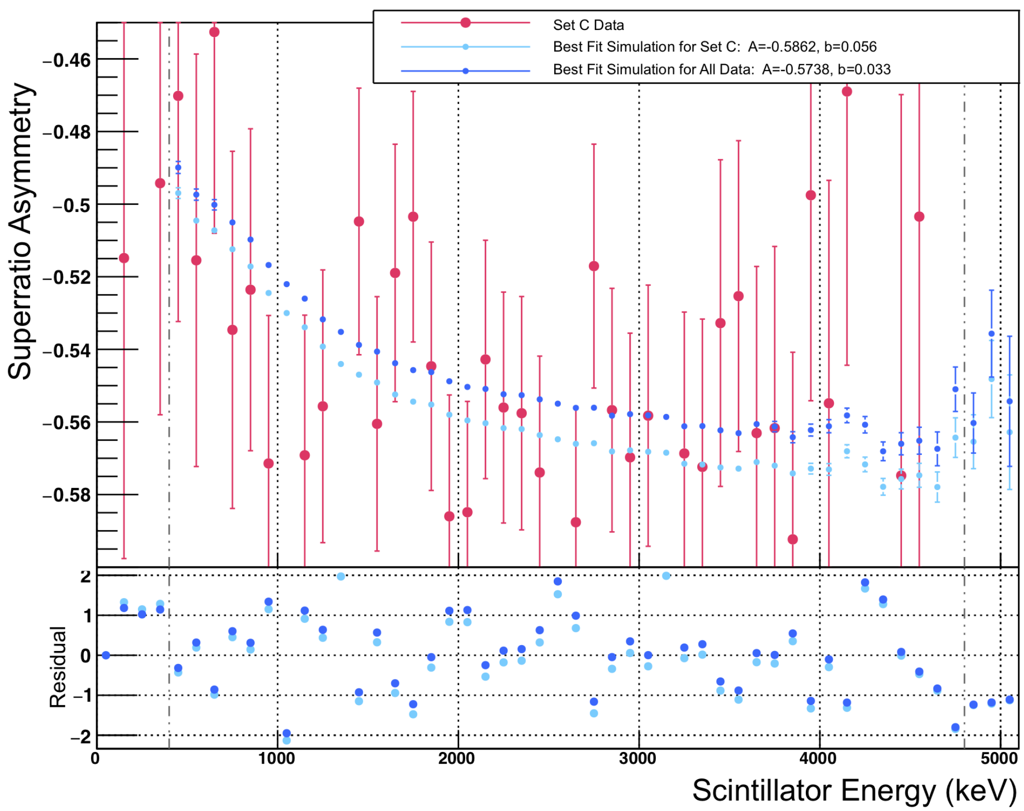

Figure 6.2: A superratio asymmetry from Dataset C, and the best fits from simulations.

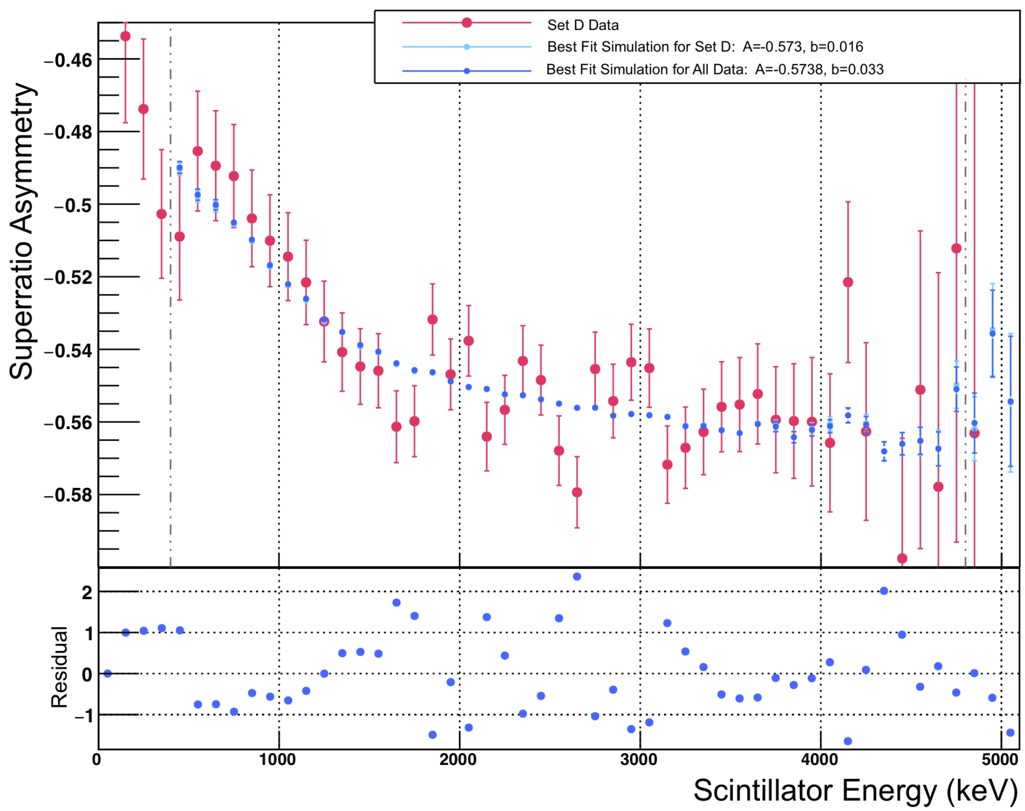

Figure 6.3: A superratio asymmetry from Dataset D, and the best fits from simulations.

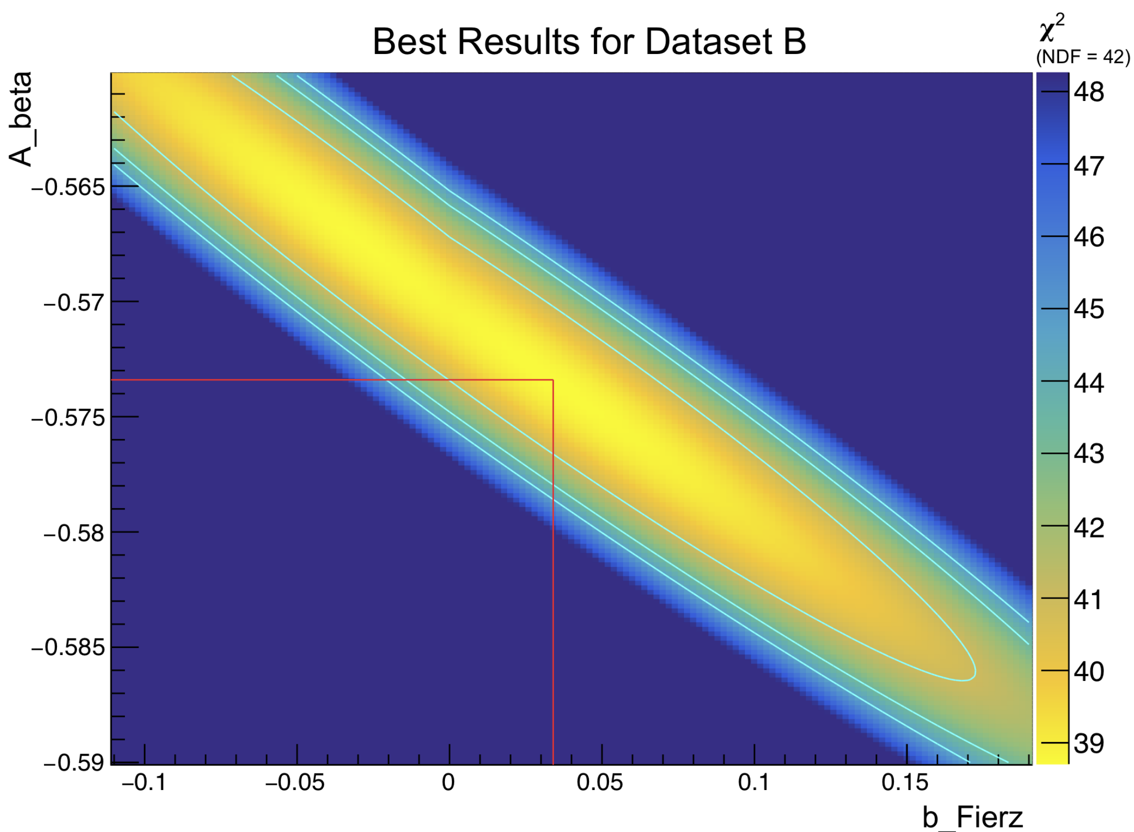

Figure 6.4: A χ^2 map to compare data from Runset B to a parameter space of A_β and b_{Fierz} values. The contours show 1σ, 90%, and 95% statistical confidence intervals.

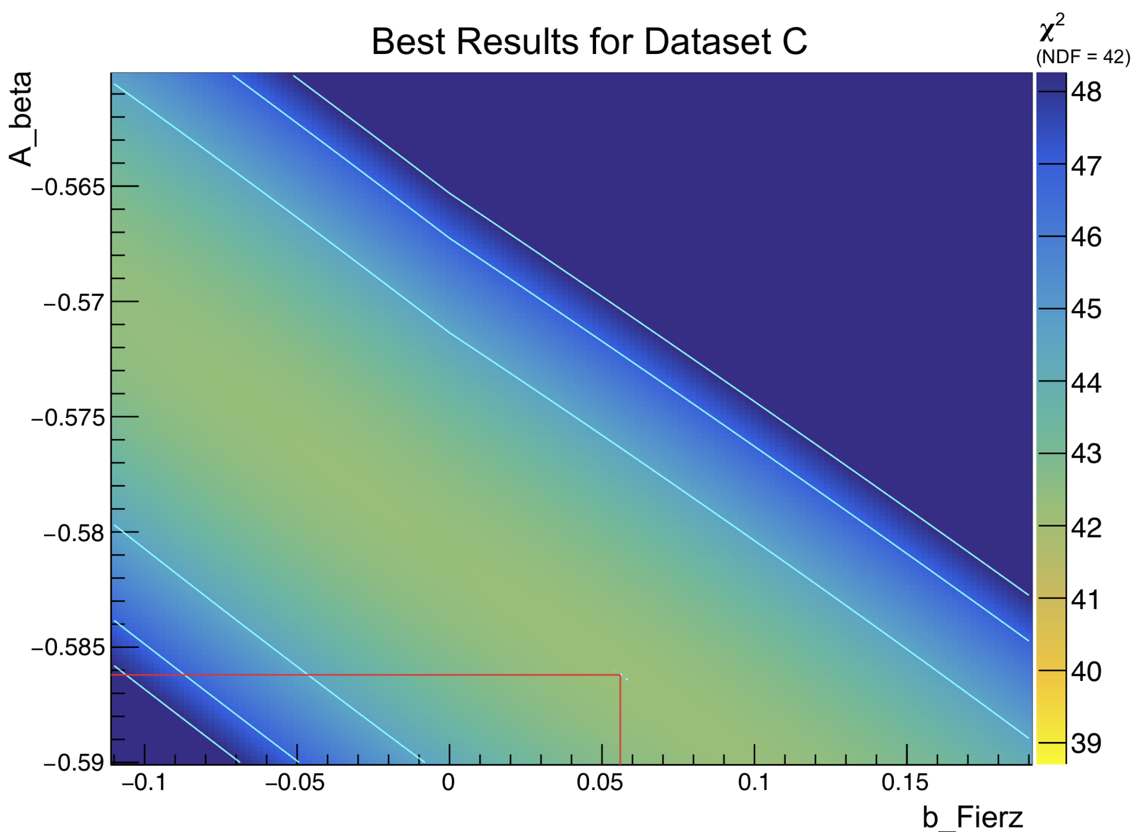

Figure 6.5: A χ^2 map to compare data from Runset C to a parameter space of A_β and b_{Fierz} values. The contours show 1σ, 90%, and 95% statistical confidence intervals.

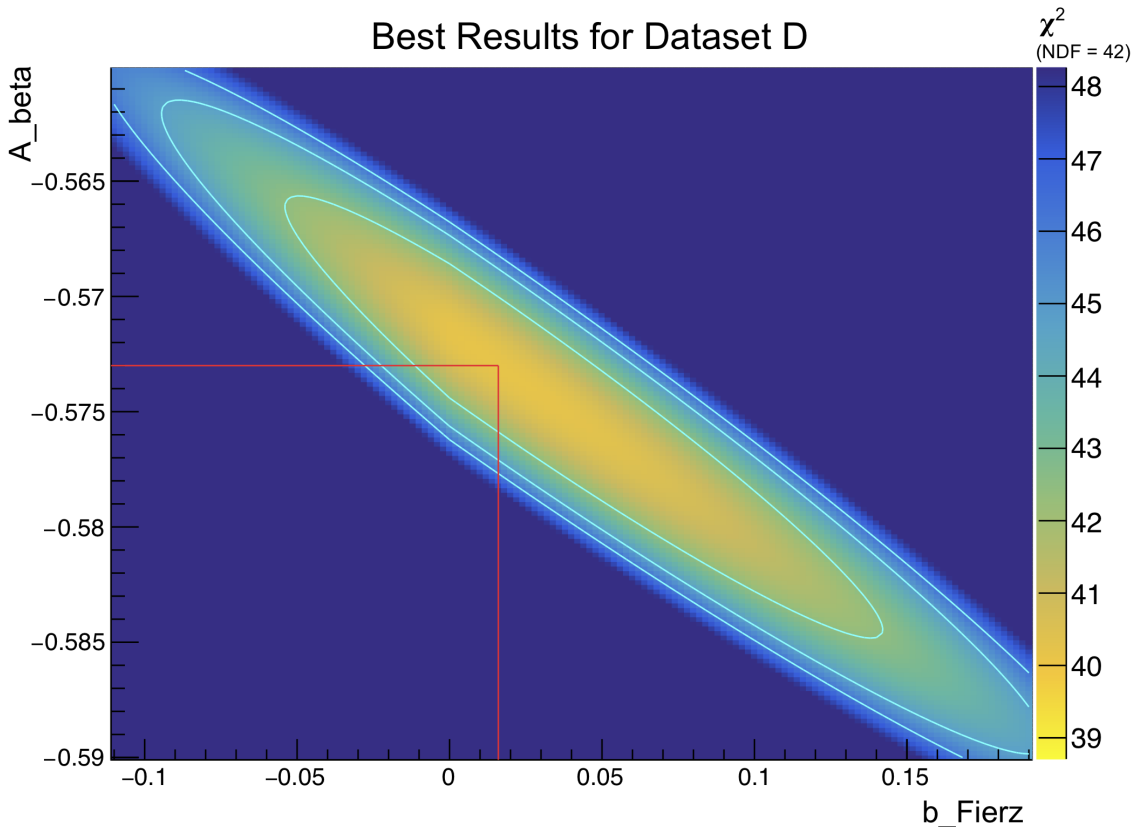

Figure 6.6: A χ^2 map to compare data from Runset D to a parameter space of A_β and b_{Fierz} values. The contours show 1σ, 90%, and 95% statistical confidence intervals.

6.2 Evaluation of Systematic Effects

6.2.1 Beta Scattering

The methodology used to simulate and model scattered events is described in Section 5.4. To evaluate the systematic effect on the final measurements arising from incomplete knowledge of how much beta scattering is present (i.e., how well we can trust the simulation to correctly model the amount of scattering), two sets of χ^2 maps very much like those in Section 6.1 are created, with the amount of scattering varied by one standard deviation. This does not require a new simulation; instead, for the three high statistics G4 simulations varying the BSM scalar coupling, all events passing the cuts are categorized into unscattered and forward-scattered events, sidescattered events, and backscattered events, depending on a comparison of the beta's emission angle to the detector in which it was eventually observed, as shown in Fig. 5.10.

The contribution from unscattered and forward scattered events is not allowed to vary, but the weights attributed to sidescattered and backscattered events was varied by $\pm 10\%$ and $\pm 5.1\%$ (respectively) relative to their 'best' values. Fig. 6.7 clearly shows the change in superratio asymmetry produced by this variation in the amount of scattering. The method by which it was determined how much the scattering weights should be allowed to vary is benchmarked in Refs. [101] [102], and is described further in the supplementary material of a recent publication by the collaboration [63].

Since errors in evaluating both side-scatter and backscatter arise from limitations on how well Geant4 is expected to perform, it is not clear how correlated these errors are, but it seems foolish to suppose they should not be correlated at all. Therefore, the conservative assumption that the two are *fully* correlated is taken, and the errors from side-scatter and backscatter are added *linearly* to one another before being combined in quadrature with the other uncertainties.

As this is the dominant systematic error, the TRINAT collaboration is working to improve the experimental design to use lower-Z materials to reduce the size of this effect.

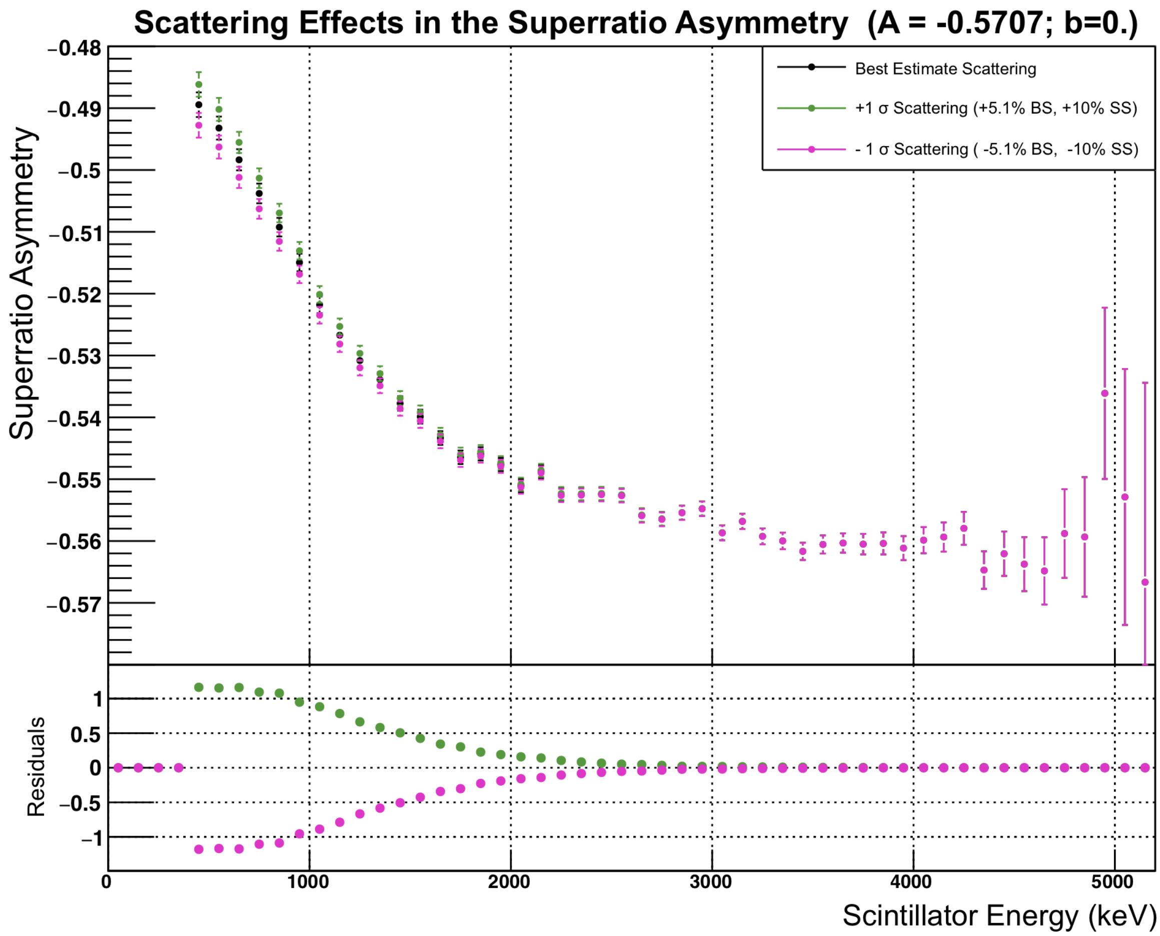

Figure 6.7: The amount of scattering is adjusted by one standard deviation in both directions, and the results to the superratio asymmetry are plotted. Backscattering and sidescattering errors are conservatively treated as being fully correlated. The bulk of the effect occurs at lower energies, where sensitivity to b_{Fierz} is at its highest.

6.2.2 Detector Calibrations and Thresholds

Scintillators

The two plastic scintillators were calibrated by the collaboration using online data, with reference points from the beta spectrum endpoint and the compton edge arising from annihilation radiation. Calibration was performed using only *polarized* data, because the final measurements use only polarized data, and the scintillator gain is more stable in the absence of the stronger oscillating magnetic fields from the AC-MOT.

A linear calibration is used, with

$$E_{\text{scint}} = \frac{1}{m}(Q_{\text{QDC}} - b), \tag{6.3}$$

and the detector resolution arising from photon counting statistics is given by

$$\sigma = \sqrt{\lambda E_{\text{scint}}}. \tag{6.4}$$

During online data collection, one QDC module failed abruptly and had to be replaced. As a result, the collected data is calibrated separately before and after the module failure, and the calibrations change slightly at this time. The methodology used is described in detail within [96], so the results will simply be stated here in Table 6.1.

Runsets			b	m	λ
EA, EB	RA, RB	Top	110.0 ± 0.3	0.3985 ± 0.0004	1.55 ± 0.09
		Bottom	142.0 ± 0.3	0.4234 ± 0.0004	1.28 ± 0.08
EC, ED	RC, RD, RE	Top	110.7 ± 0.2	0.3883 ± 0.0004	1.42 ± 0.08
		Bottom	143.0 ± 0.3	0.4132 ± 0.0004	1.32 ± 0.08

Table 6.1: Scintillator Calibrations

To evaluate the systematic effects associated with the scintillators' calibrations, the calibration for each scintillator is adjusted independently to produce energy measurements that are higher by one standard deviation, and lower by one standard deviation, and the resulting changes to the χ^2 map's A_β and b_{Fierz} centroids is measured. For this, the datasets corresponding to both sets of calibration numbers have their calibrations adjusted simultaneously, but each individual scintillator is treated separately. There is no reason to think the two scintillators' calibration accuracies should be correlated, so errors resulting from a changed scintillator calibration are added to one another in quadrature.

DSSD Radius, Energy Threshold, Agreement

Several parameters relating to our choice of cuts relating to DSSD calibrations are varied within both the experimental data and the simulated data to which it is compared. The detection radius, the overall energy threshold, the strip-by-strip SNR, and the energy and timing agreement (See Ch. 4.8) are each adjusted separately at the start of data processing, and the changes are propagated through to a final χ^2 map.

The changes to measured values of b_{Fierz} and A_β from these adjustments are comparatively small, and the errors are believed to be uncorrelated, so they are added in quadrature to the total systematic uncertainty.

6.2.3 The Atomic Cloud

Uncertainties relating to the position, size, motion, and expansion of the atomic cloud are evaluated using the response function, which is implemented as described in Ch. 5.3. To evaluate how well the simple monte carlo + response function (SMC+RF) performs in evaluating uncertainties, the relationship between how the SMC+RF and the full G4 simulation changes when a BSM parameter is adjusted is considered in Fig. 6.8.

To evaluate the propagated systematic effects arising from our knowledge of the cloud position, the simple monte carlo is used to generate events originating at points chosen randomly from the distributions produced by linear interpolation of the parameters in Table 4.3, with each parameter describing the distribution allowed to vary in accordance with its stated uncertainty, assuming gaussian-distributed errors. The results for each of the three datasets are shown in Fig. 6.9 for A_β and Fig. 6.10 for b_{Fierz}.

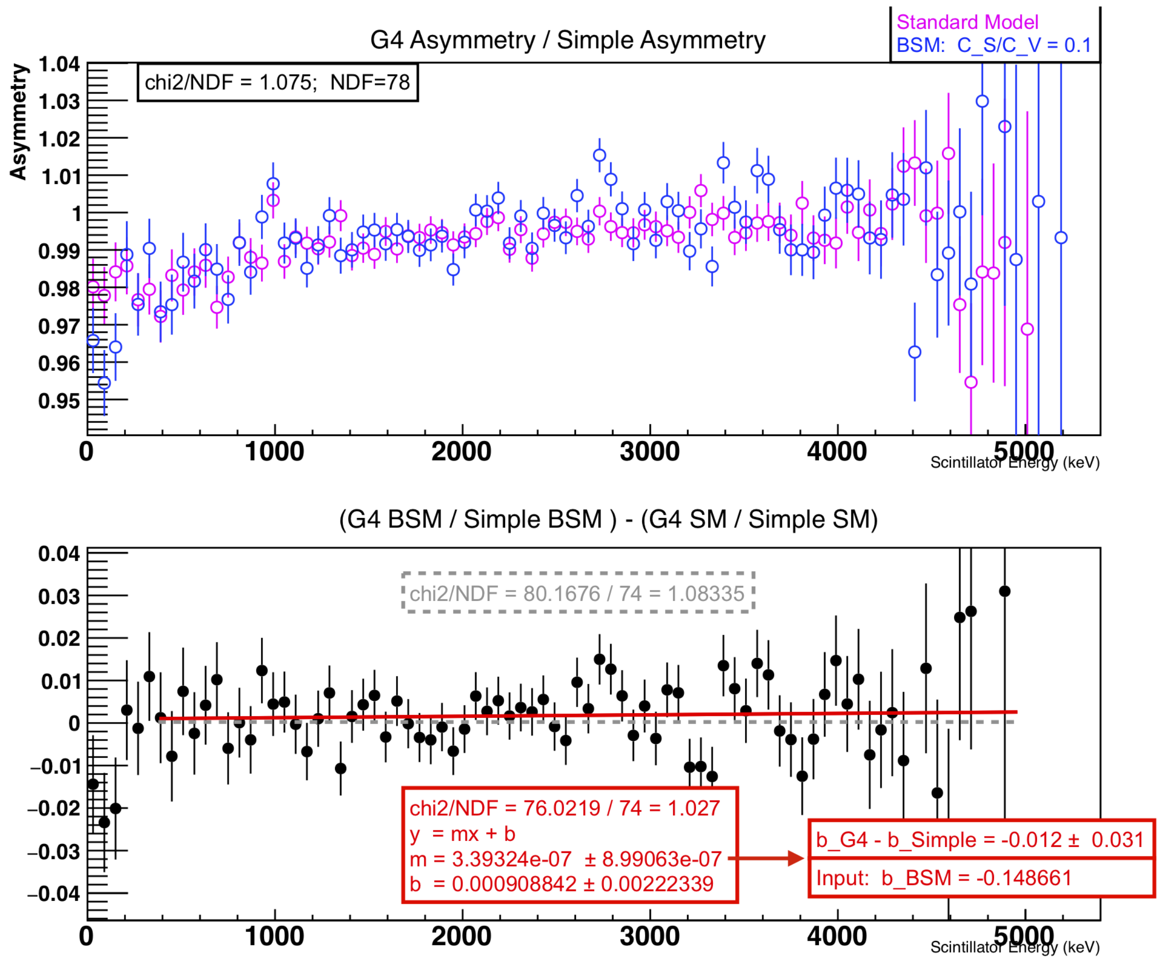

Figure 6.8: Superratio asymmetries generated by G4 and SMC+RF are compared against one another for a change in BSM parameters. The results show a consistent behaviour when the value of b_{Fierz} is adjusted, suggesting that the SMC+RF can safely be used to evaluate systematic effects such as those arising from a change in cloud position.

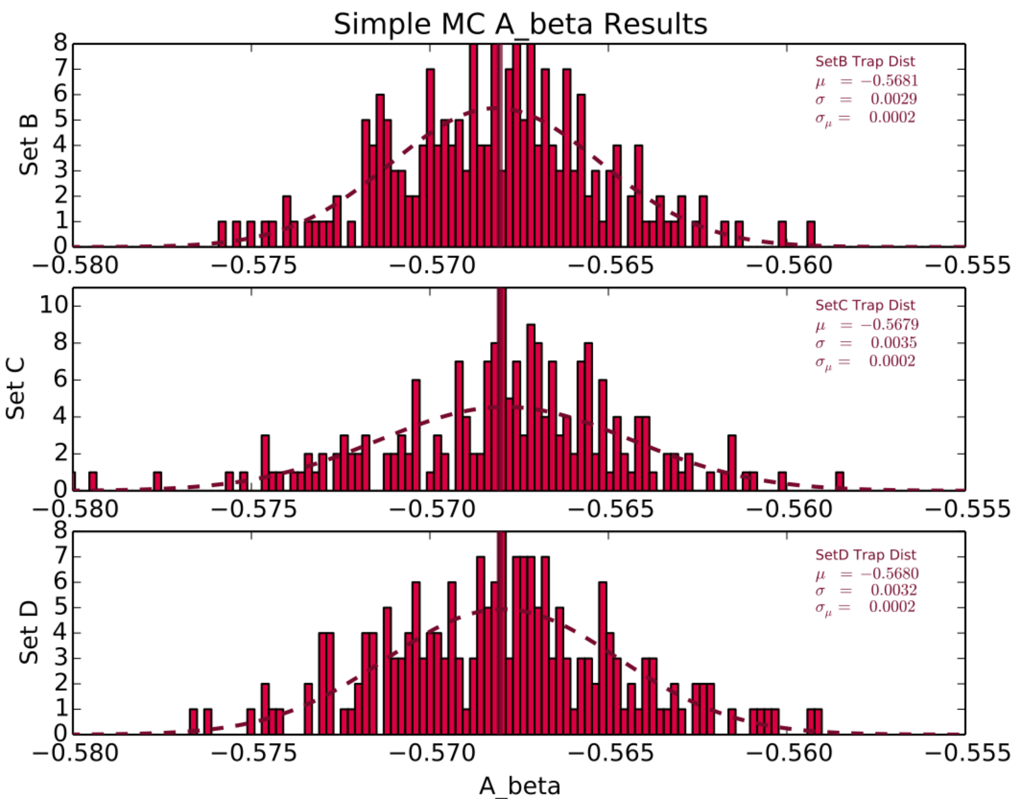

Figure 6.9: Estimated offset and uncertainty in A_β resulting from an imperfectly centred cloud of finite size, and the uncertainty and variation within these parameters. Evaluated by using the SMC+RF method.

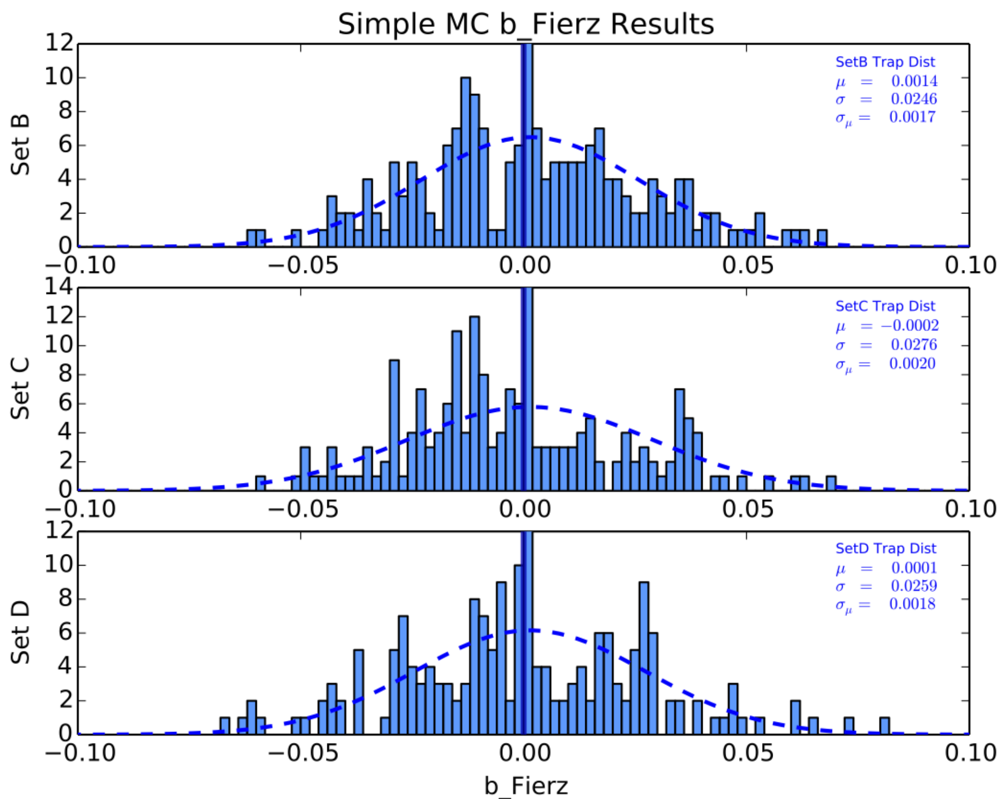

Figure 6.10: Estimated offset and uncertainty in b_{Fierz} resulting from an imperfectly centred cloud of finite size, and the uncertainty and variation within these parameters. Evaluated by using the SMC+RF method.

6.2.4 The Response Function's Low Energy Tail

This subsection has the collaboration's evaluation of the uncertainty from the scintillator detector's lineshape tail. The energy from a monoenergetic beta is not always fully absorbed in a plastic scintillator. Although most backscattered betas are vetoed by the DSSD, some produce bremsstrahlung photons, and these frequently escape low-Z plastic scintillator– all cross-sections are known to high accuracy, but there is always uncertainty entailed in the MC implementation. This lineshape tail will then effectively move events from higher to lower measured energy, artificially altering the lower-energy asymmetries and mimicking the effects of a Fierz term.

Since this detector effect is difficult to disentangle from the other scattering effects off volumes, the collaboration adds a linear function down to zero for the tail to a Gaussian for the peak, with linewidth varying by photon statistics [98]. The convolution of this simple detector response function with v/c then scales the centroid MC, with the lineshape tail varied by $\pm 10\%$ of its value, a generic uncertainty accepted by the community for MC electromagnetic simulations. The fit b_{Fierz} centroid changes by $\pm$ 0.0076, summarized as the 0.008 "Low Energy Tail" in the systematics table at the start of this chapter. When compared with other uncertainties of the present data set, this is small enough that the accuracy of this estimate is adequate.

6.2.5 Background Events

Modeling of background events is coverered comprehensively in Ch. 5.5. Because the background model doesn't fully fit the experimental TOF spectrum, a relatively large variation in the number of background events is considered. The background spectrum is scaled from its nominal size up by a factor of 2 and down by a factor of 2.

Since the background has been reduced greatly by the improved time-of-flight analysis, this even this large variation in the number of background events makes a relatively small contribution to the final result.

6.2.6 Material Thicknesses

There are three distinct objects a beta emitted from the central atom cloud must pass through before arriving at a scintillator: a $(275 \pm 6)\mu$m silicon carbide mirror, a $(229 \pm 23)\mu$m beryllium foil, and a $(295 \pm 5)\mu$m double-sided silicon strip detector, as shown in Fig. 3.4.

The propagated uncertainties are treated as uncorrelated (added in quadrature), and evaluated by running high-statistics Geant4 simulations with a parameter adjusted, then propagating the result through the analysis pipeline to compare against superratio asymmetries constructed to span the 2D BSM parameter space. Because of the processor time required for this, certain simplifying assumptions were used to reduce the necessary number of simulations. In particular, the top and bottom for each type of object were treated as producing the same size propagated uncertainty, though the top and bottom errors were not treated as being correlated. Simulations were run to ensure there would not be any large nonlinear effects when combining a change in thickness for one type of object.

Furthermore, since the DSSD and the mirror have a similar density of silicon, which is the dominant material in causing scattering from the mirrors, and because the two have as a similar thicknesses and thickness uncertainties, the the propagated uncertainties from the DSSDs and mirrors were assumed to produce similar size effects on the result. Thus, the uncertainties arising from uncertainties in the beryllium foil and mirror thicknesses were the only ones evaluated directly within Geant4. The propagated uncertainty arising from DSSD thickness was assumed to be the same size as the uncertainty arising from mirror thicknesses.

All uncertainties from material thicknesses are believed to be uncorrelated, and are added in quadrature to the final systematic uncertainty.

Chapter 7

Results and Conclusions

7.1 Measured Limits on b_{Fierz} and A_β

After corrections have been applied and uncertainties evaluated, statistical confidence intervals for the 2D A_β vs b_{Fierz} parameter space are shown in Fig. 7.1 for all datasets combined. The final estimates of A_β and b_{Fierz} with uncertainties at the 1σ level are given by:

$$b_{\text{Fierz}} = \quad 0.033 \quad \pm 0.084(\text{stat}) \ \pm \ 0.039(\text{sys}) \tag{7.1}$$

$$A_\beta = \ -0.5738 \pm 0.0082(\text{stat}) \pm \ 0.0041(\text{sys}), \tag{7.2}$$

and a list of contributing uncertainties is provided in Table 7.1. The error is dominated by statistics, which is unsurprising given that the superratio asymmetry has been used, thereby decreasing systematic errors in exchange for an increase in statistical errors (see Appendix 1.6 for a further discussion of the superratio and superratio asymmetry).

7.2 Comparison to TRINAT's Prior A_β Measurement

The uncertainty associated with this measurement of A_β is significantly larger than the collaboration's previous measurement of A_β using the same data, in which the final result was $A_\beta = -0.5707 \pm 0.0013(\text{stat}) \pm 0.0013(\text{sys}) \pm 0.0005(\text{pol})$ [63] before correcting for a data selection issue that only became apparent after publication.

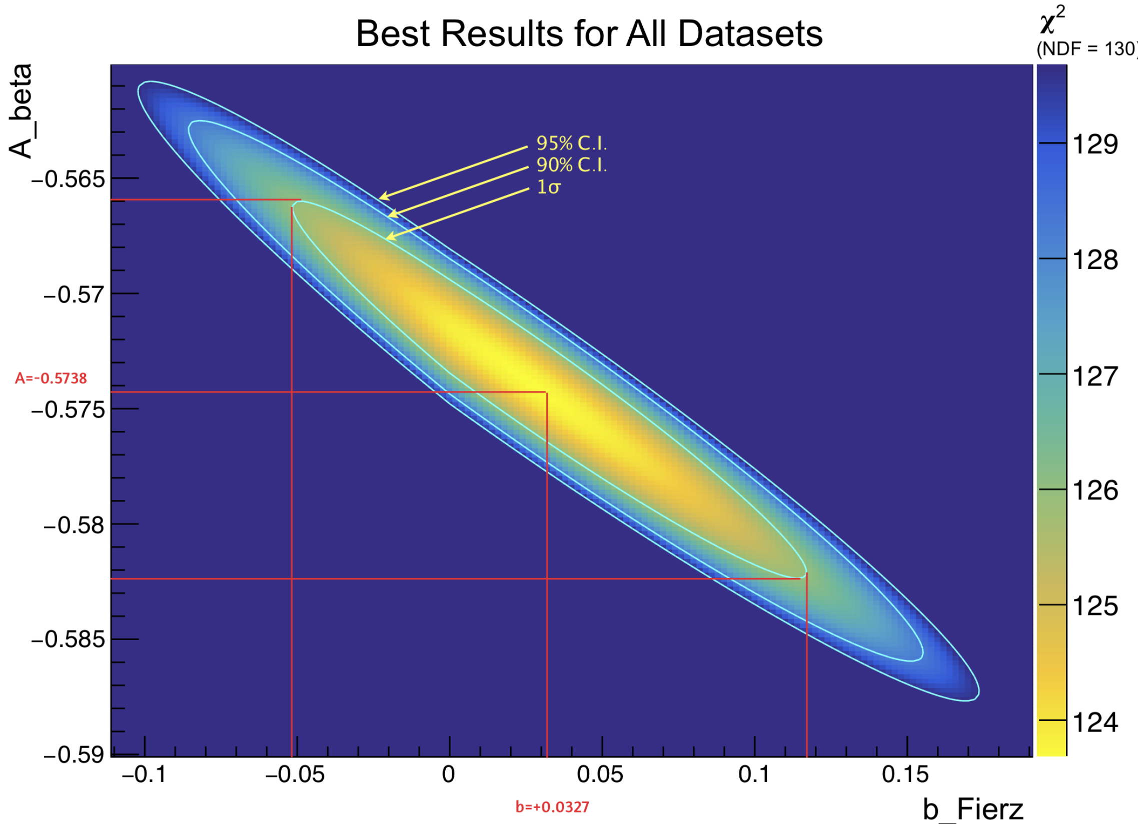

Figure 7.1: A χ^2 map to compare all data to a simulated parameter space of A_β and b_{Fierz} values. All corrections have been included, however only statistical confidence intervals are shown.

However, it must be noted that the present measurement is a two-parameter measurement rather than a one-parameter measurement, so it is expected that the uncertainty associated with a single parameter should be larger.

To evaluate whether the two measurements are consistent, a thin vertical slice of Fig. 7.1 can be extracted at $b_{\text{Fierz}} = 0$, and its projection will provide the centroid (including systematic offsets) and statistical error associated with a one-parameter analysis for A_β — though this method cannot produce an estimate of the extent to which systematic uncertainties might be different. This simple check gives a one-parameter measurement of $A_\beta = -0.5714 \pm 0.0020(\text{stat})$.

The above one-parameter result for A_β is consistent with the collaboration's prior uncorrected *and* corrected results, even after one accounts for the fact that the previ-

Error Budget

Source	Uncertainty	
	b_{Fierz}	A_β
Scintillator Calibration	0.003	0.0003
Scintillator Threshold	0.004	0.0004
DSSD Individual Strip SNR	0.006	0.0007
DSSD Energy Agreement	0.005	0.0006
DSSD Detection Radius	0.006	0.0017
DSSD Energy Threshold	0.005	0.0005
Atomic Cloud	0.002	0.0002
Background	0.004	0.0003
Beta Scattering	0.031	0.0025
Low Energy Tail	0.008	0.0007
Mirror Thickness	0.013	0.0017
DSSD Thickness	0.013	0.0017
Beryllium Foil Thickness	0.004	< 0.0001
Total Systematics	0.039	0.0041
Statistics	0.084	0.0082

Table 7.1: Error budget for the two-parameter analysis for b_{Fierz} and A_β, with all data included, and the individual contributions are discussed in detail within Ch. 6. All uncertainties are believed to be uncorrelated, and are added in quadrature. Final results: $b_{\text{Fierz}} = 0.033 \pm 0.084(\text{stat}) \pm 0.039(\text{sys})$ and $A_\beta = -0.5738 \pm 0.0082(\text{stat}) \pm 0.0041(\text{sys})$.

ous result suffered from an oversight in which some partially polarized data was not removed from the final analysis for A_β, despite the fact that this cut *was* implemented in the associated polarization measurement. This accounts for 5% of the data used in that analysis, and is estimated to decrease the average polarization by approximately 0.3%. An estimate of the size of the effect on the previous measurement of A_β suggests that the true value of A_β is likely to be ~ 0.0016 more negative than reported. Accounting for this, a more accurate one-parameter measurement might produce the result, $A_\beta \approx -0.5723 \pm 0.0014(\text{stat}) \pm 0.0013(\text{sys}) \pm 0.0005(\text{pol})$.

7.3 Relation to Present Limits on Scalar and Tensor Interactions

The best existing measurement of the Fierz interference term is in the decay of the neutron, with $b_{\text{Fierz}} = 0.017 \pm 0.021$ — consistent with the standard model prediction of zero, and with previous results for the neutron's b_{Fierz} [65][64]. Our measurement is strongly related, yet complementary. This result for b_{Fierz} cannot be directly compared to our result in ^{37}K, because the neutron's sensitivity to scalar and tensor couplings is different than our own. In particular, using ρ as defined in Eq. 1.19 we find:

$$b_{\text{Fierz}} = \frac{\pm 2\gamma}{1+\rho^2}\left(\frac{g_S}{g_V} + \rho^2 \frac{g_T}{g_A}\right) \tag{7.3}$$

where the top/bottom sign is for β^-/β^+ decay, and g_X $(X = \{V, A, S, T\})$ is a purely left-handed coupling for vectors, axial-vectors, scalars, and tensors [1][2]. In the case of ^{37}K, a previous measurement puts $|\rho| \approx 0.576$, while, in the case of the neutron, the equivalent quantity within Eq. (7.3) is ~ 2.215 [103][65][64]. The Fermi matrix element, $|M_F|$, is nearly the same for both of these isospin $= 1/2$ decays (the largest correction is the larger isospin mixing of $\sim$0.01 in ^{37}K). This means that our observable is comparatively less sensitive to Lorentz tensor currents, and will predominantly constrain or discover Lorentz scalar currents. See Fig. (7.2).

However, measurements of the superallowed $0^+ \to 0^+$ beta decays are able to produce constraints on scalar couplings which are unrivaled by any other type of measurement, and improving with every experimental generation. Though these transitions offer no sensitivity at all to tensor couplings, it would be incredibly difficult for a mixed transition measurement such as ours to compete on scalar coupling limits with the superallowed $0^+ \to 0^+$ transitions. At the time of writing, measurements of average E_β values from superallowed $0^+ \to 0^+$ transitions have together produced a constraint of $|C_S/C_V| \leq 0.0010$ at the 1σ confidence level [83].

Full considerations would require a weighted fit of b_{Fierz} experiments and similar observables [47], and are beyond the scope of this thesis. The info from this thesis, values of A_β and b_{Fierz} with their uncertainties, can together with the known fT value (lifetime and branching ratio) allow the community and/or the collaboration to include the results in a future constraint or discovery of scalar and tensor Lorentz

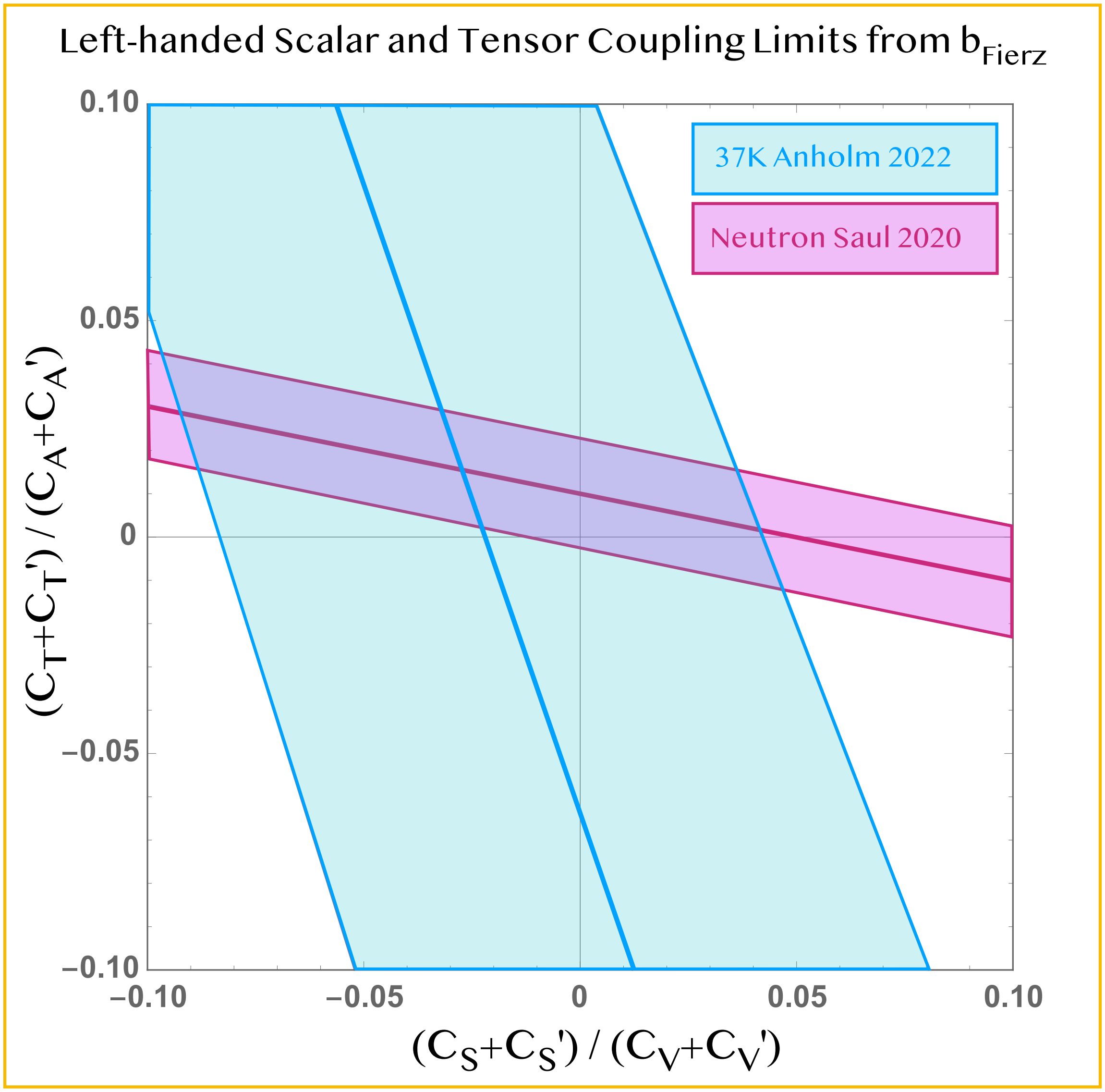

Figure 7.2: An exclusion plot comparing the measured 1σ limits for left-handed scalar and tensor couplings, comparing this work with the recent b_{Fierz} measurement in the neutron[65].

currents contributing to β decay.

7.4 Possible Future Work: R_{slow}

As discussed in Ch. 1, the nuclear weak force is known to be a predominantly left-handed vector and axial-vector ($V-A$) interaction – meaning that immediately following an interaction (e.g. beta decay) with a weak force carrying boson (W^+, W^-, Z), normal-matter leptons (such as the electron and electron neutrino) emerge with left-handed chirality, while the anti-leptons (e.g. the positron and electron anti-neutrino) emerge with right-handed chirality.

In the limit of massless particles, the particle's chirality is the same as its helicity. Thus, in a left-handed model, the direction of an (ultrarelativistic) normal lepton's spin is antiparallel direction of its motion, and the direction of spin for an anti-lepton is parallel to its direction of motion. For a non-relativistic particle the property of chirality is fairly abstract, and describes the appropriate group representation and projection operators to be used in calculations. It should be noted that a fully chiral model is also one which is maximally parity violating.

This odd quirk of the nuclear weak force is not only *predominantly* true, but it is, to the best of our current scientific knowledge, *always* true – that is, attempts to measure any right-handed chiral components of the weak force have produced results consistent with zero [84][104]. This project proposes a further measurement to constrain the strength of the right-handed component of the weak interaction.

Although the primary focus of this thesis is a search for exotic scalar and tensor couplings within the weak force, it is clear that a precision search for right-handed vector and axial-vector ($V + A$) interactions would be motivated by very similar rationale.

In the proposed experiment, we focus once again on the spin-polarized decay, $^{37}\text{K} \to\ ^{37}\text{Ar} + \beta^+ + \nu_e$, exploiting the principle of conservation of angular momentum as it applies to this transition. The proposed analysis could be performed on the data that has already been collected, although as we will see, there are some inherent difficulties to this approach which might be eliminated with a fresh set of decay data.

The decay process is as described in Appendix C. Within the JTW formalism, information about the handedness of any couplings is buried within the relative signs of the primed and un-primed coupling constants (C_X and C'_X, for $X = \{V, A, S, T\}$). Since this section describes a search for a different type of exotic physics, it is clear that the simplifications to be made within the JTW formalism will be different. Recall that for the expected pure left-handed interactions, the coupling constants obey the rule, $C_X = C'_X$ ($X = \{V, A, S, T, P\}$). For a purely right-handed interaction, the equivalent relationship is $C_X = -C'_X$. Since we know, at least for vectors and axial vectors, that the interaction must still be predominantly left-handed, one way to approach the problem is to define a new basis for the couplings to explicitly split the left-handed and right-handed couplings, as in:

$$C_X^L := \frac{1}{\sqrt{2}}(C_X + C'_X) \tag{7.4}$$

$$C_X^R := \frac{1}{\sqrt{2}}(C_X - C'_X). \tag{7.5}$$

The decay may be treated as a three-body problem in which the available kinetic energy is divided up between the beta, the neutrino, and the recoiling ^{37}Ar nucleus, and (of course) the total linear and angular momentum are conserved. While the neutrino cannot be detected directly, its kinematics may be reconstructed from observations of the beta and the recoiling daughter nucleus. By placing detectors above and below the decaying atom along the axis of its polarization, we are able to obtain information about the outgoing beta's energy and momentum, in the cases of interest to us, where it is emitted along (or close to) the axis of polarization.

It should be noted that for the class of decays of greatest interest, where the beta and the neutrino emerge back-to-back along the polarization axis, the recoiling daughter nucleus will have zero momentum along the directions perpendicular to this axis, and on average less total energy than if the beta and neutrino were emitted in a parallel direction. Henceforth, daughter nuclei from a back-to-back decay as shown in Figure 7.3 will be described as 'slow' recoils. In terms of observables, this means that if the electric field is configured to point along one of the axes perpendicular to the polarization direction, then when the recoiling ion is swept away into a detector, the slow recoil's hit position should be exactly along the projection of the polarization axis. Furthermore, the slow recoil's time of flight should be in the middle of the time of flight spectrum, since other recoils will be emitted with momentum towards or away from the detector. Of course, this is a simplistic description; in nature, no matter how strong the right-handed couplings, emitted particles will have a continuous angular spectrum – the above is only meant to describe the angular set up which would give us maximal sensitivity to observables relating to right-handed currents.

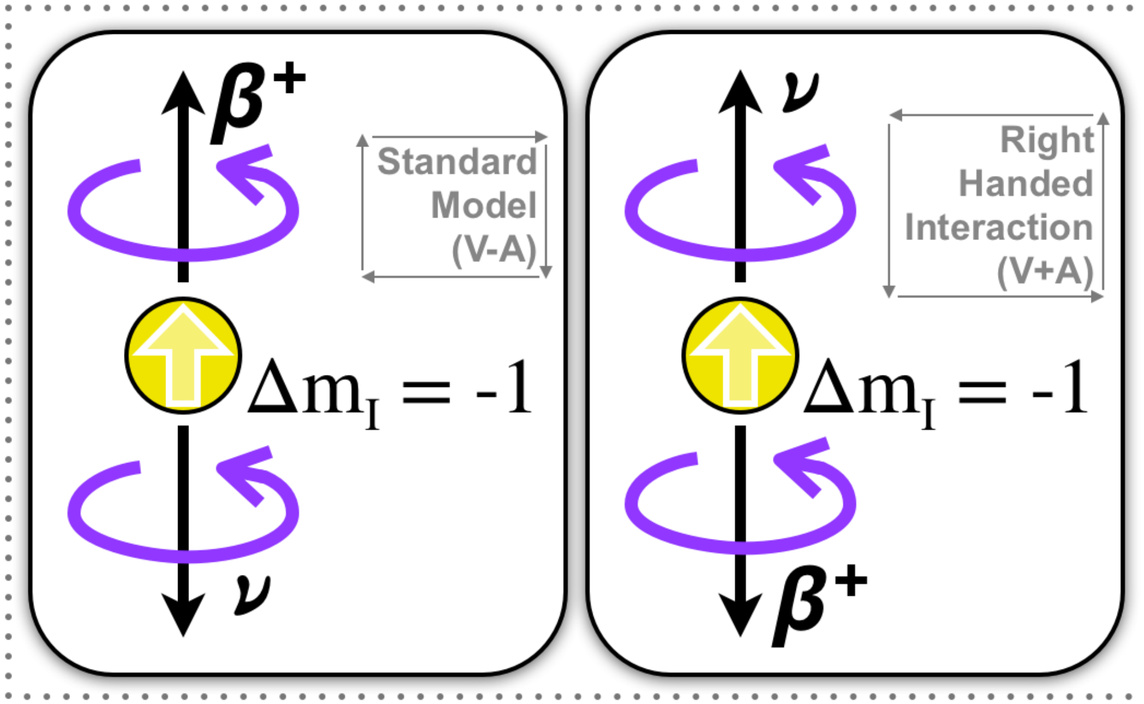

Figure 7.3: A comparison of left-handed and right-handed vector and axial couplings in polarized beta decay. The above are extremal examples; in nature there is no requirement for the leptons to be emitted back-to-back, or for either to be emitted along the axis of polarization. However the class of events with minimal momentum allocated to the recoiling daughter nucleus (i.e., the result of back-to-back lepton emission) is what provides the most sensitivity to the R_{slow} observable, and a β coincidence (our detectors are located along the axis of polarization) is required. The precise scenario on the right is the only one that is *completely* disallowed in the absence of right-handed couplings, and only in the relativistic limit. For intermediate decay scenarios, the probability is simply suppressed based on the extent to which the usual left-handed coupling can access the phase space.

The recoiling ^{37}Ar nucleus is a bit trickier to work with in some ways than an outgoing beta particle, but it is possible to do, and a necessary component of this measurement. One useful feature of the $^{37}\text{K} \rightarrow {}^{37}\text{Ar}$ transition is that, in addition to the β^+ emitted in the decay itself, one or more *orbital* electrons from the parent atom are typically lost. In the majority of decay events only one orbital electron is shaken off, which results in the daughter ^{37}Ar atom being electrically neutral [93][105]. In the remaining cases, two or more orbital electrons are lost this way, and the daughter atom is positively charged. If we apply an electric field perpendicular to the direction of polarization, these positively charged $^{37}\mathrm{Ar}^{(+n)}$ ions may be collected into a detector, from which hit position and time of flight information may be extracted. The shake-off electrons are emitted with an average energy of only $\sim 2\,\mathrm{eV}$ so to a very good approximation the other decay products are not perturbed by the presence of shake-off electrons[87].

The potential exists to use these shake-off electrons as a tag for good events, in a way similar to what has been done in the present measurements of b_{Fierz} and A_β. This could greatly improve the cleanliness of the spectra. Unfortunately, within the 2014 data that has already been collected, the recoil detector and electron detector could not be made to work simultaneously. Some of the resulting spectra are shown in Fig. 7.4. While an analysis to search for right-handed interactions could be performed on existing data, it would likely *significantly* improve the results if a new dataset were collected with both MCP detectors working at the same time.

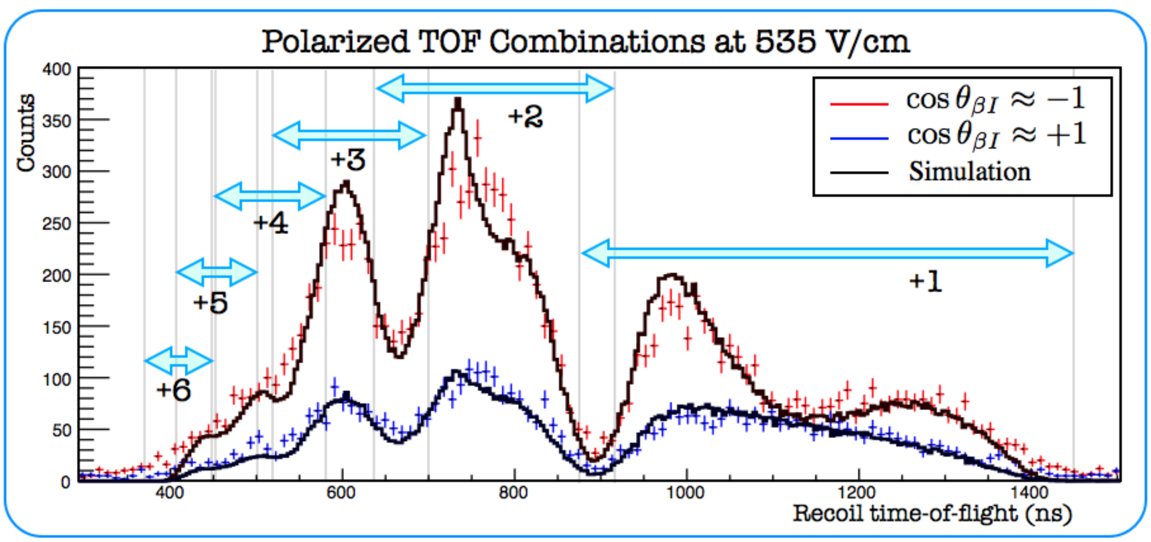

Figure 7.4: Recoil TOF Spectra for ^{37}K, taken at 535 V/cm. Recoil spectra are partially separated by charge state. For the most part, the dips within the centre of each charge state distribution are the result of the decay chamber's geometry. However, within these spectra, a non-zero R_{slow} would manifest as a change in the relative sizes of the mid-charge-state dips when comparing the red and blue spectra.

In June 2014, approximately 7 days of beam time at TRIUMF was dedicated to the TRINAT ^{37}K beta decay experiment. During this period, approximately 10,000 atoms were held within the trap at any given time. The cleaned spectra show around 50,000 polarized beta-recoil coincidence events in total, divided among measurements at three different electric field strengths (535 V/cm, 415 V/cm, 395 V/cm).

Approximately half of this data was collected with the recoil MCP in use and is therefore suitable for use in this project to search for right-handed currents; the other half is used as described within the rest of this document to search for scalar and tensor couplings.

A fit to simulation has shown that the data that has already been collected has sufficient statistical power to measure the *fractional* contribution of any polarized 'new physics' beta decay parameter (ie right-handed, scalar, and tensor currents within the weak interaction) to a sensitivity of $\sim 2\%$ of its true value. Systematic limitations are still being assessed.

7.5 Summary

This two-parameter analysis to measure A_β and b_{Fierz} has produced the results:

$$b_{\text{Fierz}} = \quad 0.033 \pm 0.084(\text{stat}) \pm 0.039(\text{sys}) \tag{7.6}$$

$$A_\beta = -0.5738 \pm 0.0082(\text{stat}) \pm 0.0041(\text{sys}), \tag{7.7}$$

where uncertainties are evaluated at 1σ. This measurement of b_{Fierz} is consistent with the standard model value of $b_{\text{Fierz}} = 0$ for the absence of scalar and tensor currents, and A_β is consistent both with the collaboration's prior measurement of A_β, as well as with the theory prediction using no exotic physics, at $A_\beta = -0.5706 \pm 0.0007$.

The result for b_{Fierz} is dominated by statistical uncertainty, suggesting that the measurement could be improved simply by counting longer. There is also room for improvement in the systematic uncertainty, which is dominated by scattering and the related measurements of material thicknesses.

Largely because of this result, the collaboration is working to reduce the largest systematics, using lower-Z materials to reduce backscattering, and changing the silicon δE to a multi-wire proportional chamber with very thin windows. The collaboration has already implemented very thin pellicle mirrors. The projected systematic uncertainty could approach 0.01 in a future experment, which would then likely continue to be limited by statistics.

Bibliography

[1] Jackson, J. D., Treiman, S. B. and Wyld, H. W., *Possible Tests of Time Reversal Invariance in Beta Decay*, Physical Review, Vol. 106, pp. 517–521, May 1957.

[2] Jackson, J. D., Treiman, S. B. and Wyld, H. W., *Coulomb Corrections in Allowed Beta Transitions*, Nuclear Physics, Vol. 4, pp. 206–212, Nov. 1957.

[3] Becquerel, H., *Sur les radiations émises par phosphorescence*, Comptes rendus de l'Academie des Sciences, Paris, Vol. 122, pp. 420–421, 1896.

[4] Rutherford, E., *VIII. Uranium radiation and the electrical conduction produced by it*, The London, Edinburgh, and Dublin Philosophical Magazine and Journal of Science, Vol. 47, No. 284, pp. 109–163, 1899.

[5] Villard, P., *Sur la réflexion et la réfraction des rayons cathodiques et des rayons déviables du radium*, CR Acad. Sci. Paris, Vol. 130, pp. 1010, 1900.

[6] Rutherford, E., *XV. The magnetic and electric deviation of the easily absorbed rays from radium*, The London, Edinburgh, and Dublin Philosophical Magazine and Journal of Science, Vol. 5, No. 26, pp. 177–187, 1903.

[7] Becquerel, H., *Influence d'un champ magnétique sur le rayonnement des corps radio-actifs*, Journal de Physique Théorique et Appliquée, Vol. 9, No. 1, pp. 71–78, 1900.

[8] Rutherford, E. and Soddy, F., *LX. radioactive change*, The London, Edinburgh, and Dublin Philosophical Magazine and Journal of Science, Vol. 5, No. 29, pp. 576–591, 1903.

[9] Brown, L. M., *The idea of the neutrino*, Physics today, Vol. 31, No. 9, pp. 23, 1978.

[10] Pais, A., *Inward Bound: Of Matter and Forces in the Physical World*, Oxford University Press, 1986.

[11] Fermi, E., *Tentativo di una Teoria Dei Raggi β*, Il Nuovo Cimento, Vol. 11, No. 1, pp. 1–19, Jan. 1934.

[12] Fermi, E., *Versuch einer Theorie der β-Strahlen. I*, Zeitschrift für Physik, Vol. 88, No. 3, pp. 161–177, 1934.

[13] Gamow, G. and Teller, E., *Selection Rules for the β-Disintegration*, Physical Review, Vol. 49, pp. 895–899, Jun 1936.

[14] Lee, T.-D. and Yang, C.-N., *Question of parity conservation in weak interactions*, Physical Review, Vol. 104, No. 1, pp. 254–258, 1956.

[15] Wu, C. S., Ambler, E., Hayward, R. W., Hoppes, D. D. and Hudson, R. P., *Experimental Test of Parity Conservation in Beta Decay*, Physical Review, Vol. 105, pp. 1413–1415, Feb 1957.

[16] Feynman, R. P. and Gell-Mann, M., *Theory of the Fermi Interaction*, Physical Review, Vol. 109, pp. 193–198, Jan 1958.

[17] Tomonaga, S.-i., *On a relativistically invariant formulation of the quantum theory of wave fields.*, Progress of Theoretical Physics, Vol. 1, No. 2, pp. 27–42, 1946.

[18] Schwinger, J., *Quantum electrodynamics. I. A covariant formulation*, Physical Review, Vol. 74, No. 10, pp. 1439, 1948.

[19] Feynman, R. P., *Space-time approach to quantum electrodynamics*, Physical Review, Vol. 76, No. 6, pp. 769, 1949.

[20] Feynman, R. P., *The theory of positrons*, Physical Review, Vol. 76, No. 6, pp. 749, 1949.

[21] Feynman, R. P., *Mathematical formulation of the quantum theory of electromagnetic interaction*, Physical Review, Vol. 80, No. 3, pp. 440, 1950.

[22] Dyson, F. J., *The radiation theories of Tomonaga, Schwinger, and Feynman*, Physical Review, Vol. 75, No. 3, pp. 486, 1949.

[23] Yang, C. N. and Mills, R. L., *Conservation of Isotopic Spin and Isotopic Gauge Invariance*, Physical Review, Vol. 96, pp. 191–195, Oct 1954.

[24] Glashow, S. L., *The renormalizability of vector meson interactions*, Nuclear Physics, Vol. 10, pp. 107–117, 1959.

[25] Glashow, S. L., *Partial-symmetries of weak interactions*, Nuclear Physics, Vol. 22, No. 4, pp. 579–588, 1961.

[26] Salam, A. and Ward, J. C., *Electromagnetic and weak interactions*, Physics Letters, Vol. 13, No. 2, pp. 168–171, 1964.

[27] Englert, F. and Brout, R., *Broken Symmetry and the Mass of Gauge Vector Mesons*, Physical Review Letters, Vol. 13, pp. 321–323, Aug 1964.

[28] Higgs, P. W., *Broken Symmetries and the Masses of Gauge Bosons*, Physical Review Letters, Vol. 13, pp. 508–509, Oct 1964.

[29] Guralnik, G. S., Hagen, C. R. and Kibble, T. W. B., *Global Conservation Laws and Massless Particles*, Physical Review Letters, Vol. 13, pp. 585–587, Nov 1964.

[30] Brout, R. and Englert, F., *Spontaneous Symmetry Breaking in Gauge Theories: a Historical Survey*, 1998.

[31] Guralnik, G. S., *The history of the Guralnik, Hagen and Kibble development of the theory of spontaneous symmetry breaking and gauge particles*, International Journal of Modern Physics A, Vol. 24, No. 14, pp. 2601–2627, 2009.

[32] Weinberg, S., *A Model of Leptons*, Physical Review Letters, Vol. 19, pp. 1264–1266, Nov 1967.

[33] Salam, A., *Elementary particle theory*, Svartholm, N. (editor), 1968.

[34] 't Hooft, G. and Veltman, M., *Regularization and renormalization of gauge fields*, Nuclear Physics B, Vol. 44, No. 1, pp. 189–213, 1972.

[35] Hasert, F. et al., *Observation of neutrino-like interactions without muon or electron in the Gargamelle neutrino experiment*, Nuclear Physics B, Vol. 73, No. 1, pp. 1–22, 1974.

[36] Arnison, G. et al., *Experimental observation of isolated large transverse energy electrons with associated missing energy at s=540 GeV*, Physics Letters B, Vol. 122, No. 1, pp. 103–116, 1983.

[37] Banner, M. et al., *Observation of single isolated electrons of high transverse momentum in events with missing transverse energy at the CERN pp collider*, Physics Letters B, Vol. 122, No. 5, pp. 476–485, 1983.

[38] Arnison, G. et al., *Experimental observation of lepton pairs of invariant mass around 95 GeV/c^2 at the CERN SPS collider*, Physics Letters B, Vol. 126, No. 5, pp. 398–410, 1983.

[39] Bagnaia, P. et al., *Evidence for $Z^0 \rightarrow e^+e^-$ at the CERN $\bar{p}p$ Collider*, Physics Letters B, Vol. 129, No. 1, pp. 130–140, 1983.

[40] Gross, D. J. and Wilczek, F., *Asymptotically free gauge theories*, Physical Review D, Vol. 8, No. 10, pp. 3633, 1973.

[41] Gross, D. J. and Wilczek, F., *Ultraviolet behavior of non-abelian gauge theories*, Physical Review Letters, Vol. 30, No. 26, pp. 1343, 1973.

[42] Politzer, H. D., *Reliable perturbative results for strong interactions?*, Physical Review Letters, Vol. 30, No. 26, pp. 1346, 1973.

[43] Pais, A. and Treiman, S. B., *How Many Charm Quantum Numbers are There?*, Physical Review Letters, Vol. 35, pp. 1556–1559, Dec 1975.

[44] Schirber, M., *Q&A: with Standard Bearer Steven Weinberg*, APS News, Vol. 28, No. 2, Feb 2019.

[45] Tanabashi, M. et al., *Review of Particle Physics*, Physical Review D, Vol. 98, pp. 030001, Aug 2018.

[46] Krane, K. S., *Introductory Nuclear Physics*, Wiley, New York, 1988.

[47] Falkowski, A., González-Alonso, M. and Naviliat-Cuncic, O., *Comprehensive analysis of beta decays within and beyond the Standard Model*, Journal of High Energy Physics, Vol. 2021, No. 4, pp. 1–36, 2021.

[48] Hong, R., Sternberg, M. G. and Garcia, A., *Helicity and nuclear β decay correlations*, American Journal of Physics, Vol. 85, No. 1, pp. 45–53, 2017.

[49] Combs, D., Jones, G., Anderson, W., Calaprice, F., Hayen, L. and Young, A., *A look into mirrors: A measurement of the β-asymmetry in ^{19}Ne decay and searches for new physics*, arXiv e-prints, p. arXiv:2009.13700, Sep. 2020.

[50] González-Alonso, M., Naviliat-Cuncic, O. and Severijns, N., *New physics searches in nuclear and neutron β decay*, Progress in Particle and Nuclear Physics, Vol. 104, pp. 165–223, 2019.

[51] Cirgiliano, V., Garcia, A., Gazit, D., Naviliat-Cuncic, O., Savard, G. and Young, A., *Precision beta decay as a probe of new physics*, arXiv preprint arXiv:1907.02164, 2019.

[52] Ge, S.-F., Lindner, M. and Patra, S., *New physics effects on neutrinoless double beta decay from right-handed current*, Journal of High Energy Physics, Vol. 2015, No. 10, pp. 1–18, 2015.

[53] Ali, A., Borisov, A. V. and Zhuridov, D., *Probing new physics in the neutrinoless double beta decay using electron angular correlation*, Physical Review D, Vol. 76, No. 9, pp. 093009, 2007.

[54] Klapdor-Kleingrothaus, H., *Status and Perspectives of Double Beta Decay—Window to New Physics Beyond the Standard Model of Particle Physics*, International Journal of Modern Physics A, Vol. 13, No. 23, pp. 3953–3992, 1998.

[55] Langacker, P., Luo, M. and Mann, A. K., *High-precision electroweak experiments: a global search for new physics beyond the Standard Model*, Reviews of Modern Physics, Vol. 64, No. 1, pp. 87, 1992.

[56] Cameron, J., Chen, J., Singh, B. and Nica, N., *Nuclear data sheets for A= 37*, Nuclear Data Sheets, Vol. 113, No. 2, pp. 365–514, 2012.

[57] Shidling, P. D., Melconian, D., Behling, S., Fenker, B., Hardy, J. C., Iacob, V. E., McCleskey, E., McCleskey, M., Mehlman, M., Park, H. I. and Roeder,

B. T., *Precision half-life measurement of the β^+ decay of ^{37}K*, Physical Review C, Vol. 90, pp. 032501, Sep 2014.

[58] Ozmetin, A., Melconian, D. G., Iacob, V. E., Shidling, P., Kolhinen, V. S., McClain, D. J., Nasser, M., Schroeder, B., Roeder, B., Park, H.-I., Anholm, M., Saastamoinen, A. J. and Trinat Collaboration, *Improving the ft value of 37K via a precision measurement of the branching ratio*, *APS Division of Nuclear Physics Meeting Abstracts*, Oct 2020.

[59] Ebel, M. and Feldman, G., *Further remarks on Coulomb corrections in allowed beta transitions*, Nuclear Physics, Vol. 4, pp. 213–214, 1957.

[60] Greiner, W. and Müller, B., *Leptonic Interactions*, pp. 25–80, Springer Berlin Heidelberg, Berlin, Heidelberg, 2009.

[61] Holstein, B. R., *Recoil effects in allowed beta decay: The elementary particle approach*, Reviews of Modern Physics, Vol. 46, No. 4, pp. 789–814, Oct. 1974.

[62] Pattie, R. J. et al., *First Measurement of the Neutron β Asymmetry with Ultracold Neutrons*, Physical Review Letters, Vol. 102, pp. 012301, Jan 2009.

[63] Fenker, B., Gorelov, A., Melconian, D., Behr, J. A., Anholm, M., Ashery, D., Behling, R. S., Cohen, I., Craiciu, I., Gwinner, G., McNeil, J., Mehlman, M., Olchanski, K., Shidling, P. D., Smale, S. and Warner, C. L., *Precision Measurement of the β Asymmetry in Spin-Polarized ^{37}K Decay*, Physical Review Letters, Vol. 120, pp. 062502, Feb 2018.

[64] Sun, X. et al., *Improved limits on Fierz interference using asymmetry measurements from the Ultracold Neutron Asymmetry (UCNA) experiment*, Physical Review C, Vol. 101, pp. 035503, Mar 2020.

[65] Saul, H., Roick, C., Abele, H., Mest, H., Klopf, M., Petukhov, A. K., Soldner, T., Wang, X., Werder, D. and Märkisch, B., *Limit on the Fierz Interference Term b from a Measurement of the Beta Asymmetry in Neutron Decay*, Physical Review Letters, Vol. 125, pp. 112501, Sep 2020.

[66] Hickerson, K. P. et al., *First direct constraints on Fierz interference in free-neutron β decay*, Physical Review C, Vol. 96, pp. 042501, Oct 2017.

[67] Melconian, D., Behr, J., Ashery, D., Aviv, O., Bricault, P., Dombsky, M., Fostner, S., Gorelov, A., Gu, S., Hanemaayer, V., Jackson, K., Pearson, M. and Vollrath, I., *Measurement of the neutrino asymmetry in the β decay of laser-cooled, polarized 37K*, Physics Letters B, Vol. 649, No. 5, pp. 370–375, 2007.

[68] Towner, I. and Hardy, J., *Currents and their couplings in the weak sector of the standard model*, Symmetries and fundamental interactions in nuclei, p. 183, 1995.

[69] Hardy, J. C. and Towner, I., *Superallowed $0^+ \to 0^+$ nuclear β decays: A critical survey with tests of the conserved vector current hypothesis and the standard model*, Physical Review C, Vol. 71, No. 5, pp. 055501, 2005.

[70] Wilkinson, D., *Evaluation of beta-decay: II. Finite mass and size effects*, Nuclear Instruments and Methods in Physics Research Section A: Accelerators, Spectrometers, Detectors and Associated Equipment, Vol. 290, No. 2, pp. 509–515, 1990.

[71] Wilkinson, D., *Evaluation of beta-decay Part III. The complex gamma function*, Nuclear Instruments and Methods in Physics Research Section A: Accelerators, Spectrometers, Detectors and Associated Equipment, Vol. 335, No. 1, pp. 305–309, 1993.

[72] Wilkinson, D., *Evaluation of beta-decay Part IV. The complex gamma function; practicalities*, Nuclear Instruments and Methods in Physics Research Section A: Accelerators, Spectrometers, Detectors and Associated Equipment, Vol. 365, No. 1, pp. 203–207, 1995.

[73] Severijns, N., Tandecki, M., Phalet, T. and Towner, I. S., *$\mathcal{F}t$ values of the $T = 1/2$ mirror β transitions*, Physical Review C, Vol. 78, pp. 055501, Nov 2008.

[74] Towner, I. S. and Hardy, J. C., *Improved calculation of the isospin-symmetry-breaking corrections to superallowed Fermi β decay*, Physical Review C, Vol. 77, pp. 025501, Feb 2008.

[75] Jaus, W. and Rasche, G., *Nuclear-structure dependence of $O(\alpha)$ corrections to Fermi decays and the value of the Kobayashi-Maskawa matrix element* V_{ud}, Physical Review D, Vol. 41, pp. 166–176, Jan 1990.

[76] Barker, F., Brown, B., Jaus, W. and Rasche, G., *Determination of $|V_{ud}|$ from Fermi decays and the unitarity of the KM-mixing matrix*, Nuclear Physics A, Vol. 540, No. 3, pp. 501–519, 1992.

[77] Towner, I., *The nuclear-structure dependence of radiative corrections in superallowed Fermi beta-decay*, Nuclear Physics A, Vol. 540, No. 3, pp. 478–500, 1992.

[78] Towner, I., *Quenching of spin operators in the calculation of radiative corrections for nuclear beta decay*, Physics Letters B, Vol. 333, No. 1, pp. 13–16, 1994.

[79] Marciano, W. J. and Sirlin, A., *Radiative corrections to β decay and the possibility of a fourth generation*, Physical Review Letters, Vol. 56, pp. 22–25, Jan 1986.

[80] Marciano, W. J. and Sirlin, A., *Improved Calculation of Electroweak Radiative Corrections and the Value of V_{ud}*, Physical Review Letters, Vol. 96, pp. 032002, Jan 2006.

[81] Czarnecki, A., Marciano, W. J. and Sirlin, A., *Radiative corrections to neutron and nuclear beta decays revisited*, Physical Review D, Vol. 100, pp. 073008, Oct 2019.

[82] Hayen, L., *Standard model $\mathcal{O}(\alpha)$ renormalization of g_A and its impact on new physics searches*, Phys. Rev. D, Vol. 103, pp. 113001, Jun 2021.

[83] Hardy, J. C. and Towner, I. S., *Superallowed $0^+ \rightarrow 0^+$ nuclear β decays: 2020 critical survey, with implications for V_{ud} and CKM unitarity*, Physical Review C, Vol. 102, pp. 045501, Oct 2020.

[84] Severijns, N., Beck, M. and Naviliat-Cuncic, O., *Tests of the standard electroweak model in nuclear beta decay*, Reviews of Modern Physics, Vol. 78, pp. 991–1040, September 2006.

[85] Hayen, L. and Severijns, N., *Radiative corrections to Gamow-Teller decays*, arXiv preprint arXiv:1906.09870, p. arXiv:1906.09870, Jun. 2019.

[86] Ben-Itzhak, I., Heber, O., Gertner, I. and Rosner, B., *Production and mean-lifetime measurement of metastable Ar^- ions*, Physical Review A, Vol. 38, pp. 4870–4871, Nov 1988.

[87] Levinger, J. S., *Effects of Radioactive Disintegrations on Inner Electrons of the Atom*, Physical Review, Vol. 90, pp. 11–25, Apr 1953.

[88] Corney, A., *Atomic and Laser Spectroscopy*, Oxford University Press, New York, 1977.

[89] Fenker, B., Behr, J. A., Melconian, D., Anderson, R. M. A., Anholm, M., Ashery, D., Behling, R. S., Cohen, I., Craiciu, I., Donohue, J. M., Farfan, C., Friesen, D., Gorelov, A., McNeil, J., Mehlman, M., Norton, H., Olchanski, K., Smale, S., Thériault, O., Vantyghem, A. N. and Warner, C. L., *Precision measurement of the nuclear polarization in laser-cooled, optically pumped ^{37}K*, New Journal of Physics, Vol. 18, No. 7, pp. 073028, 2016.

[90] Raab, E. L., Prentiss, M., Cable, A., Chu, S. and Pritchard, D. E., *Trapping of Neutral Sodium Atoms with Radiation Pressure*, Physical Review Letters, Vol. 59, pp. 2631–2634, Dec 1987.

[91] Anholm, M., *Characterizing the AC-MOT*, Master's thesis, University of British Columbia, 2014.

[92] Harvey, M. and Murray, A. J., *Cold Atom Trap with Zero Residual Magnetic Field: The AC Magneto-Optical Trap*, Physical Review Letters, Vol. 101, pp. 173201, Oct 2008.

[93] Gorelov, A., Behr, J., Melconian, D., Trinczek, M., Dubé, P., Häusser, O., Giesen, U., Jackson, K., Swanson, T., D'Auria, J., Dombsky, M., Ball, G., Buchmann, L., Jennings, B., Dilling, J., Schmid, J., Ashery, D., Deutsch, J., Alford, W., Asgeirsson, D., Wong, W. and Lee, B., *Beta–neutrino correlation experiments on laser trapped ^{38m}K, ^{37}K*, Hyperfine Interactions, Vol. 127, No. 1, pp. 373–380, 2000.

[94] Swanson, T. B., Asgeirsson, D., Behr, J. A., Gorelov, A. and Melconian, D., *Efficient transfer in a double magneto-optical trap system*, Journal of the Optical Society of America B, Vol. 15, No. 11, pp. 2641–2645, Nov 1998.

[95] Audi, G., Wapstra, A. and Thibault, C., *The AME2003 Atomic Mass Evaluation*, Nuclear Physics A, Vol. 729, No. 1, pp. 337 – 676, 2003.

[96] Fenker, B. B., *Precise measurement of the β-asymmetry in the decay of magneto-optically trapped, spin-polarized 37K*, Ph.D. thesis, Texas A&M University, 2016.

[97] Behling, R. S., *Measurement of the Standard Model Beta Asymmetry Parameter, A_β, in 37K*, Ph.D. thesis, Texas A&M University, 2015.

[98] Clifford, E., Hagberg, E., Koslowsy, V., Hardy, J., Schmeing, H. and Azuma, R., *Measurements of the response of a hybrid detector telescope to mono-energetic beams of positrons and electrons in the energy range 0.8–3.8 MeV*, Nuclear Instruments and Methods in Physics Research, Vol. 224, No. 3, pp. 440–447, 1984.

[99] Landau, L. D., *On the energy loss of fast particles by ionization*, J. Phys., Vol. 8, pp. 201–205, 1944.

[100] Moyal, J., *XXX. Theory of ionization fluctuations*, The London, Edinburgh, and Dublin Philosophical Magazine and Journal of Science, Vol. 46, No. 374, pp. 263–280, 1955.

[101] Lonergan, J., Jupiter, C. and Merkel, G., *Electron energy straggling measurements for thick targets of beryllium, aluminum, and gold at 4.0 and 8.0 MeV*, Journal of Applied Physics, Vol. 41, No. 2, pp. 678–688, 1970.

[102] Rester, D. H. and Derrickson, J. H., *Electron Transmission Measurements for Al, Sn, and Au Targets at Electron Bombarding Energies of 1.0 and 2.5 MeV*, Journal of Applied Physics, Vol. 42, No. 2, pp. 714–721, 1971.

[103] Brown, M. A.-P. et al., *New result for the neutron β-asymmetry parameter A_0 from UCNA*, Physical Review C, Vol. 97, pp. 035505, Mar 2018.

[104] Severijns, N. and Naviliat-Cuncic, O., *Symmetry tests in nuclear beta decay*, Annual Review of Nuclear and Particle Science, Vol. 61, pp. 23–46, 2011.

[105] Melconian, D. G., *Measurement of the Neutrino Asymmetry in the Beta Decay of Laser-Cooled, Polarized* ^{37}K, Ph.D. thesis, Simon Fraser University, 2005.

[106] Holstein, B. R., *Erratum: Recoil effects in allowed beta decay: The elementary particle approach*, Reviews of Modern Physics, Vol. 48, pp. 673–673, Oct 1976.

[107] Towner, I., Private Communication to the TRINAT Collaboration, August 2011.

[108] Ball, G. C., *Tests of the standard model from nuclear beta-decay studies at ISAC*, *From Particles To The Universe*, pp. 148–153, World Scientific, 2001.

[109] Raman, S., Houser, C., Walkiewicz, T. and Towner, I., *Mixed Fermi and Gamow-Teller* β*-transitions and isoscalar magnetic moments*, Atomic Data and Nuclear Data Tables, Vol. 21, No. 6, pp. 567–620, 1978.

Appendix A

Statement of Contributions

Much of the experimental apparatus described here was designed and built before I joined the TRINAT research group, with the notable exception of the AC-MOT, which I played a key part in designing and implementing as part of a previous MSc degree[91], as well as afterwards. This includes time-independent magnetic field trimming, time-dependent control and optimization of the anti-Helmholtz coils for all parts of the AC-MOT/OP duty cycle with the development of custom waveforms, logic controls for the trapping and optical pumping lasers to maintain synchronization with the magnetic field, and related logic triggers to be recorded in data acquisition.

Calibration of the rMCP and subsequent measurements of the atom cloud position were performed by me. Calibration of the eMCP, the two scintillators, and the DSSDs for the relevant experimental data was performed primarily by Ben Fenker. The switch to using the leading rather than trailing edge for all timing data was implemented by me. The scintillator walk correction was also performed by me.

Upgrades to the TRINAT Geant4 software package to enable multithreading and reconcile the JTW and Holstein approaches (see Appendix C) to allow for scalar and tensor couplings within the main branch decay probability distribution were performed by me. The implementation of the simulation's 2% branch without exotic couplings, which was used for this analysis, had been completed earlier by other collaboration members. The simulation's representation of the materials and geometry used for our experimental chamber had already been set up by Spencer Behling and Ben Fenker. Ben Fenker also set up the simulated DSSD calibration such that each simulated strip had the same resolution and noise as the real strip that it represented.

The simple monte carlo and associated response functions were created, optimized, and tested by me, and I was responsible for overseeing the Geant4 and simple monte carlo simulation runs.

The SOE TOF simulations in COMSOL were performed by Alexandre Gorelov, but the event-by-event combination of G4 and COMSOL spectra, their normalizations, and all further work with the simulated data was performed by me. I was also responsible for checking that the TOF model of background events arising from the combination of COMSOL and Geant4 simulations performed as expected.

I was responsible for setting up the comparisons between experimental data and the parameter space of simulated A_β and b_{Fierz} values. The systematic effects listed in Table 7.1 were all evaluated with me, with the exception of the low energy tail entry, which was evaluated by John Behr. Additionally, although the final value of the beta scattering uncertainty was evaluated by me, its value as a fraction of total events at certain angles was agreed upon by the collaboration as a whole after much discussion, in advance of the acceptance for publication of our previous A_β measurement with the same data [63], and I have attempted to maintain a consistent approach in that regard.

The final values of the b_{Fierz} and A_β measurements presented here, and the uncertainties associated with them, were evaluated by me.

I was also responsible for the collaboration's *post hoc* discovery that the previous A_β measurement had been performed using partially polarized data, and estimating the size of the effect to A_β.

Appendix B

Notable Differences in Data Selection between this and the Previous Result

B.1 Polarization Cycle Selection

Data used for our collaboration's Ref. [63] was slightly less polarized than previously thought, due to an oversight in the data selection procedure. See Ch. 7.2 for a discussion of the effects.

B.2 Leading Edge / Trailing Edge and Walk Correction

Using the leading edge rather than the trailing edge to mark the timing of time-to-digital converter (TDC) pulses cleans up jitter, eliminates background, and changes the relative delays between different inputs. It is immediately relevant to the shape of the 'walk correction' on scintillator timing pulses, which give a different prediction for beta arrival time as a function of scintillator energy.

B.3 TOF Cut + Background Modelling

A SOE-beta time-of-flight cut is necessary to reduce background. The above mentioned walk correction directly results in an change in which specific events are selected in a given TOF cut. It further results in an adjustment to the expected fraction of background events in any such cut.

B.4 DSSD Energy Threshold

I use an overall 50 keV threshold on the DSSD, (taking +/- 10 keV from that as a systematic to be propagated/checked), but the collaboration's previous analysis used 60 keV as the default threshold.

Appendix C

Derivation of the Probability Density Function

In order to obtain a probability density function (PDF) to describe the beta decay process which includes both a representation of the exotic physics that is the subject of this search, as well as the small higher-order corrections which are known to be present, it is necessary to combine features from two disparate formalisms. The Jackson–Treiman–Wyld (JTW) description incorporates many parameters representing various flavours of exotic physics, but incorporates only the leading order terms in the resulting expression. By contrast, the Holstein formulation makes no reference to exotic physics, but does a much more thorough job of describing the beta decay physics that we collectively do expect to see, such as higher-order terms and small corrections to the form of the spectra.

Although recoil-order and other small corrections must be accounted for within a complete description of beta decay, in the case of exotic couplings, leading order JTW description is adequate, because any exotic couplings present in nature have already been determined to be either small or nonexistant. Therefore, in a search for exotic physics of this nature, it is sufficient to describe any exotic coupling parameters with expressions truncated at leading order, in combination with a more precise set of expressions to account for the well-understood physical behaviours that dominate.

We begin by recalling the Fermi contact interaction description of beta decay from

Eq. (1.4). Recalling the definition of an interaction Hamiltonian, we can write:

$$\mathcal{M}_{fi} \;=\; G_F \int \bar{\psi}_f \, \hat{\mathcal{O}} \, \psi_i \, \mathrm{d}V. \;=\; \int \mathcal{H}_{\text{int}} \, \mathrm{d}V \tag{C.1}$$

This approximation is adequate for the purpose of characterizing BSM interactions because any exotic physics that we might search for has already been constrained, through decades of clever experiments, to be a comparatively small part of the overall behaviour. These small adjustments to already small terms may be safely neglected. This model leads directly to the JTW result described in Sec. C.1, however the Holstein results of Sec. C.2 arise from a more modern description of the beta decay process.

We will use the Lee-Hang interaction Hamiltonian here, which incorporates a linear combination of all possible operators that obey Lorentz invariance at the nucleon level. In particular[14]:

$$\begin{aligned}
\mathcal{H}_{\text{int}} \,/\, G_F \;=\;& (\bar{\psi}_p \psi_n)(C_S \, \bar{\psi}_e \psi_\nu + C'_S \, \bar{\psi}_e \gamma_5 \psi_\nu) \\
&+ (\bar{\psi}_p \gamma_\mu \psi_n)(C_V \, \bar{\psi}_e \gamma_\mu \psi_\nu + C'_V \, \bar{\psi}_e \gamma_\mu \gamma_5 \psi_\nu) \\
&+ \frac{1}{2}(\bar{\psi}_p \sigma_{\lambda\mu} \psi_n)(C_T \, \bar{\psi}_e \sigma_{\lambda\mu} \psi_\nu + C'_T \, \bar{\psi}_e \sigma_{\lambda\mu} \gamma_5 \psi_\nu) \\
&- (\bar{\psi}_p \gamma_\mu \gamma_5 \psi_n)(C_A \, \bar{\psi}_e \gamma_\mu \gamma_5 \psi_\nu + C'_A \, \bar{\psi}_e \gamma_\mu \psi_\nu) \\
&+ (\bar{\psi}_p \gamma_5 \psi_n)(C_P \, \bar{\psi}_e \gamma_5 \psi_\nu + C'_P \, \bar{\psi}_e \psi_\nu) + \text{H.C.},
\end{aligned} \tag{C.2}$$

where C_X and C'_X (with $X = \{V, A, S, T, P\}$) are complex coupling constants for vector, axial, scalar, tensor, and pseudoscalar interactions, and ψ_Y (with $Y = \{p, n, e, \nu\}$) are the wavefunctions for the interaction's proton, neutron, electron, and neutrino. Operators γ_5 and γ_μ are Dirac gamma matrices, and $\sigma_{\lambda\mu} = -\frac{i}{2}(\gamma_\lambda \gamma_\mu - \gamma_\mu \gamma_\lambda)$. As usual, "H.C." represents the Hermitian conjugate of the previous terms within the Hamiltonian.

With these expressions in place, it is possible to obtain a complete solution for the differential decay rate of Eq. 1.6 in terms of physical observables.

C.1 JTW Formalism

Rather than going through the full calculation to find the differential decay rate, I will instead simply give the result, taken from JTW and others[14][1][2][59]. To leading order, we find a five-dimensional PDF for beta decay kinematics:

$$\begin{aligned}
\mathrm{d}^5\Gamma_{\mathrm{JTW}} \;\equiv\; & \frac{1}{(2\pi)^5} F_{\pm}(Z', E_\beta) p_\beta E_\beta (E_0 - E_\beta)^2 \mathrm{d}E_\beta \, \mathrm{d}^2\hat{\boldsymbol{\Omega}}_\beta \, \mathrm{d}^2\hat{\boldsymbol{\Omega}}_\nu \\
& \times \xi \left[1 + a_{\beta\nu} \frac{\vec{\boldsymbol{p}}_\beta \cdot \vec{\boldsymbol{p}}_\nu}{E_\beta E_\nu} + b_{\mathrm{Fierz}} \frac{m_e c^2}{E_\beta} + \; c_{\mathrm{align}} \; T_{\mathrm{align}}(\vec{\boldsymbol{J}}) \left(\frac{\vec{\boldsymbol{p}}_\beta \cdot \vec{\boldsymbol{p}}_\nu}{3E_\beta E_\nu} - \frac{(\vec{\boldsymbol{p}}_\beta \cdot \hat{\boldsymbol{j}})(\vec{\boldsymbol{p}}_\nu \cdot \hat{\boldsymbol{j}})}{E_\beta E_\nu} \right) \right. \\
& \left. + \frac{\vec{\boldsymbol{J}}}{J} \cdot \left(A_\beta \frac{\vec{\boldsymbol{p}}_\beta}{E_\beta} + B_\nu \frac{\vec{\boldsymbol{p}}_\nu}{E_\nu} + D_{\mathrm{TR}} \frac{\vec{\boldsymbol{p}}_\beta \times \vec{\boldsymbol{p}}_\nu}{E_\beta E_\nu} \right) \right], \qquad \text{(C.3)}
\end{aligned}$$

where, for convenience, we have defined a nuclear alignment term,

$$T_{\mathrm{align}}(\vec{\boldsymbol{J}}) \;\equiv\; \frac{J(J+1) - 3\langle(\vec{\boldsymbol{J}} \cdot \hat{\boldsymbol{j}})^2\rangle}{J(2J-1)}. \qquad \text{(C.4)}$$

In Eqs. (C.3) and (C.4), E_β, $\vec{\boldsymbol{p}}_\beta$, and p_β are the outgoing β particle's (total) energy, momentum 3-vector, and momentum scalar, while E_ν, $\vec{\boldsymbol{p}}_\nu$, and p_ν are the equivalent quantities for the outgoing (anti-)neutrino, and E_0 is the maximum possible β energy associated with the transition. $\vec{\boldsymbol{J}}$ is the nuclear angular momentum vector of the parent, and J is its projection onto the axis of quantization. $\hat{\boldsymbol{j}}$ is a unit vector in the direction of $\vec{\boldsymbol{J}}$ (note that in general, $\hat{\boldsymbol{j}} \neq \frac{\vec{\boldsymbol{J}}}{J}$). As usual, m_e is the mass of the electron, and c is the speed of light. The infinitesimal surface element $\mathrm{d}^2\hat{\boldsymbol{\Omega}}_\beta$ ($\mathrm{d}^2\hat{\boldsymbol{\Omega}}_\nu$) represents the direction of β (neutrino) emission. The function $F_{\pm}(Z', E_\beta)$ is known as a Fermi function for outgoing electrons (top) and positrons (bottom), with Z' the proton number of the daughter nucleus, and is evaluated as in e.g. Refs. [70][71][72].

For the reader's convenience, the kinematic factors unique to a particular transition are written out here in terms of their couplings.

$$\begin{aligned}
\xi &= |M_F|^2\big(|C_S|^2 + |C_V|^2 + |C'_S|^2 + |C'_V|^2\big) \\
&+ \ |M_{GT}|^2 \left(|C_T|^2 + |C_A|^2 + |C'_T|^2 + |C'_A|^2\right) \qquad \text{(C.5)} \\
a_{\beta\nu}\xi &= |M_F|^2\left[\left(|C_V|^2 + |C'_V|^2 - |C_S|^2 - |C'_S|^2\right) \mp 2\frac{\alpha Z m_e c^2}{p_\beta c}\,\mathrm{Im}[C_S C_V^* + C'_S C'^*_V]\right] \\
&+ \ \frac{1}{3}\,|M_{GT}|^2\left[\left(|C_T|^2 - |C_A|^2 + |C'_T|^2 - |C'_A|^2\right)\right. \\
&\left.\pm\, 2\frac{\alpha Z m_e c^2}{p_\beta c}\,\mathrm{Im}[C_T C_A^* + C'_T C'^*_A]\right] \qquad \text{(C.6)} \\
b_{\text{Fierz}}\,\xi &= \pm\, 2\gamma\,\mathrm{Re}\big[|M_F|^2\,(C_S C_V^* + C'_S C'^*_V) + |M_{GT}|^2\,(C_T C_A^* + C'_T C'^*_A)\big] \qquad \text{(C.7)} \\
c_{\text{align}}\,\xi &= |M_{GT}|^2\Lambda_{J'J}\left[\left(|C_T|^2 - |C_A|^2 + |C'_T|^2 - |C'_A|^2\right) \pm 2\frac{\alpha Z m_e c^2}{p_\beta c}\,\mathrm{Im}[C_T C_A^* + C'_T C'^*_A]\right] \qquad \text{(C.8)}
\end{aligned}$$

$$\begin{aligned}
A_\beta\,\xi &= 2\,\lambda_{J'J}|M_{GT}|^2\left[\pm\mathrm{Re}[C_T C'^*_T - C_A C'^*_A] + \frac{\alpha Z m_e c^2}{p_\beta c}\,\mathrm{Im}[C_T C'^*_A + C'_T C^*_A]\right] \\
&+ \ 2\,\delta_{J'J}\,M_F\,M_{GT}\left(\frac{J}{J+1}\right)^{1/2}\left[\ \mathrm{Re}[C_S C'^*_T + C'_S C^*_T - C_V C'^*_A - C'_V C^*_A]\right. \\
&\left.\pm\ 2\frac{\alpha Z m_e c^2}{p_\beta c}\,\mathrm{Im}[C_S C'^*_A + C'_S C^*_A - C_V C'^*_T - C'_V C^*_T]\right] \qquad \text{(C.9)} \\
B_\nu\xi &= 2|M_{GT}|^2\lambda_{J'J}\,\mathrm{Re}\left[\frac{\gamma\, m_e c^2}{E_\beta}\,(C_T C'^*_A + C'_T C^*_A) \pm (C_T C'^*_T + C_A C'^*_A)\right] \\
&- \ \delta_{J'J}\,M_F\,M_{GT}\left(\frac{J}{J+1}\right)^{1/2}\mathrm{Re}\left[(C_S C'^*_T + C'_S C^*_T + C_V C'^*_A + C'_V C^*_A)\right. \\
&\left.\pm\ \frac{\gamma\, m_e c^2}{E_\beta}\,(C_S C'^*_A + C'_S C^*_A + C_V C'^*_T + C'_V C^*_T)\right] \qquad \text{(C.10)} \\
D_{\text{TR}}\xi &= 2\,\delta_{J'J}\,M_F\,M_{GT}\left(\frac{J}{J+1}\right)^{1/2}\left[\ \mathrm{Im}[C_S C^*_T - C_V C^*_A + C'_S C'^*_T - C'_V C'^*_A]\right. \\
&\left.\mp\ \ \frac{\alpha Z m_e c^2}{p_\beta c}\,\mathrm{Re}[C_S C^*_A - C_V C^*_T + C'_S C'^*_A - C'_V C'^*_T]\right] \qquad \text{(C.11)}
\end{aligned}$$

In Eqs. C.5 - C.11, we have used $\gamma := (1-\alpha^2 Z'^2)^{1/2}$, and as usual, α is the fine structure constant. Here, M_F and M_{GT} are the Fermi and Gamow-Teller matrix elements, and are unique to the transition under consideration, while the C_X and C'_X

(for $X = \{V, A, S, T\}$) are as in Eq. (C.2). The possible pseudoscalar couplings (C_P and C'_P) have been dropped here because they are relativisitically suppressed. We have also made use of the following shorthand definitions of $\lambda_{J'J}$, $\Lambda_{J'J}$, and $\delta_{J'J}$ for transitions with parent and daughter nuclear angular momenta given by J and J' respectively:

$$\lambda_{J'J} = \begin{cases} 1 & J' = J - 1 \\ \frac{1}{J+1} & J' = J \\ \frac{-J}{J+1} & J' = J + 1 \end{cases} \tag{C.12}$$

$$\Lambda_{J'J} = \begin{cases} 1 & J' = J - 1 \\ \frac{-(2J-1)}{J+1} & J' = J \\ \frac{J(2J-1)}{(J+1)(2J-3)} & J' = J + 1 \end{cases} \tag{C.13}$$

$$\delta_{J'J} = \begin{cases} 1 & J' = J \\ 0 & J' \neq J \end{cases} \tag{C.14}$$

Note that Eq. C.3 depends on neutrino momentum, which we cannot observe directly; to make use of the neutrino momentum, it must first be reconstructed from the momenta of the outgoing beta and daughter nucleus. From an experimental standpoint, within the present experiment we it is not possible to reconstruct the the neutrino momenta with the available data, because we failed to measure the momenta of the daughters in conjunction with the tagged beta decay events with which we are primarily concerned in this thesis, so there is insufficient kinematic information available.

From a theoretical standpoint, JTW has intentionally neglected recoil-order terms – meaning that the daughter nucleus is treated, for the purpose of kinetic energy calculations, as being infinitely massive, and as such it must have no change in kinetic energy from the decay–however the approximation still allows for it to undergo a change in momentum. One result of this approximation is that the neutrino energy, E_ν, is not a free variable within Eq. C.3, since the total amount of energy released is fixed for a given transition. The inherent inconsistencies of this approximation make it a tricky starting point for a description of neutrino and recoil kinematics.

It is fortunately possible to simplify Eq. (C.3) by integrating over all possible neutrino directions such that the resulting distribution no longer depends on parameters that are not observed. The result is:

$$\begin{aligned} \mathrm{d}^3\Gamma &= \frac{2}{(2\pi)^4} F_{\pm}(Z', E_\beta)\, p_\beta E_\beta (E_0 - E_\beta)^2\, \mathrm{d}E_\beta\, \mathrm{d}^2\hat{\boldsymbol{\Omega}}_\beta\, \xi \\ &\quad \times \left[1 + b_{\mathrm{Fierz}} \frac{m_e c^2}{E_\beta} + A_\beta \left(\frac{\vec{\boldsymbol{J}}}{J} \cdot \frac{\vec{\boldsymbol{p}}_\beta}{E_\beta}\right)\right]. \end{aligned} \tag{C.15}$$

By choosing the coordinate system describing the outgoing β-direction to be aligned with the nuclear spin direction ($\vec{\boldsymbol{J}}$), it can be seen that any azimuthal dependence has been eliminated with the integral over neutrino direction. Then, a further integral over the ϕ_β coordinate yields the result:

$$\mathrm{d}^2\Gamma(E_\beta, \theta) = W(E_\beta) \left[1 + b_{\mathrm{Fierz}} \frac{m_e c^2}{E_\beta} + A_\beta \frac{v_\beta(E_\beta)}{c} |\vec{\boldsymbol{P}}| \cos\theta\right] \mathrm{d}E_\beta\, \mathrm{d}\theta, \tag{C.16}$$

where the polarization $\vec{\boldsymbol{P}}$ is given by $\vec{\boldsymbol{P}} := \frac{\vec{\boldsymbol{J}}}{J}$, and θ is the angle between the beta emission direction and the polarization direction. Here, we have grouped the expression's overall energy dependence into the term $W(E_\beta)$, so that

$$W(E_\beta) = \frac{2}{(2\pi)^3} F_{-}(Z', E_\beta)\, \xi\, p_\beta E_\beta (E_0 - E_\beta)^2, \tag{C.17}$$

where we have taken the opportunity to specialize the equations to β^+ decay transitions with $J = J' = \frac{3}{2}$. The remaining parameters can be simplified as:

$$
\begin{aligned}
\xi &= |M_F|^2 \left(|C_S|^2 + |C_V|^2 + |C_S'|^2 + |C_V'|^2\right) \\
&\quad + \, |M_{GT}|^2 \left(|C_T|^2 + |C_A|^2 + |C_T'|^2 + |C_A'|^2\right) \qquad \text{(C.18)} \\
b_{\text{Fierz}}\, \xi &= -\, 2\gamma \,\text{Re}\big[|M_F|^2 \left(C_S C_V^* + C_S' C_V'^*\right) + |M_{GT}|^2 \left(C_T C_A^* + C_T' C_A'^*\right)\big] \\
& \qquad \text{(C.19)} \\
A_\beta\, \xi &= \frac{4}{5}\, |M_{GT}|^2 \left[\text{Re}[C_A C_A'^* - C_T C_T'^*] + \frac{\alpha Z m_e c^2}{p_\beta c}\, \text{Im}[C_T C_A'^* + C_T' C_A^*]\right] \\
&\quad + \, 2 \left(\frac{3}{5}\right)^{1/2} M_F\, M_{GT} \Big[\text{Re}[C_S C_T'^* + C_S' C_T^* - C_V C_A'^* - C_V' C_A^*] \\
&\quad - \, \frac{\alpha Z' m_e c^2}{p_\beta c}\, \text{Im}[C_S C_A'^* + C_S' C_A^* - C_V C_T'^* - C_V' C_T^*]\Big]\,. \qquad \text{(C.20)}
\end{aligned}
$$

It is clear that the results of Eqs. (C.16)-(C.20) present a significant simplification over the description of Eqs. (C.3)-(C.14).

Note that JTW presents slightly different expressions for one component of A_β within [1] and [2], and the latter convention is what has been adopted here. We further require that both M_F and M_{GT} must be real, however we do not require that they be positive, which would make the two conventions equivalent.

There are a number of degrees of freedom left in the expressions that remain, and it is not immediately obvious how certain choices about these parameters might affect the physical results, or which approximations or assumptions ought to be made in order to arrive at a theory that matches the observational reality. This is in part a result of the fact that the theory behind JTW was developed before we had a detailed experimental understanding of much of the behaviour of beta decay, so all mathematically consistent behaviours are treated with roughly the same amount of consideration within the model.

Perhaps the most notable improvement to our understanding of Eqs. (C.15)-(C.20) is that the weak interaction arises predominantly from vector (C_V, C_V') and axial-vector (C_A, C_A') couplings, and the scalar and tensor couplings, if present at all, are comparatively small. In particular,

$$\frac{|C_S|^2 + |C'_S|^2}{|C_V|^2 + |C'_V|^2} \ll 1 \tag{C.21}$$

$$\frac{|C_T|^2 + |C'_T|^2}{|C_A|^2 + |C'_A|^2} \ll 1. \tag{C.22}$$

Imaginary components of C_X and C'_X are associated with breaking of time-reversal symmetry for the transition. Since this effect has never been observed, it must be comparatively small if it is present, and so it follows that

$$\left|\frac{\mathrm{Im}[C_X]}{\mathrm{Re}[C_X]}\right| \ll 1 \tag{C.23}$$

$$\left|\frac{\mathrm{Im}[C'_X]}{\mathrm{Re}[C'_X]}\right| \ll 1, \tag{C.24}$$

which holds *at least* for the cases of $X = \{V, A\}$, as there is comparatively little experimental information on how scalar and tensor interactions might behave with regard to time reversal, for the obvious reason that they have never been observed. In order to obtain the correct, physically observed value for A_β, we require that the $M_F\, M_{GT}$ term in Eq. (C.9) have an overall positive value. Because we know that the scalar and tensor couplings must be small, and any imaginary contributions to the term must be small, we conclude that

$$M_F\, M_{GT}\, (C_V C'^*_A + C'_V C^*_A) < 0. \tag{C.25}$$

C.2 Holstein Formalism

Holstein [61] [106] generously provides explicit equations to match both Eq. (C.3) (i.e. Holstein's Eq. (51), where neutrino direction is a parameter of the probability distribution) and Eq. (C.15) (Holstein's Eq. (52), where neutrino direction has already been integrated over).

Here's Holstein's Eq. (52):

$$\begin{aligned}
\mathrm{d}^3\Gamma_{\text{Holstein}} &= 2G_v^2\cos^2\theta_c\frac{F_{\mp}(Z',E_\beta)}{(2\pi)^4}\,p_\beta E_\beta(E_0-E_\beta)^2\mathrm{d}E_\beta\,\mathrm{d}^2\hat{\boldsymbol{\Omega}}_\beta \\
&\quad\times\left\{F_0(E_\beta)+\Lambda_1F_1(E_\beta)\hat{\boldsymbol{n}}\cdot\frac{\vec{\boldsymbol{p}}_\beta}{E_\beta}+\Lambda_2F_2(E_\beta)\left[\left(\hat{\boldsymbol{n}}\cdot\frac{\vec{\boldsymbol{p}}_\beta}{E_\beta}\right)^2-\frac{1}{3}\frac{p_\beta^2}{E_\beta^2}\right]\right. \\
&\quad\left.+\Lambda_3F_3(E_\beta)\left[\left(\hat{\boldsymbol{n}}\cdot\frac{\vec{\boldsymbol{p}}_\beta}{E_\beta}\right)^3-\frac{3}{5}\frac{p_\beta^2}{E_\beta^2}\hat{\boldsymbol{n}}\cdot\frac{\vec{\boldsymbol{p}}_\beta}{E_\beta}\right]\right\} \qquad (C.26)
\end{aligned}$$

where E_β, $\vec{\boldsymbol{p}}_\beta$, p_β, E_0, $\mathrm{d}^2\hat{\boldsymbol{\Omega}}_\beta$, and $F_\pm(Z',E_\beta)$ are as in Eq. (C.3), and the Λ_i are given by Holstein's Eq. (48), where, *within this context*, M is the nuclear spin projection along the axis of quantization:

$$\Lambda_1 := \frac{\langle M\rangle}{J} \qquad (C.27)$$

$$\Lambda_2 := 1-\frac{3\langle M^2\rangle}{J(J+1)} \qquad (C.28)$$

$$\Lambda_3 := \frac{\langle M\rangle}{J}-\frac{5\langle M^3\rangle}{J(3J^2+3J-1)}. \qquad (C.29)$$

and we immediately see a relation between several terms in JTW's and Holstein's descrioptions:

$$\text{Holstein's } \hat{\mathbf{n}} = \text{JTW's } \hat{\mathbf{j}} \qquad (C.30)$$

$$\Lambda_1\hat{\boldsymbol{j}} = \frac{\langle M\rangle}{J}\hat{\boldsymbol{j}} = \frac{\vec{\boldsymbol{J}}}{J} \qquad (C.31)$$

$$\Lambda_2 = T_{\text{align}}\frac{(2J-1)}{(J+1)}. \qquad (C.32)$$

Note that Λ_3 is a quadrupole term, and JTW has no equivalent.

The careful reader will eventually note that despite the deceivingly similar notation, Holstein's spectral functions $F_i(E_\beta)$ are not the same as the $F_i(E_\beta,u,v,s)$ in any limit. Among other rules, Holstein's spectral functions obey these:

$$F_i(E_\beta) \neq F_i(E_\beta,u,v,s) \qquad (C.33)$$

$$F_i(E_\beta) = H_i(E_\beta,u,v,0) \qquad (C.34)$$

$$f_i(E_\beta) = F_i(E_\beta,u,v,0). \qquad (C.35)$$

For the $F_i(E_\beta)$ functions of interest to us here, we find the following relationships:

$$\begin{aligned}
F_0(E_\beta) &= H_0(E_\beta, J, J', 0) = F_1(E_\beta, J, J', 0) &&= f_1(E_\beta) \\
F_1(E_\beta) &= H_1(E_\beta, J, J', 0) = F_4(E_\beta, J, J', 0) + \tfrac{1}{3}F_7(E_\beta, J, J', 0) &&= f_4(E_\beta) + \tfrac{1}{3}f_7(E_\beta) \\
F_2(E_\beta) &= H_2(E_\beta, J, J', 0) = F_{10}(E_\beta, J, J', 0) + \tfrac{1}{2}F_{13}(E_\beta, J, J', 0) &&= f_{10}(E_\beta) + \tfrac{1}{3}f_{13}(E_\beta) \\
F_3(E_\beta) &= H_3(E_\beta, J, J', 0) = F_{18}(E_\beta, J, J', 0) &&= f_{18}(E_\beta).
\end{aligned} \tag{C.36}$$

Note that the $f_i(E_\beta)$ in Eq. C.36 are the same spectral functions used to describe a polarized decay spectrum when the neutrino (ie, the recoil) is also observed – though of course such a spectrum must have other terms as well. For the spectrum of interest to us here, in which the neutrino direction has already been integrated over, we can simply look up the $H_i(E_\beta, J, J', 0) = H_i(E, u, v, s\!=\!0)$ spectral functions, and leave it at that. We find:

$$\begin{aligned}
F_0(E_\beta) = {} & |a_1|^2 + 2\,\mathrm{Re}[a_1^* a_2]\,\frac{1}{3M^2}\left[m_e^2 + 4E_\beta E_0 + 2\frac{m_e^2}{E_\beta}E_0 - 4E_\beta^2\right] \\
& + |c_1|^2 + 2\,\mathrm{Re}[c_1^* c_2]\,\frac{1}{9M^2}\left[11m_e^2 + 20E_\beta E_0 - 2\frac{m_e^2}{E_\beta}E_0 - 20E_\beta^2\right] \\
& - 2\frac{E_0}{3M}\,\mathrm{Re}[c_1^*(c_1 + d \pm b)] + \frac{2E_\beta}{3M}\left(3\,|a_1|^2 + \,\mathrm{Re}[c_1^*(5c_1 \pm 2b)]\right) \\
& - \frac{m_e^2}{3ME_\beta}\,\mathrm{Re}\left[-3a_1^* e + c_1^*\left(2c_1 + d \pm 2b - h\frac{E_0 - E_\beta}{2M}\right)\right]
\end{aligned} \tag{C.37}$$

$$F_1(E_\beta) = \delta_{u,v}\left(\frac{u}{u+1}\right)^{1/2}\Bigg\{2\,\mathrm{Re}\Bigg[a_1^*\left(c_1 - \frac{E_0}{3M}(c_1+d\pm b) + \frac{E_\beta}{3M}(7c_1\pm b+d)\right)\Bigg]$$
$$+2\,\mathrm{Re}[a_1^* c_2 + c_1^* a_2]\left(\frac{4E_\beta(E_0-E_\beta)+3m_e^2}{3M^2}\right)\Bigg\}$$
$$\mp\frac{(-1)^s\gamma_{u,v}}{u+1}\,\mathrm{Re}\Bigg\{c_1^*\Bigg(c_1 + 2c_2\left(\frac{8E_\beta(E_0-E_\beta)+3m_e^2}{3M^2}\right) - \frac{2E_0}{3M}(c_1+d\pm b)$$
$$+\frac{E_\beta}{3M}(11c_1 - d\pm 5b)\Bigg)\Bigg\} + \frac{\lambda_{u,v}}{u+1}\,\mathrm{Re}\Bigg\{c_1^*\Bigg[-f\left(\frac{5E_\beta}{M}\right)$$
$$+g\left(\frac{3}{2}\right)^{1/2}\left(\frac{E_0^2-11E_0E_\beta+6m_e^2+4E_\beta^2}{6M^2}\right)\pm 3j_2\left(\frac{8E_\beta^2-5E_0E_\beta-3m_e^2}{6M^2}\right)\Bigg]\Bigg\} \tag{C.38}$$

$$F_2(E_\beta) = \theta_{u,v}\frac{E_\beta}{2M}\,\mathrm{Re}\left[c_1^*\left(c_1 + c_2\frac{8(E_0-E_\beta)}{3M} - d\pm b\right)\right]$$
$$-\delta_{u,v}\frac{E_\beta}{M}\left[\frac{u(u+1)}{(2u-1)(2u+3)}\right]^{1/2}\mathrm{Re}\Bigg\{a_1^*\Bigg(\left(\frac{3}{2}\right)^{1/2} f + g\frac{E_\beta+2E_0}{4M}$$
$$\pm\left(\frac{3}{2}\right)^{1/2} j_2\frac{E_0-E_\beta}{2M}\Bigg)\Bigg\} + (-1)^s\,\kappa_{u,v}\frac{E_\beta}{2M}\,\mathrm{Re}\Bigg[c_1^*\Bigg(\pm 3f \pm \left(\frac{3}{2}\right)^{1/2} g\frac{E_0-E_\beta}{M}$$
$$+3j_2\frac{E_0-2E_\beta}{2M}\Bigg)\Bigg] + \epsilon_{u,v}\,\mathrm{Re}[c_1^* j_3]\left(\frac{21E_\beta^2}{8M^2}\right) \tag{C.39}$$

$$F_3(E_\beta) = -\delta_{u,v}\,(3u^2+3u-1)\left[\frac{u}{(u-1)(u+1)(u+2)(2u-1)(2u+3)}\right]^{1/2}$$
$$\times\,\mathrm{Re}[a_1^* j_3]\left(\frac{E_\beta^2\sqrt{15}}{4M^2}\right) + \frac{\rho_{u,v}}{u+1}\,\mathrm{Re}\left[c_1^*(g\sqrt{3}+j_2\sqrt{2})\left(\frac{5E_\beta^2}{4M^2}\right)\right]$$
$$\pm\frac{(-1)^s\sigma_{u,v}}{u+1}\,\mathrm{Re}[c_1^* j_3]\left(\frac{5E_\beta^2}{2M^2}\right) \tag{C.40}$$

where most of the terms in Eqs. C.37-C.40 have yet to be defined.

The terms $a_1, a_2, b, c_1, c_2, d, e, f, g, h, j_2, j_3$ are described as being structure functions. Holstein gives some predictions for their form, assuming the impulse approximation holds, in his Eq. (67). For the most part, the forms of these structure functions are beyond the scope of this thesis, so I will not re-state them here, however it should be noted that the numerical values used for these parameters were taken from a private communication from Ian Towner to the TRINAT collaboration[107].

An exception is made for parameters a_i and c_i, as these are closely related to the Fermi- and Gamow-Teller couplings for the transition, and must be compared to the equivalent expressions within JTW's formalism. In fact, a_1 and a_2 (c_1 and c_2) are terms within a series expansion for the vector (axial) couplings, including recoil-order corrections (ROC), with recoil energy q and average nuclear mass (of the parent and daughter) M, such that:

$$a(q^2) = a_1 + \left(\frac{q^2}{M^2}\right) a_2 + \cdots \tag{C.41}$$

$$c(q^2) = c_1 + \left(\frac{q^2}{M^2}\right) c_2 + \cdots \tag{C.42}$$

Using the impulse approximation, Holstein finds:

$$a(q^2) \approx \frac{g_V(q^2)}{(1+\frac{\Delta}{2M})}\left[M_F + \frac{1}{6}(q^2-\Delta^2)M_{r^2} + \frac{1}{3}\Delta M_{\mathbf{r}\cdot\mathbf{p}}\right] \tag{C.43}$$

$$\begin{aligned} c(q^2) \approx \frac{g_A(q^2)}{(1+\frac{\Delta}{2M})}\Bigg[&M_{GT} + \frac{1}{6}(q^2-\Delta^2)M_{\sigma r^2} + \frac{1}{6\sqrt{10}}(2\Delta^2+q^2)M_{1y} \\ &+A\frac{\Delta}{2M}M_{\sigma L} + \frac{1}{2}\Delta M_{\sigma r p}\Bigg], \end{aligned} \tag{C.44}$$

where Δ is the difference between the masses of the parent and daughter nuclei, M_F and M_{GT} are the familiar Fermi and Gamow-Teller matrix elements specific to the transition, and $g_V(q^2)$ and $g_A(q^2)$ are the universally applicable vector and axial couplings (which vary according to the energy scale involved). The terms M_{r^2}, $M_{\mathbf{r}\cdot\mathbf{p}}$, $M_{\sigma r^2}$, M_{1y}, $M_{\sigma L}$, and $M_{\sigma rp}$ are matrix elements relating to the nuclear structure of the parent and daughter isotopes. For the sake of simplicity, we note that for the transition of primary concern to us here, ${}^{37}\mathrm{K} \to {}^{37}\mathrm{Ar} + \beta^+ + \nu_e$, we find that $M_{\mathbf{r}\cdot\mathbf{p}} = M_{\sigma L} = M_{\sigma rp} = 0$, so those terms can safely be dropped[107]. Recalling that the energy dependence in $g_V(q^2)$ and $g_A(q^2)$ only becomes relevant at much higher energy scales, we will take the approximation that they are to be treated as constant.

It immediately follows that:

$$a_1 \approx g_V \left(1 - \frac{\Delta}{2M}\right) \left[M_F - \frac{1}{6}\Delta^2 M_{r^2}\right] \tag{C.45}$$

$$a_2 \approx \frac{1}{6} M^2 g_V \left(1 - \frac{\Delta}{2M}\right) M_{r^2} \tag{C.46}$$

$$c_1 \approx g_A \left(1 - \frac{\Delta}{2M}\right) \left[M_{GT} + \frac{1}{6}\Delta^2 \left(\frac{2}{\sqrt{10}} M_{1y} - M_{\sigma r^2}\right)\right] \tag{C.47}$$

$$c_2 \approx \frac{1}{6} M^2 g_A \left(1 - \frac{\Delta}{2M}\right) \left[\frac{1}{\sqrt{10}} M_{1y} + M_{\sigma r^2}\right] \tag{C.48}$$

Next, Holstein goes and tweaks those $F_i(E_\beta)$ terms that we've already written out, by adding in an adjustment for Coulomb corrections. Those corrections have this form:

$$F_i(E_\beta) \to \tilde{F}_i(E_\beta) := F_\mp(Z', E_\beta) \left[F_i(E_\beta) + \Delta F_i(E_\beta)\right] \tag{C.49}$$

To obtain expressions for the $\Delta F_i(E_\beta)$, Holstein invokes some Feynman diagrams and provides expressions for several integrals, all of which are both complex and complicated. The modified spectral functions are provided in terms of functions of these integrals. Since nobody wants to have to evaluate those integrals, Holstein makes a further approximation by taking only the first term in an expansion of the $\Delta F_i(E_\beta)$ in terms of $Z\alpha$, where $Z\alpha \ll 1$. Then, the resulting expressions for $\Delta F_i(E_\beta)$ can be written in terms of much more straightforward integrals over form factors for electric change and weak charge.

If we make the further assumption that these form factors are identical, and that both types of charge are spread over a ball of uniform density with radius R, then we find:

$$X = Y = \frac{9\pi R}{140} \tag{C.50}$$

in the Eqs. (C.51 - C.53) that follow.

Because Holstein doesn't actually write these expressions in terms of $F_i(E_\beta)$, but rather in terms of $F_i(E_\beta, u, v, s)$, this correction presents yet another opportunity for the reader to interpret his notation incorrectly. We note that one must remember to make use of the relations in Eq. (C.36). Furthermore, Holstein notes that some of the terms $F_i(E_\beta, u, v, s)$ are suppressed already, and he does not consider those terms further. We will take this approximation to be adequate for our purposes here.

So, we'll write out the functions for these corrections.

$$\Delta F_1(E_\beta, u, v, s) = \mp \left(\frac{8\alpha Z}{3\pi}\right) X \Big[E_\beta \left(8\,|a|^2 + \tfrac{28}{3}\,|c|^2\right) + E_0 \left(|a|^2 - \tfrac{1}{3}\,|c|^2\right)$$
$$+3\left(\tfrac{m_e c^2}{E_\beta}\right)\left(|a|^2 + |c|^2\right)\Big] \tag{C.51}$$

$$\Delta F_4(E_\beta, u, v, s) = \mp \left(\frac{8\alpha Z}{3\pi}\right) 9 X E_\beta \left[2\,\delta_{u,v}\left(\frac{u}{u+1}\right)^{1/2} \mathrm{Re}[a^* c] \mp (-1)^s \left(\frac{\gamma_{u,v}}{u+1}\right)|c|^2\right] \tag{C.52}$$

$$\Delta F_7(E_\beta, u, v, s) = \mp \left(\frac{8\alpha Z}{3\pi}\right) X\,(E_0 - E_\beta) \left[2\,\delta_{u,v}\left(\frac{u}{u+1}\right)^{1/2} \mathrm{Re}[a^* c]\right.$$
$$\left. \mp(-1)^s \left(\frac{\gamma_{u,v}}{u+1}\right)|c|^2\right] \tag{C.53}$$

We note that the above corrections have been written in terms of $a = a(q^2)$ and $c = c(q^2)$, and we must use Eqs. (C.41, C.42) to put the results in terms of a_1, a_2, c_1, and c_2 so that they can be correctly combined with Eqs. (C.37-C.40).

If we evaluate Holstein's Eqs. (B8) for β^+ decay modes (i.e., the *lower* sign when the option arises), taking $u = v = J = J' = 3/2$ and $s = 0$, we find the following values:

$$\begin{aligned}
&\delta_{u,v} = 1 && \theta_{u,v} = 1 && \rho_{u,v} = \frac{-41}{40} \\
&\gamma_{u,v} = 1 && \kappa_{u,v} = \frac{1}{2\sqrt{2}} && \sigma_{u,v} = \frac{-41}{4\sqrt{35}} \\
&\lambda_{u,v} = \frac{-\sqrt{2}}{5} && \epsilon_{u,v} = \frac{-1}{2\sqrt{5}} && \phi_{u,v} = 0
\end{aligned} \tag{C.54}$$

C.3 Combining Formalisms

To combine the two formalisms, we begin by comparing individual terms within JTW's integrated PDF (Eq. C.15) and Holstein's comparable PDF (Eq. C.26). We find:

$$\xi \approx G_v^2 \cos^2\theta_c \; F_0(E_\beta) \tag{C.55}$$

$$A_\beta \xi \approx G_v^2 \cos^2\theta_c \; F_1(E_\beta), \tag{C.56}$$

where the equality is exact within certain limits as described below.

With these relationships established, we can proceed to compare individual terms within each of the above expressions. Recalling that JTW retains fewer expansion terms than Holstein, and also neglects the smaller nuclear structure functions entirely, it is clear that many terms from Holstein simply have no equivalent within JTW. In fact, of the Holstein structure functions $a_1, a_2, b, c_1, c_2, d, e, f, g, h, j_2,$ and j_3, only a_1 and c_1 are represented within JTW. Holstein has made it clear that a_1 and c_1 are related, respectively, to the Fermi (vector) and Gamow-Teller (axial) couplings. However, JTW uses more parameters to describe each of these: the vector coupling is parameterized by M_F, C_V, and C_V', and the axial coupling by M_{GT}, C_A, and C_A'.

To properly compare the Holstein and JTW formalisms, Eqs. (C.55-C.56) must be evaluated with $C_S = C_S' = C_T = C_T' = 0$, and $a_2 = b = c_2 = d = e = f = g = h = j_2 = j_3 = 0$, and $M = \infty$. We find, from Eq. (C.55):

$$|a_1|^2 \; G_v^2 \cos^2\theta_c = |M_F|^2 \left(|C_V|^2 + |C_V'|^2\right) \tag{C.57}$$

$$|c_1|^2 \; G_v^2 \cos^2\theta_c = |M_{GT}|^2 (|C_A|^2 + |C_A'|^2), \tag{C.58}$$

and treating Eq. (C.56) in a similar manner,

$$|c_1|^2 \; G_v^2 \cos^2\theta_c = 2\,|M_{GT}|^2 \, \mathrm{Re}[C_A C_A'^*] \tag{C.59}$$

$$\mathrm{Re}[a_1^* c_1] \; G_v^2 \cos^2\theta_c = -M_F \, M_{GT} \; \mathrm{Re}[C_V C_A'^* + C_V' C_A^*] \tag{C.60}$$

At this point, given that we are working with complex coupling constants, it becomes clear that there may not be a uniquely defined relationship between the two formalisms' coupling constants. Therefore, we will proceed by simply picking a convention and checking that it is self-consistent and produces the physical behaviour we expect.

Because we expect Holstein to use only the physically observed left-handed couplings, and because we are not presently *searching* for right-handed couplings, we will enforce left-handedness within JTW's description as well. In particular, for left-handed couplings, we have [47]:

$$C_V = C'_V \tag{C.61}$$

$$C_A = C'_A. \tag{C.62}$$

One possible convention for the relationship between the two formalisms which is consistent with the constraints described above is:

$$a_1 = \frac{M_F}{G_v \cos\theta_c} \frac{1}{\sqrt{2}} (C_V + C'_V) \tag{C.63}$$

$$c_1 = \frac{M_{GT}}{G_v \cos\theta_c} \frac{-1}{\sqrt{2}} (C_A + C'_A). \tag{C.64}$$

We note that in the above expressions, the terms $G_v \cos\theta_c$, $(C_V + C'_V)$, and $(C_A + C'_A)$ are universally applicable, while the portion of the couplings dependent on the structure of the nucleus resides entirely within the nuclear matrix elements M_F and M_{GT}.

For convenience, we define the following left-handed couplings for vectors, axial vectors, scalars, and tensors:

$$g_V = \frac{1}{\sqrt{2}} (C_V + C'_V) = +1.0 \tag{C.65}$$

$$g_A = \frac{-1}{\sqrt{2}} (C_A + C'_A) \approx +0.91210 \tag{C.66}$$

$$g_S = \frac{1}{\sqrt{2}} (C_S + C'_S) \tag{C.67}$$

$$g_T = \frac{-1}{\sqrt{2}} (C_T + C'_T), \tag{C.68}$$

where, in addition to the requirements of Eqs. (C.61)-(C.62) we will henceforth consider only the left-handed scalar and tensor couplings, so that

$$C_S = C'_S \tag{C.69}$$

$$C_T = C'_T. \tag{C.70}$$

Furthermore, we will require that all C_X and C'_X are *real*. By enforcing this requirement, we lose the ability to describe a violation of time reversal symmetry, an exotic behaviour that is not the focus of the present search. In order to produce the correct physical behaviour in the decay of ^{37}K, we also require, for the Gamow-Teller matrix elements in Holstein and JTW:

$$M_{GT,\,\text{Holstein}} = \pm M_{GT,\,\text{JTW}} \approx -0.62376 \tag{C.71}$$

The sign ambiguity can be attributed to a sign ambiguity in the original JTW publications. The result is that the literature can't seem to agree on a single sign convention, or even whether the convention ought to be the same in the cases of β^-/β^+ decay. See, for example, Refs [105][108][109]. The important point is that, for whichever convention is in use, the equations result in broadly correct physical behaviour. In the case of ^{37}K, we can use the fact that the overall sign of A_β *must* be negative within our mathematical expressions, because it is experimentally measured to be negative.

We are now in a position to write out Eqs. (C.18), (C.19), and (C.20) in terms of only real, left-handed couplings. Doing so, we note that if the couplings are required to be real, then b_{Fierz} is *only* sensitive to left-handed scalar or tensor couplings, and within A_β, the requirement is only that the scalar and tensor couplings must have *the same* handedness.

The resulting expressions are:

$$\xi = |M_F|^2 \left(|g_S|^2 + |g_V|^2\right) + |M_{GT}|^2 \left(|g_T|^2 + |g_A|^2\right) \tag{C.72}$$

$$b_{\text{Fierz}}\,\xi = -2\gamma \left(|M_F|^2\, g_V\, g_S + |M_{GT}|^2\, g_A\, g_T\right) \tag{C.73}$$

$$A_\beta\,\xi = \frac{2}{5}\,|M_{GT}|^2 \left(g_A^2 - g_T^2\right) + 2\left(\frac{3}{5}\right)^{1/2} M_F\, M_{GT,\,\text{Holstein}} \left(g_V\, g_A - g_S\, g_T\right). \tag{C.74}$$

We will take this opportunity to define and utilize some standard nuclear physics notation:

$$\rho \ := \ \frac{C_A M_{GT}}{C_V M_F} \ = \ \frac{-g_A M_{GT}}{g_V M_F} \tag{C.75}$$

Since each specific transition may, as a result of the nuclear structure relationships involved, take different values for the matrix elements M_F and M_{GT}, a particular transition can often be described by the ratio, ρ, of the Gamow-Teller and Fermi couplings specific to it. This notation offers a cleaner way to characterize standard model predictions of the observables in Eqs. (C.5)-(C.11), but can become somewhat inelegant when used within a description of BSM physics. Taking *only* the leading order (linear) terms in exotic couplings, we find:

$$\xi \ = \ g_V^2 |M_F|^2 \left(1 + \rho^2\right) \tag{C.76}$$

$$b_{\text{Fierz}} \ = \ \frac{-2\gamma}{1+\rho^2} \left(\frac{g_S}{g_V} + \rho^2 \frac{g_T}{g_A} \right) \tag{C.77}$$

$$A_\beta \ = \ \frac{\frac{2}{5}\rho^2 - 2\rho\sqrt{\frac{3}{5}}}{1+\rho^2}, \tag{C.78}$$

where, for ^{37}K, Eq. (C.75) must produce a positive value for ρ in order to be compatible with both Eq. (C.78) and the physically observed results.

Appendix D

Comparing Notation between Holstein and JTW

This section provides several equations and tables intended to be used as a quick reference for comparing differences in notation, sign convention, and normalization between two different descriptions of the beta decay probability distribution.

The following equations provide a term-by-term comparison between the Holstein and JTW conventions, intentionally neglecting ROC terms.

$$\xi = G_v^2 \cos\theta_C \, f_1(E) \tag{D.1}$$

$$a_{\beta\nu} = f_2(E) \,/\, f_1(E) \tag{D.2}$$

$$\frac{\langle \vec{J} \rangle}{J} \cdot \frac{\vec{p}}{E} A_\beta = \Lambda_1 \hat{n} \cdot \frac{\vec{p}}{E} f_4(E) \,/\, f_1(E) \tag{D.3}$$

$$\frac{\langle \vec{J} \rangle}{J} \cdot \frac{\vec{p}_\nu}{E_\nu} B_\nu = \Lambda_1 \hat{n} \cdot \vec{k} \;\; f_6(E) \,/\, f_1(E) \tag{D.4}$$

$$\frac{\langle \vec{J} \rangle}{J} \cdot \frac{(\vec{p} \times \vec{p}_\nu)}{E E_\nu} D_{\mathrm{TR}} = \Lambda_1 \hat{n} \cdot \left(\frac{\vec{p}}{E} \times \hat{k}\right) \;\; f_8(E) \,/\, f_1(E) \tag{D.5}$$

$$\begin{aligned} &\left[\frac{J(J+1) - 3\langle(\vec{J} \cdot \hat{j})^2\rangle}{J(2J-1)}\right]\left[\frac{1}{3}\frac{\vec{p} \cdot \vec{p}_\nu}{E E_\nu} - \frac{(\vec{p} \cdot \hat{j})(\vec{p}_\nu \cdot \hat{j})}{E E_\nu}\right] c_{\mathrm{align}} \\ &= \Lambda_2 \left[(\hat{n} \cdot \frac{\vec{p}}{E})(\hat{n} \cdot \hat{k}) - \frac{1}{3}(\frac{\vec{p}}{E} \cdot \hat{k})\right] \;\; f_{12}(E) \,/\, f_1(E) \end{aligned} \tag{D.6}$$

Holstein	JTW	Thesis	Comments
k			Neutrino momentum 4-vector
	E_ν		Neutrino energy
$\hat{k}$	$\frac{\mathbf{p_\nu}}{E_\nu}$		3D Neutrino emission direction unit vector. Neutrinos are always treated as massless.
p			Beta momentum 4-vector, or sometimes the magnitude of the beta momentum 3-vector. Never the magnitude of the 4-vector.
E	E_e	E_β	Beta energy
$\mathbf{p}$	$\mathbf{p_e}$	$\boldsymbol{\vec{p}_\beta}$	Beta momentum 3-vector
q			Recoil momentum 4-vector, or sometimes a magnitude.

Table D.1: A comparison of some kinematic terms in JTW [1] [2] and Holstein [61][106]. Bolding/italicization carries meaning.

Holstein	JTW	Comments
u	J	Initial state total nuclear angular momentum.
v	J'	Final state total nuclear angular momentum.
s	No equivalent	

Table D.2: A comparison of some angular momenta in JTW [1] [2] and Holstein [61][106].

Holstein	JTW	Thesis	Comments
$G_v^2 \cos\theta_C\, f_1(E)$	ξ	$\xi(E_\beta)$	Normalization. Proportional to the fractional decay rate.
$\hat{n}$	$\mathbf{j}$	$\hat{\boldsymbol{j}}$	Nuclear polarization unit vector. Also the axis of quantization.
J	J		Total nuclear angular momentum quantum number
$\langle M\rangle$	$\lvert\langle \mathbf{J}\rangle\rvert$		Angular momentum projection along the axis of quantization
$\Lambda^{(1)}\hat{n} = \frac{\langle M\rangle}{J}\hat{n}$	$\frac{\langle \mathbf{J}\rangle}{J}$	$\Lambda_1 \hat{\boldsymbol{n}}$	Dipole element vector. Proportional to nuclear polarization.
$\Lambda^{(2)}$	$\frac{J(J+1)-3\langle(\vec{\boldsymbol{J}}\cdot\hat{\boldsymbol{j}})^2\rangle}{J(2J-1)}\frac{(2J-1)}{(J+1)}$	$T_{\text{align}}(\vec{\boldsymbol{J}})\frac{(2J-1)}{(J+1)}$	Quadrupole element
$\Lambda^{(3)}$	No equivalent	Λ_3	Octopole element
$\Lambda^{(4)}$	No equivalent	Λ_4	Hexadecapole element

Table D.3: A comparison of terms relating to multipole elements and their normalizations in JTW [1] [2] and Holstein [61] [106].

Term		Integral
$f_1(E_\beta)$	$\leftrightarrow$	$\int 1 \,\mathrm{d}\hat{\boldsymbol{\Omega}}_{\boldsymbol{k}} = 4\pi$
$f_2(E_\beta)$	$\leftrightarrow$	$\int \left(\frac{\vec{\boldsymbol{p}}_\beta \cdot \hat{\boldsymbol{k}}}{E_\beta}\right) \mathrm{d}\hat{\boldsymbol{\Omega}}_{\boldsymbol{k}} = 0$
$f_3(E_\beta)$	$\leftrightarrow$	$\int \left(\left(\frac{\vec{\boldsymbol{p}}_\beta \cdot \hat{\boldsymbol{k}}}{E_\beta}\right)^2 - \frac{1}{3}\frac{p_\beta^2}{E_\beta^2}\right) \mathrm{d}\hat{\boldsymbol{\Omega}}_{\boldsymbol{k}} = 0$
$f_4(E_\beta)$	$\leftrightarrow$	$\int \left(\hat{\boldsymbol{n}} \cdot \frac{\vec{\boldsymbol{p}}_\beta}{E_\beta}\right) \mathrm{d}\hat{\boldsymbol{\Omega}}_{\boldsymbol{k}} = 4\pi \left(\hat{\boldsymbol{n}} \cdot \frac{\vec{\boldsymbol{p}}_\beta}{E_\beta}\right)$
$f_5(E_\beta)$	$\leftrightarrow$	$\int \left(\hat{\boldsymbol{n}} \cdot \frac{\vec{\boldsymbol{p}}_\beta}{E_\beta}\right)\left(\frac{\vec{\boldsymbol{p}}_\beta \cdot \hat{\boldsymbol{k}}}{E_\beta}\right) \mathrm{d}\hat{\boldsymbol{\Omega}}_{\boldsymbol{k}} = 0$
$f_6(E_\beta)$	$\leftrightarrow$	$\int \left(\hat{\boldsymbol{n}} \cdot \hat{\boldsymbol{k}}\right) \mathrm{d}\hat{\boldsymbol{\Omega}}_{\boldsymbol{k}} = 0$
$f_7(E_\beta)$	$\leftrightarrow$	$\int \left(\hat{\boldsymbol{n}} \cdot \hat{\boldsymbol{k}}\right)\left(\frac{\vec{\boldsymbol{p}}_\beta \cdot \hat{\boldsymbol{k}}}{E_\beta}\right) \mathrm{d}\hat{\boldsymbol{\Omega}}_{\boldsymbol{k}} = \frac{1}{3}4\pi \left(\hat{\boldsymbol{n}} \cdot \frac{\vec{\boldsymbol{p}}_\beta}{E_\beta}\right)$
$f_8(E_\beta)$	$\leftrightarrow$	$\int \hat{\boldsymbol{n}} \cdot \left(\frac{\vec{\boldsymbol{p}}_\beta \times \hat{\boldsymbol{k}}}{E_\beta}\right) \mathrm{d}\hat{\boldsymbol{\Omega}}_{\boldsymbol{k}} = 0$
$f_9(E_\beta)$	$\leftrightarrow$	$\int \hat{\boldsymbol{n}} \cdot \left(\frac{\vec{\boldsymbol{p}}_\beta \times \hat{\boldsymbol{k}}}{E_\beta}\right)\left(\frac{\vec{\boldsymbol{p}}_\beta \cdot \hat{\boldsymbol{k}}}{E_\beta}\right) \mathrm{d}\hat{\boldsymbol{\Omega}}_{\boldsymbol{k}} = 0$
$f_{10}(E_\beta)$	$\leftrightarrow$	$\int T_2(\hat{\boldsymbol{n}}) : \left[\frac{\vec{\boldsymbol{p}}_\beta}{E}, \frac{\vec{\boldsymbol{p}}_\beta}{E}\right] \mathrm{d}\hat{\boldsymbol{\Omega}}_{\boldsymbol{k}} = 4\pi\, T_2(\hat{\boldsymbol{n}}) : \left[\frac{\vec{\boldsymbol{p}}_\beta}{E}, \frac{\vec{\boldsymbol{p}}_\beta}{E}\right]$
$f_{11}(E_\beta)$	$\leftrightarrow$	$\int T_2(\hat{\boldsymbol{n}}) : \left[\frac{\vec{\boldsymbol{p}}_\beta}{E}, \frac{\vec{\boldsymbol{p}}_\beta}{E}\right]\left(\frac{\vec{\boldsymbol{p}}_\beta \cdot \hat{\boldsymbol{k}}}{E}\right) \mathrm{d}\hat{\boldsymbol{\Omega}}_{\boldsymbol{k}} = 0$
$f_{12}(E_\beta)$	$\leftrightarrow$	$\int T_2(\hat{\boldsymbol{n}}) : \left[\frac{\vec{\boldsymbol{p}}_\beta}{E}, \hat{\boldsymbol{k}}\right] \mathrm{d}\hat{\boldsymbol{\Omega}}_{\boldsymbol{k}} = 0$
$f_{13}(E_\beta)$	$\leftrightarrow$	$\int T_2(\hat{\boldsymbol{n}}) : \left[\frac{\vec{\boldsymbol{p}}_\beta}{E}, \hat{\boldsymbol{k}}\right]\left(\frac{\vec{\boldsymbol{p}}_\beta \cdot \hat{\boldsymbol{k}}}{E}\right) \mathrm{d}\hat{\boldsymbol{\Omega}}_{\boldsymbol{k}} = \frac{1}{3}4\pi\, T_2(\hat{\boldsymbol{n}}) : \left[\frac{\vec{\boldsymbol{p}}_\beta}{E}, \frac{\vec{\boldsymbol{p}}_\beta}{E}\right]$
$f_{14}(E_\beta)$	$\leftrightarrow$	$\int T_2(\hat{\boldsymbol{n}}) : \left[\hat{\boldsymbol{k}}, \hat{\boldsymbol{k}}\right] \mathrm{d}\hat{\boldsymbol{\Omega}}_{\boldsymbol{k}} = 0$
$f_{15}(E_\beta)$	$\leftrightarrow$	$\int T_2(\hat{\boldsymbol{n}}) : \left[\hat{\boldsymbol{k}}, \hat{\boldsymbol{k}}\right]\left(\frac{\vec{\boldsymbol{p}}_\beta \cdot \hat{\boldsymbol{k}}}{E}\right) \mathrm{d}\hat{\boldsymbol{\Omega}}_{\boldsymbol{k}} = 0$
$f_{16}(E_\beta)$	$\leftrightarrow$	$\int T_2(\hat{\boldsymbol{n}}) : \left[\frac{\vec{\boldsymbol{p}}_\beta}{E}, \frac{\vec{\boldsymbol{p}}_\beta}{E} \times \hat{\boldsymbol{k}}\right] \mathrm{d}\hat{\boldsymbol{\Omega}}_{\boldsymbol{k}} = 0$
$f_{17}(E_\beta)$	$\leftrightarrow$	$\int T_2(\hat{\boldsymbol{n}}) : \left[\hat{\boldsymbol{k}}, \frac{\vec{\boldsymbol{p}}_\beta}{E} \times \hat{\boldsymbol{k}}\right] \mathrm{d}\hat{\boldsymbol{\Omega}}_{\boldsymbol{k}} = 0$
$f_{18}(E_\beta)$	$\leftrightarrow$	$\int T_3(\hat{\boldsymbol{n}}) : \left[\frac{\vec{\boldsymbol{p}}_\beta}{E}, \frac{\vec{\boldsymbol{p}}_\beta}{E}, \frac{\vec{\boldsymbol{p}}_\beta}{E}\right] \mathrm{d}\hat{\boldsymbol{\Omega}}_{\boldsymbol{k}} = 4\pi\, T_3(\hat{\boldsymbol{n}}) : \left[\frac{\vec{\boldsymbol{p}}_\beta}{E}, \frac{\vec{\boldsymbol{p}}_\beta}{E}, \frac{\vec{\boldsymbol{p}}_\beta}{E}\right]$

Table D.4: Integrals of terms from Holstein's Eq. (51) [61] [106].